Traction Between Rough Surfaces

by

Junki Joe

A dissertation submitted in partial fulfillment
of the requirements for the degree of
Doctor of Philosophy
(Mechanical Engineering)
in The University of Michigan
2021

Doctoral Committee:

Professor James Barber, Co-Chair
Professor Michael Thouless, Co-Chair
Professor Joseph Conlon
Professor Wei Lu
Professor Mark Rudelson

Junki Joe

jkjoe@umich.edu

ORCID iD: 0000-0002-8949-1592

To my family and my beloved wife, Yong Jae Kim

ACKNOWLEDGEMENTS

I would like to thank my advisors, Prof. Barber and Prof. Thouless, for invaluable advice, continuous support, and patience during my Ph.D. study. I would especially like to express my gratitude to Prof. Barber for giving me a precious gift, a beautiful tribology problem. Insightful discussions with them shaped my mindset in researching and teaching. Their valuable guidance will play a role as clues and solutions whenever I encounter obstacles in the future. I will make an effort to keep it in mind forever. One day, I was discouraged by not having a result I expected, but he told me there is no bad news in research and always good news, which became my resource to challenge any problems. He also showed me a big picture of my work whenever I was obsessed with minor detail or the wrong direction. I feel I was a very lucky student because they supported and gave advice about any researches I was interested in with no objection. I also appreciate that he gave me fulfilling experiences to teach ME311 students, and I could learn many things about teaching. Overall, I felt grateful and honored to have discussed with them, and they will remain my best role model as a researcher, mentor, and teacher.

I would like to thank the members of my Ph.D. committee, Prof. Lu, Prof. Conlon, and Prof. Rudelson, for their suggestions and critique. I appreciate Prof. Conlon's and Prof. Rudelson's patience and time to understand my explanation, although we are from different departments. It was always joyful to discuss with Prof. Conlon in his office, and the discussion made me more confident in my work.

I would like to thank Prof. Ciavarella in the Polytechnic University of Bari for

continuous discussion and sharing his endless research ideas during my whole Ph.D. study. Although we have not met in person, I could feel he is the most enthusiastic researcher. He introduced me to new topics, which help me broaden my interest. Also, I would like to thank his past Ph.D. student, Dr. Papangelo, for collaboration.

I would like to thank Prof. Scaraggi at the University of Salento, who collaborated on my first paper, for allowing me to use his numerical method code. I appreciate that he explained his code, kept updating his program versions and allowed me to review other researchers' papers.

I also thank Prof. Müser and Dr. Anle Wang in the Saarland University for conducting numerical simulation for me in my last Ph.D. year. I contacted them because I worried about my entire work having good agreements with other numerical simulations by luck or not. Since Dr. Anle Wang helped me validating my work as like my work is his, I could be more confident in my work.

I have to thank Prof. Jongbaeg Kim, Prof. Woochul Kim, and Prof. Won Suk Ohm in Yonsei Univerisity for providing helpful advice before starting the road to Ph.D. Thanks to the advice, I could study at the University of Michigan and work with the awesome scholars above.

I thank all of my friends in Ann Arbor who started the road to Ph.D. with me: Hun Kim(my roommate for a long time, Tennis and working out partner, very friendly), Sunghyun Park(hanging with him was always fun, another tennis and working out partner), Sang Tek Oh(Sociology guy, Tennis teacher, very intelligent). I could more enjoy my Ph.D. life in Ann Arbor with these friends.

I have to thank one of my best friends, Don Lee, in South Korea. While I study in the United States, he spent much time for my parents in Korea on behalf of me. Thanks to his help, I could focus more on my research.

I thank my parents, who have sacrificed their life for me. I love them very much. They always provided unconditional love and care to me. I have no doubt that I

could not come this far without their support.

TABLE OF CONTENTS

LIST OF FIGURES

Figure

ABSTRACT

We develop a theoretical model to predict the effect of surface roughness on load-displacement relation (traction) and probability density function [PDF] for local gaps. We characterize the rough surface by the PDF for a rough surface whose power spectral density is truncated at some upper cutoff wavenumber. The PDF is then modified by the inclusion of an additional incremental wavenumber, and hence the upper cutoff wavenumber increases. If the incremental roughness is sufficiently small, the modification of the PDF can be determined by a linearized solution for the combined effect of elastic deformation and adhesive laws (e.g., Lennard-Jones law). The effect of the entire spectrum is obtained by iteration of the above process. We find that the PDF converges at large wavenumbers, in contrast to non-adhesive contact theories.

Because the adhesion between surfaces must decay with increasing separation, the adhesive laws have a charter of a negative spring, which can trigger elastic instability. With an energetic analysis and numerical simulation, we show that an arbitrarily small perturbation of the coarse-scale roughness (i.e., low wavenumbers) is sufficient to trigger the instability. The instability results in a non-uniform pattern of alternating regions of contact and separation, and the characteristic length scale of the pattern correlates with the most unstable wavelength. It leads to different behavior during approach and separation and consequent hysteresis losses.

Some roughness outside the instability range can be expected to influence the contact morphology and hence the adhesive law. In this context, we apply the technique

from the iterative process sequentially. Suppose that the PSD is arbitrarily separated into coarse-scale and fine-scale components, and fine-scale roughness is sufficiently small. This allows us to use the iterative method to determine the traction for a plane surface containing only the fine-scale roughness. We can then consider the coarse-scale modeled explicitly as the roughness, but the effect of the fine-scale is reflected in a modified traction law. Because the modified traction laws have a less character of the negative spring, this process allows us to proceed to lower wavenumber without encountering the instability due to the inclusion of the incremental roughness.

Although the modified traction laws have weaker negative springs, they still can trigger the instability. With the modified traction laws, we examine the effect of fine-scale roughness on both the generation of patterns and the load-displacement relations. The numerical simulation results show that this approach is a very good approximation. In particular, the maximum negative slope of the modified traction laws correlates extremely well with an instability criterion obtained by the energetic argument.

The present theoretical model involving the iterative process has an analogy with diffusion problems and hence random-walk problems. We convert the iterative process into diffusional partial differential equations, allowing us to extend the theory into non-adhesive law, which can be approximated by a power law. We show that as the exponent and coefficient of the power-law type of the regularized non-adhesive law increase, the traction converges a unique solution. In order to validate the theory, the results are then compared with numerical simulations such as molecular dynamics and Green's function molecular dynamics and show extremely good agreement.

CHAPTER I

Introduction

1.1 Interfacial Interaction Law

Adhesive interactions between contacting solids have a major impact in many areas of engineering and everyday life. For example, the degree of adhesion is critical for the assessment of the quality of glued joints, in designing human joint prostheses, or in understanding the sense of touch. Adhesive forces are also central to most modern theories of frictional interaction, as well as to Archard's theory of adhesive wear. Coatings have been applied widely in aerospace, biomedical, electronic, and many other industries with a view to obtaining desired frictional/adhesive characteristics.

In recent years, the need to include adhesion in contact analysis has become increasingly pressing as micro- and nano-electromechanical systems have been developed. In everyday life objects at the "human scale" do not stick to each other, principally as a result of inevitable surface roughness which reduces the proportion of the surface in intimate contact. However, this does not always hold true at smaller scales, where surface forces, including adhesion, becomes greater in proportion to

Chapter 1 is adapted from part of the published paper:
Ciavarella, M., Joe, J., Papangelo, A., Barber, J. R. "The role of adhesion in contact mechanics." *Journal of the Royal Society Interface* 16.151 (2019): 20180738.

volume forces.

Designing surfaces for optimal adhesive performance is now a hot topic in the engineering community, where nature is an important source of inspiration. Indeed we are still far from being able to achieve the astonishing capability of insects and reptiles to control interface adhesive strength. The most famous case is perhaps that of the gecko, whose feet can sustain several times its weight, whilst also being able to completely detach its foot in 15 ms. This remarkable achievement is attributed to the hierarchical structures of gecko feet which are split into many fibrils in order to reach the optimal nanoscale size for the attachment to be robust and close to the theoretical strength. This has stimulated the growth of the field of bio-inspired engineering, which attempts to replicate natural solutions with patterns in polymer films having micron- or sub-micron-sized protrusions.

1.1.1 Lennard-Jones law

Classical contact mechanics is typically characterized by the *Signorini inequalities*, which demand that the tractions between interacting solid bodies be non-tensile, and that interpenetration of material is inadmissible. We can then partition the surface of a body into regions of *contact*, where the gap between the bodies is zero and the normal component of traction is compressive, and *separation*, where there are no tractions and the gap is positive. However, at very small length scales, this dichotomy is an oversimplification. The local tractions between the bodies will be a continuous function of relative approach and van der Waals forces and other physical mechanisms can cause regions of tensile [or *adhesive*] tractions. Most authors assume that the Lennard-Jones 6–12 law [4] defines the relation between the force and separation of two individual molecules, and if a continuum is approximated as a uniform distribution of molecules, the resulting traction σ [tensile positive] between two half

spaces is then found to be [5, 6]

$$\sigma(g) = \frac{8\Delta\gamma}{3\varepsilon}\left[\frac{\varepsilon^3}{g^3} - \frac{\varepsilon^9}{g^9}\right] \quad \text{where} \quad \Delta\gamma = \int_{\varepsilon}^{\infty} \sigma(g)dg \tag{1.1}$$

is the *interface energy* or the work done per unit area of interface in separating the two bodies from the equilibrium position $g = \varepsilon$, at which $\sigma = 0$. This expression is shown in Figure 1.1. The maximum tensile traction occurs at a separation $g = 3^{1/6}\varepsilon$ and is $\sigma_0 = 16\Delta\gamma/9\sqrt{3}\varepsilon$.

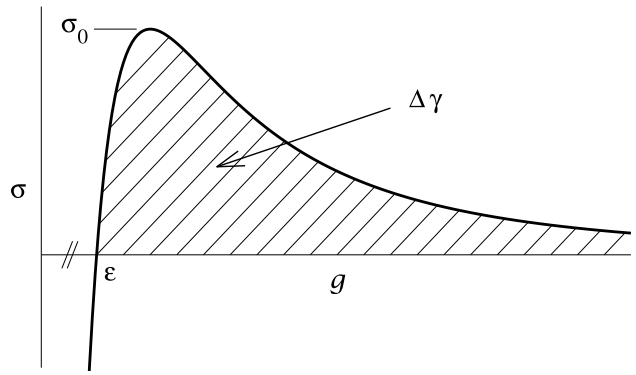

Figure 1.1: The traction law defined in equation 1.1. The interface energy $\Delta\gamma$ corresponds to the shaded area.

1.2 Contact of a sphere on a plane

Equation 1.1 can be integrated to determine the force transmitted between two rigid bodies of known shape and relative position. In particular, if a sphere of radius R is placed near a half plane, the maximum tensile force [the *pull-off force*] occurs when the point of closest approach is equal to ε and is of magnitude $2\pi R\Delta\gamma$. Bradley [7] obtained this result by integrating the intermolecular force law over two finite spheres of radius R_1, R_2 and then dropping terms of the order ε/R_i, $i = 1, 2$. This approach was extended by Rumpf [8] and Rabinovich *et al.* [9] to estimate the adhesive force between a small spherical particle and a rough surface, characterized as a set of

spherical asperities. These equations showed that even small amplitude of roughness decreases pull-off by large factors.

1.2.1 The JKR theory

If the contacting bodies are deformable, equation 1.1 can be combined with an analysis of the deformation, but the resulting boundary-value problem is highly non-linear and generally can only be solved by numerical methods. An approximation introduced by Johnson *et al.* [10] retains the Signorini dichotomy between regions of contact and separation, but relaxes the requirement that contact tractions be non-tensile. The total potential energy $\Pi = U + \Omega - \Gamma$ is then computed as the sum of elastic strain energy U, potential energy of external forces Ω and interface energy $\Gamma = A_{\rm c}\Delta\gamma$, where $A_{\rm c}$ is the total contact area. The partition into areas of contact and separation is then determined so as to minimize Π. This is now generally known as the *JKR solution*. Conceptually, it is identical to Griffith's theory of fracture and hence is equivalent to linear elastic fracture mechanics [LEFM], with $\Delta\gamma$ playing the rôle of the critical energy release rate G_c. It follows that an alternative formulation is to demand that the contact traction be square-root singular at all edges of the contact area, with stress intensity factor

$$K_{\rm I} = \sqrt{2E^*\Delta\gamma} \quad \text{where} \quad \frac{1}{E^*} = \frac{1-\nu_1^2}{E_1} + \frac{1-\nu_2^2}{E_2} \tag{1.2}$$

and E_i, ν_i are Young's modulus and Poisson's ratio respectively for the two bodies, with $i = 1, 2$. For the sphere, the [compressive] indentation force P, the contact radius a and the indentation depth Δ are related by the equations

$$\hat{P} = \frac{4\hat{a}^3}{3\pi} - \frac{4\hat{a}^{3/2}}{\sqrt{2\pi}}\,; \quad \hat{\Delta} = \hat{a}^2 - \sqrt{2\pi\hat{a}}\,, \tag{1.3}$$

where the dimensionless parameters

$$\hat{P} = \frac{P}{\pi R \Delta\gamma} \; ; \quad \hat{a} = \left(\frac{E^* R}{\Delta\gamma} \right)^{1/3} \frac{a}{R} \; ; \quad \hat{\Delta} = \left(\frac{E^* R}{\Delta\gamma} \right)^{2/3} \frac{\Delta}{R} \; . \tag{1.4}$$

The resulting relation between $\hat{P}$ and $\hat{\Delta}$ is shown in Fig. 1.2.

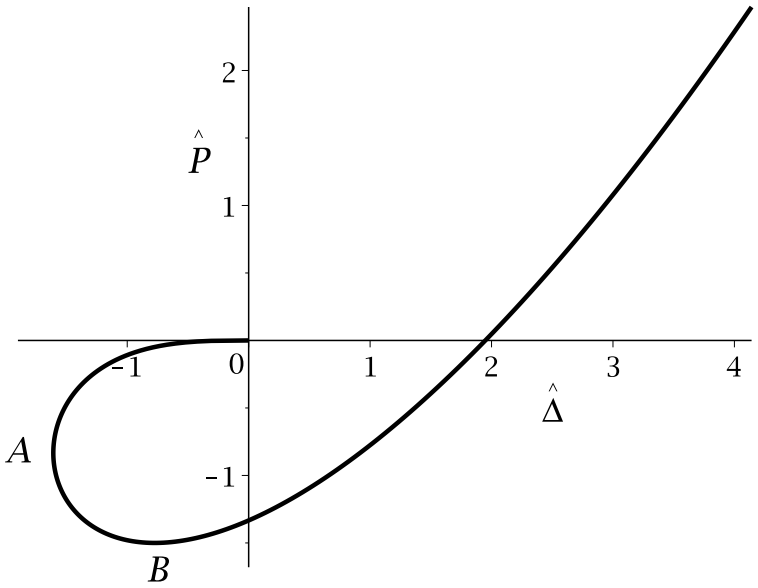

Figure 1.2: JKR solution for the relation between dimensionless compressive force $\hat{P}$ and indentation $\hat{\Delta}$ for the contact of a sphere and a plane.

In this figure, the pull-off force under force control is defined by point B and corresponds to $P = -3\pi R\Delta\gamma/2$, which differs from Bradley's rigid-body value only by a factor 3/4. Under force control, only points to the right of B are stable, whereas under displacement control, stability is retained to the maximum negative indentation at A. In either case, once the limiting point is reached, the sphere will jump out of contact and some energy will be dissipated, presumably in the form of elastodynamic waves. Similarly, if the sphere is slowly brought to approach the half space, it will jump into contact from the origin to point B, again with a loss of energy. A sequence of contact and separation cycles therefore implies a hysteretic loss of energy.

The original JKR solution considered only the contact of a sphere on a plane,

but the same technique can be applied to any geometry for which the corresponding boundary-value problem can be solved. For example, Johnson [11] gave the solution for a body with a sinusoidal surface in partial contact with a plane. Also, the energetic argument can be used to obtain numerical solutions using a boundary-element approach. For example, Popov *et al.* [12] used this approach to determine the pull-off force displacement relation for flat rigid punches of various planforms. They showed that under displacement control, final detachment occurs from a contact area approximately identified with a circle inscribed in the planform, but that the maximum tensile force occurs before this state is reached.

1.2.2 The Tabor parameter

A numerical solution [13] of the problem for a sphere using the traction law of equation 1.1 shows that the pull-off force P_0 is a continuous function of the *Tabor parameter*

$$\mu = \sqrt[3]{\frac{R(\Delta\gamma)^2}{E^{*\,2}\varepsilon^3}}\,, \tag{1.5}$$

[14], tending to the Bradley rigid-body value of $2\pi R\Delta\gamma$ at $\mu = 0$ and to the JKR value of $(3/2)\pi R\Delta\gamma$ as $\mu \to \infty$. Equation 1.5 contains the radius R and hence is specific to the spherical contact problem.

1.2.3 Solutions for lower values of μ

The JKR solution approaches the exact solution asymptotically as $\mu \to \infty$, and it is natural to seek a corresponding solution for the case $\mu \to 0$. For small values of μ, many authors use a strategy which can be summarized as

1. Solve the problem neglecting adhesive tractions — i.e. using the Signorini boundary conditions.

2. Find the gap between the surfaces in the separation region in step 1.

3. Calculate a 'correction' to the contact force based on the adhesive tractions that would be predicted in such a gap.

4. Neglect any further elastic deformation that might be expected from these adhesive tractions.

This approach has come to be known as the *DMT method*, since it was first introduced by Derjaguin *et al.* [15], who however used only the van der Waals term from equation 1.1 in step 3. If the bodies are strictly rigid so $\mu = 0$, no elastic deformation occurs in step 1 and the DMT solution so defined is exact. However, it cannot be regarded as an asymptotic solution for small but finite μ, though many authors refer to this as the 'DMT régime'. Indeed, Pashley [16] showed that the DMT method can give unrealistic predictions, notably that the pull-off force is always overestimated for any μ (the error increases with μ), and occurs at separations larger than zero, which contradicts the results of rigorous numerical solutions. Greenwood [17] gives a detailed criticism of the DMT method and offers an alternative 'semi-rigid' approach based on determining the elastic displacements due to the tractions predicted by the rigid theory. Derjaguin *et al.* [15] did not obtain a load-displacement relation analogous to the 'JKR equation' (1.3), but Maugis [1] developed an approximate relation by adding a constant 'adhesive force' $2\pi R\Delta\gamma$ to the Hertzian load, obtaining

$$\hat{P} = \frac{4\hat{\Delta}^{3/2}}{3\pi} - 2 \; . \tag{1.6}$$

Following Greenwood [18], we shall refer to this as the 'DMT-M solution'.

Figure 1.3 shows a schematic of the DMT solution, where repulsive pressures only act in the area of contact, and adhesive forces only add to the Hertz problem outside the contact area. In the JKR solution, instead, both compressive and tensile stresses act in the area of contact, and nothing else occurs outside. Obviously there are two very different necks: the Hertz neck of DMT, and the LEFM neck of JKR.

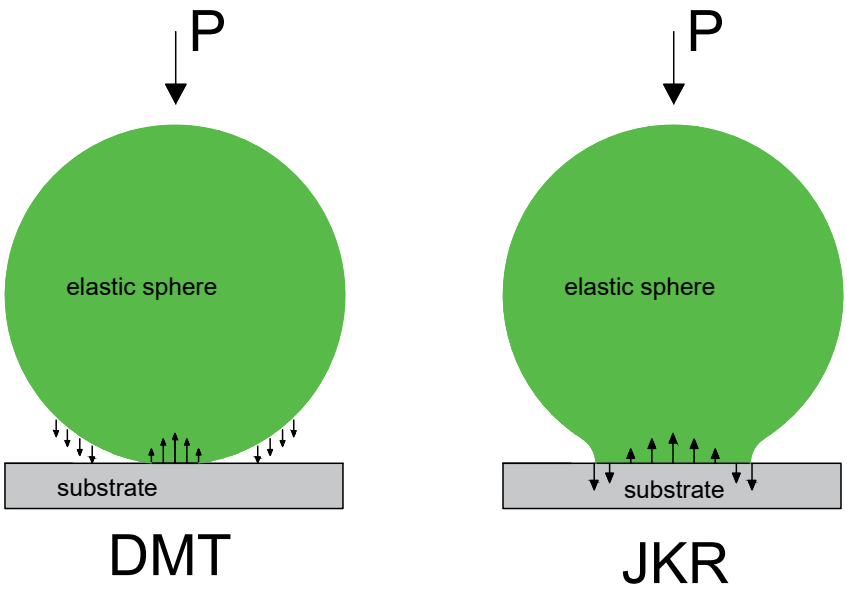

Figure 1.3: Sketch of traction distributions in DMT and JKR type of solution. In DMT the contact area coincides with that obtained from the non-adhesive problem, the adhesive tractions are thus confined in the separated zone. In a JKR solution both compressive and adhesive tractions are exchanged within the contact area.

1.2.4 Approximation of the traction law

An alternative strategy appropriate for intermediate values of μ is to approximate the traction law (Equation 1.1) to make the resulting boundary-value problem more tractable. Maugis [1] used a law in which the tensile tractions in the separation region are assumed to be constant and equal to the maximum value σ_0 from Equation 1.1 over a range $0 < g < g_{\max}$, beyond which they are zero. The value of $g_{\max}$ is chosen such that the interface energy $\Delta\gamma = \sigma_0 g_{\max}$. This reduces the contact problem to a linear three-part boundary-value problem which can be solved in closed form for the case of the sphere. Alternatively, Greenwood and Johnson [19] showed that the superposition of two axisymmetric Hertzian traction distributions, one tensile and one [over a smaller circle] compressive, could be chosen so as to satisfy the contact condition in the smaller circle. The traction in the surrounding annulus is then a single-valued function of gap and parameters can be chosen so as to ensure that the

maximum tensile traction is σ_0 and the implied interface energy is $\Delta\gamma$. Both these approaches predict a dependence of pull-off force on μ that is qualitatively similar, but not identical to the numerical solution [13].

1.2.5 An adhesion map

The map of the contact of elastic spheres is given in Fig. 1.4 as given by Johnson & Greenwood [20], as the theory which dominates a certain range of (i) load and (ii) Tabor (or Maugis) parameter. For large compressive loads, it is seen that little is gained by using adhesive theories, as Hertz theory is a good approximation. For tensile loads (not shown in the figure), there is no alternative to adhesive theories, and intermediate cases depend on the Bradley [7] to JKR [10] transition. Recently [21] have shown that $\mu > 5$ is not sufficient if one wants to model accurately the jump-in phenomenon and hence the hysteresis associated to the instabilities in getting in and out of contact. Strictly speaking, JKR is a solution valid only for very large Tabor parameters, and DMT is never an accurate solution. Maugis-Dugdale is a convenient solution for representing a transition between the DMT-Maugis and the JKR regime, and Schwartz [22] has given an alternative solution which divides the surface energy into a JKR contribution and a DMT-M one.

1.3 Concepts of Rough Surfaces

All surfaces have roughness; The roughness affects physical properties of contact processes such as friction coefficient, leakage on sealing, adhesion, electrical and thermal conductivity. Because roughness has randomness, it is challenging to analyze the physical effect of the roughness. Thanks to nature, however, the randomness of the actual rough surface is multiscaled as self-affine fractals in fine scale, resulting in Gaussian probability distribution for gaps. Some theoretical models idealizing self-affinity and Gaussianity will be discussed in the following sections.

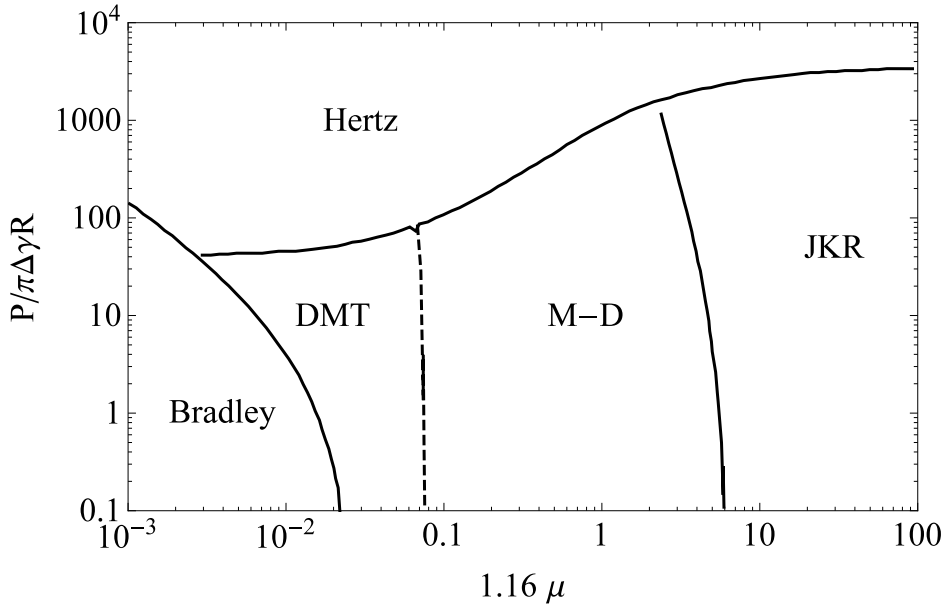

Figure 1.4: Adhesion map for a sphere. Depending on the dimensionless load and the Tabor parameter, the most appropriate model is indicated. M-D refers to Maugis-Dugdale model, see [1]

1.3.1 Asperity models

Bowden and Tabor [23] developed a friction model between rough surfaces, introducing an idea that rough surfaces make contact only on asperities' tips. Because only the tip of asperities is contacted, plastic deformation occurs between the surfaces even with a small load. This assumption makes the load proportional to the contact area because the stress at the asperity junction is approximated by the hardness, which is usually approximately three times the yield stress [24]. Likewise, the friction force is required to break the asperity junctions, which are treated as cold-welded. This idea suggests that the friction force is proportional to contact area and load, which agrees with Amonton's second law. Figure 1.5 illustrates the idealization of a rough surface as a collection of asperities. In Greenwood and Williamson (1966) [GW] theory, the rough surfaces are idealized as normally or exponentially distributed asperities having the same curvature and independent to other asperities between a rigid flat and rough elastic surface. Then, each asperity is independently applied by

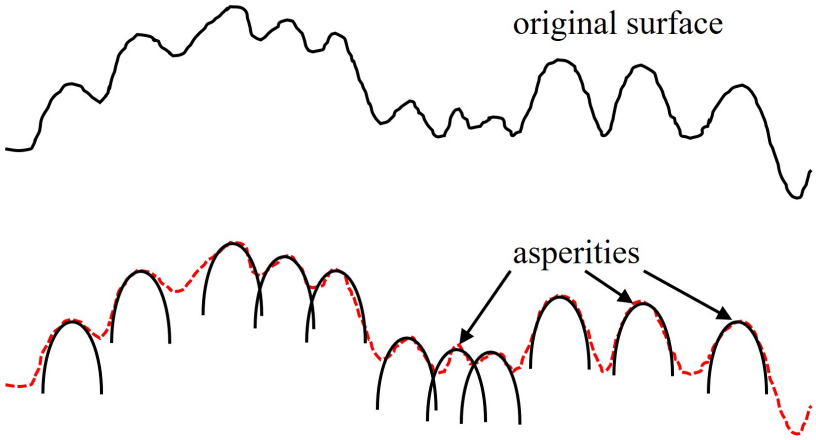

Figure 1.5: Original rough surface and the idealized surface as a collection of asperities.

Hertzian elastic contact theory to calculate contact area and load. Regardless of the form of the deformation, the theory results in a simple linear relation between load and contact area. However, the GW model has problems explaining the multiscality of rough surfaces. As its scale decreases, the independence of asperities is no longer valid because an asperity affects adjacent asperities. Despite this weakness, many researchers have developed the asperity model because of its simplicity.

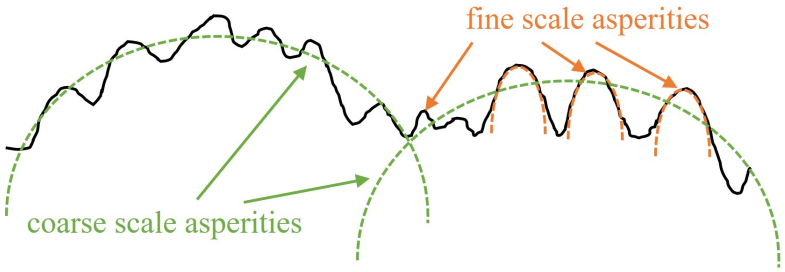

Figure 1.6: Multiscaled surface with two different sizes of curvature.

1.3.2 Multiscale models

The measurable magnification increased by the development of experimental equipment, and it was revealed that the rough surface is multiscaled as self-affine fractals in fine-scale [25]. This property was suggested by Archard (1957), who pioneered the

idea that smaller asperities idealize the rough surfaces on larger asperities on even larger asperities, as seen in Figure 1.6, explaining the multiscality of the roughness. This model provides qualitatively better descriptions than GW model, and started to be acknowledged in the 1980s, since the multiscale property of rough surfaces was revealed by the development of experimental equipment. To describe the multiscality, Ciavarella *et al.* (2000) [CDBJ] used a Weierstrass-shaped profile to find probability density function for pressure for adhesiveless contacts. Westergaard's solution is iteratively used on each sinusoidal of the Weierstrass function. A similar method is adapted by Persson (2001), extending the Weierstrass function into surface power spectral density [PSD].

Compared to the conditional PDF from sinusoidal, the PDF from part of PSD with uniform phase shows no singularity. Another advantage of using PSD over the Weierstrass profile is that it is a more realistic idealization of the rough surface. Persson's theory results in a simple diffusion type of partial differential equation assuming that fine-scale roughness is under full contact, while CDBJ introduced an iterative method to find PDF for pressure. In Section 2 and 3, we extend the iterative methods inspired by CDBJ and Persson into adhesive contact, and in Section 5, we derive a modified diffusional partial differential equation based on Section 3.

1.3.3 Fuller and Tabor

The first theoretical investigation of the effect of roughness on adhesion was that of Fuller and Tabor [26], who followed Greenwood and Williamson [27] in modelling the rough surface as a set of identical spherical asperities of radius R whose peak heights follow a Gaussian distribution with standard deviation h_{rms}, but who used the JKR solution of Section 1.2 to describe the individual asperity contacts. They predicted that the pull-off force should decrease drastically with h_{rms} and that this

effect is characterized by the dimensionless parameter

$$\theta_{FT} = \frac{h_{\text{rms}}^{3/2} E^*}{R^{1/2} \Delta\gamma} \tag{1.7}$$

where we note that $\Delta\gamma/E^*$ defines a characteristic adhesion length which for contact of similar materials is related to ε of equation 1.1.

1.3.4 Fractal surfaces

Naturally generated surfaces have fractal properties. To describe this fractal property, Majumdar and Bhushan described the rough surfaces as Weierstrass–Mandelbrot function. However, the wavenumber of rough surfaces is rather continuous, resulting in power law type of PSD,

$$C(\zeta_x, \zeta_y) = \begin{cases} C_0, & \zeta_L < \sqrt{\zeta_x^2 + \zeta_y^2} < \zeta_0 \\ C_0 \left(\frac{\sqrt{\zeta_x^2 + \zeta_y^2}}{\zeta_0} \right)^{-2(H+1)}, & \zeta_0 < \sqrt{\zeta_x^2 + \zeta_y^2} < \zeta_1 \\ 0\,, & \sqrt{\zeta_x^2 + \zeta_y^2} > \zeta_1 \end{cases} \tag{1.8}$$

as shown in Fig. 1.6, where ζ_x and ζ_y are the wavenumber for x and y directions. If the surface is isotropic, the PSD is the function only of ζ. Roll-off wavenumber is introduced, because surface manufacturing polish the rough surface in engineering field. Also, with the roll-off wavenumber, the height distribution of the rough surface is more close to Gaussian.

The power-law segment in equation (1.8) typically extends over three or four decades so the roughness has a profound 'multiscale' character and is "self-affine" (a generalization of the concept of "self-similarity"), i.e. with a proper rescaling of in-plane and normal coordinates its statistical properties are insensitive to the length scale at which the roughness is observed (Fig. 1.8). The slope in the power-law range is characterized by the Hurst exponent H, or equivalently by the fractal dimension

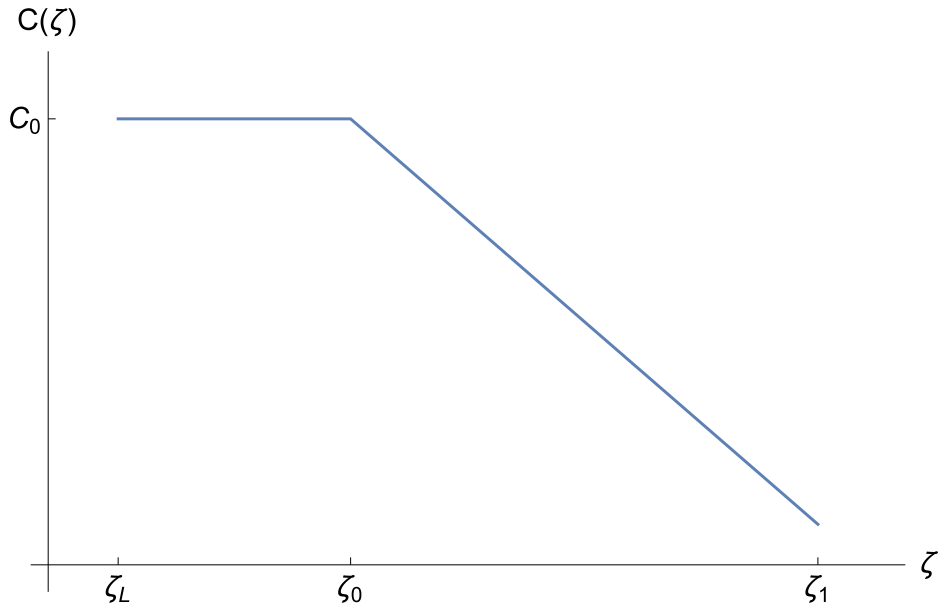

Figure 1.7: Log-log plot of the typical spectrum of surface roughness which is used today to model idealized nominally flat Gaussian rough fractal surfaces.

$D = 3 - H$.

Variance of the surface height, gradient, and curvature are written as m_0, m_2, and m_4 each in general. The spectral moments can be obtained from the PSD in Equation 1.9. While m_0 is converged as ζ_1 goes to infinity, the other two moments diverge to infinity. m_2 and m_4 heavily depend on upper wavenumber.

$$\begin{aligned} m_0 &= 2\pi \int_0^\infty \zeta C(\zeta) d\zeta \\ m_2 &= \pi \int_0^\infty \zeta^3 C(\zeta) d\zeta \\ m_4 &= \tfrac{3\pi}{4} \int_0^\infty \zeta^5 C(\zeta) d\zeta \end{aligned} \tag{1.9}$$

Thus the asperity radii continue to decrease down to atomic scales, where asperities are defined by only a few atoms. This resolution-dependence has been much criticized, and in the fractal limit it means that no real surface should be contacted independently on the rms amplitude of roughness in the asperity models, a result which looks paradoxical.

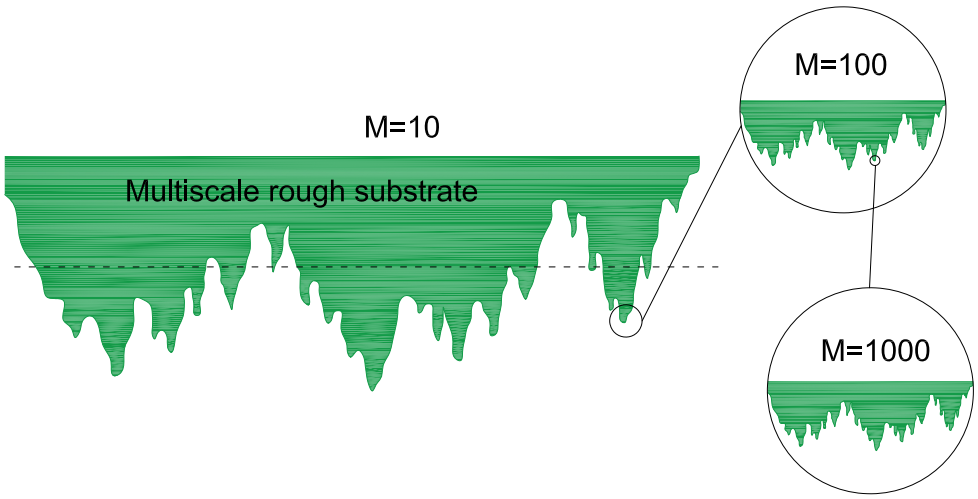

Figure 1.8: Fractal character of self-affine rough surfaces. After a proper rescaling of in-plane and normal coordinates, the statistical properties of roughness are insensitive to the length scale at which they are observed ($M = \zeta_1/\zeta_0$, "magnification").

1.4 Persson's model without adhesion

CDBJ extended Archard's concepts in Section 1.3.4 to the Weierstrass series, and found a paradoxical fractal 'limit' in which the contact is restricted to an infinite number of infinitesimal contact areas, each sustaining an infinite contact pressure. This anticipated Persson's 'resolution-dependent' solution [28] of the adhesionless rough contact problem which at low nominal pressures p_{nom} predicted that the total actual contact area A_c is given by

$$\frac{A_c}{A_{nom}} = \text{erf}\left(\frac{p_{\text{nom}}}{E^*}\frac{1}{\sqrt{m_2}}\right) \tag{1.10}$$

where A_{nom} is the 'nominal' or 'apparent' contact area and m_2 is the second moment of the height PSD in Equaiton 1.9. This dependence on rms slope is sensitive to the PSD truncation, so [e.g.] $A_c \to 0$ as $\zeta_1 \to \infty$ in Equation 1.10 [29]. Surprisingly, an

identical result is obtained from asperity models [30] except for the exact prefactor for small load, and this result caused quite a discussion in the literature [31, 32].

An arguably more important conclusion for adhesionless contact due to Persson [33] is that some macroscopic relationships, notably that between load and displacement, tend to a converged result in the fractal limit, whereas asperity model theories remain ill-posed as a result of neglecting interaction effects unless these are introduced numerically [34]. Particularly rapid convergence is found for the important case of low fractal dimension. Specifically, for $D \simeq 2.2$ Persson [33] gives

$$\frac{p_{\text{nom}}(g)}{E^*} \simeq \zeta_0 h_{\text{rms}} \exp\left(\frac{-\bar{g}}{\gamma h_{\text{rms}}}\right) \tag{1.11}$$

where $\bar{g}$ is the mean separation, $\gamma \simeq 0.5$ and $h_{\text{rms}} = \sqrt{m_0}$ is the rms height, which depends only weakly on the truncation ζ_1. Another relationship that is only weakly dependent on fine scale roughness is that between electrical contact resistance and nominal pressure [35].

Equations (1.11, 1.10) are exemplary of two types of result in the contact of fractal rough surfaces: those that are determined primarily at the coarse scale and that are therefore not sensitive to measurement resolution, and those that are not convergent and that give paradoxical predictions when ultrafine scale features are included.

1.5 Numerical methods

Contact problems can be solved with the Boundary element method [BEM] for nodal contact tractions, based on elasticity for a semi-infinite solution. It solves Fredholm's integral equation with discretization, a convolution of Green's function. For adhesiveless contact problems, to satisfy the contact Signorini condition, the contact region is iteratively defined. One way to approximate the contact regions is to put an imaginary surface as a penalty function. The imaginary surface has large enough

stiffness to depict the adhesiveless contact law, making the convergence problem remain. The convergence problem is solved by adapting the molecular dynamics [MD] algorithm as the penalty, describing problems more realistically since the interaction occurs at the molecular level. This method combining the BEM with MD is called Green's function molecular dynamics [GMFD]. While the computational complexity of the BEM is $O(n^2)$, that of GFMD is $O(n\sqrt{n}\log n)$ [36]. Theoretical predictions are generally compared with the numerical solution, which are typically obtained over a rectangular grid with initial nodal heights chosen to approximate a surface with the PSD of the equation 1.8. However, computational considerations place limits on the practical mesh refinement, so that even the most sophisticated codes such as those of Pastewka and Robbins [37] and that used in Müser's recent 'Contact Challenge' [38] can only describe surfaces with PSDs spanning about three decades — e.g., nanometer to micrometer scales.

The 'Contact Challenge' dealt with one contact problem for a given rough surface. In the paper, roughness parameters were defined, and authors were invited to submit their predictions without knowing the solution obtained in a computer-intensive numerical simulation. Then, it is published with comparisons of theory with [numerical] experiments in [39]. It contains relations between contact area, gap, and pressure. While the asperity-based models showed less accuracy to reference data (*i.e.* molecular dynamics simulations), the fractal-based model such as Persson's model with correction factors agreed well. well.

1.6 Overview of the Dissertation

In the 2nd chapter, we addressed contact between rough surfaces by tracking the evolution of the probability density function for the gap as roughness is added incrementally from coarse to fine-scale. The suggested model is a modified version of Persson's model in that the Lennard-Jones law is used instead of classical non-adhesive

contact mechanics. We found that the gap probability density function converged at large wavenumbers, in contrast to non-adhesive contact theories (Equation 1.10), which typically require arbitrary truncation of the roughness spectrum. However, this method had difficulty in that it can only be applied to fine-scale roughness since long-wavelength sinusoids exhibit a contact instability associated with the Lennard-Jones law's maximum negative slope.

In the 3rd chapter, we developed a method that can circumvent the difficulty in Chapter 2. We suggested that the fine-scale roughness could be characterized by a modified [reduced] interface energy, which could then be used in a JKR formulation of the remaining [macroscopic] contact features. Instead, if we use the method to determine the entire modified traction law, we can then use this to replace the Lennard-Jones law in determining the effect of the next lower tranche of the power spectrum density. Since the maximum negative slope of the modified law is lower than that of the Lennard-Jones law, this allows the method to be extended to longer wavelength features of the roughness. This approach can then be applied iteratively to describe the effect of an extended roughness spectrum.

In the 4th chapter, we discussed the instabilities of thin elastic plane layers. Any adhesive laws exhibit a range in which the slope is negative. The negative spring can trigger elastic instability. Based on an energetic argument, for $\nu \leq 0.25$ the unstable response comprises a sudden jump in and out during loading and unloading. For $\nu > 0.25$, infinitesimal sinusoidal perturbations on the plane surface are unstable, and the most unstable wavelength is approximately three times layer thickness, resulting in a regular pattern with the characteristic wavenumber. Once the instability occurs, the traction curves for loading and unloading are different, implying a hysteretic energy loss.

In the 5th chapter, we discussed the effect of roughness on the pattern instability in the fourth chapter. With the large roughness, the onset of instability is more chal-

lenging to define. One approach is to monitor the amplitude of the power spectrum density near the characteristic wavelength, three times the layer thickness. While the low root-mean-square roughness can trigger the instability, it is confirmed that the moderate to large root-mean-square roughness exert a stabilizing effect. We also developed a two-scale approximation. First, we estimated the effect of roughness on the mean traction from the third chapter method. The modified traction law is then used on the energetic analysis of plane surfaces from the fourth chapter. The approximation results work exceptionally well with a criterion based on the power spectrum density near the characteristic wavelength.

In the 6th chapter, we revisit the method in Chapter 3 to derive two partial differential equations from the recursive processes involving integrations over a finite tranche of power spectral density. We extend a method to adhesiveless contact by using regularized adhesiveless contact law, and compare with numerical methods and Persson's theoretical model.

CHAPTER II

Effect of Fine-Scale Roughness on the Tractions Between Contacting Bodies

2.1 Introduction

Surfaces are rarely atomically smooth and numerous authors have attempted to predict the effect of surface roughness on the contact of nominally plane surfaces. Many of these theories are based on models of the roughness as a set of non-interacting microscopic asperities, following the seminal contribution of Greenwood and Williamson [40]. These theories have enjoyed considerable success in explaining the physical observation that [for example] electrical contact conductance and the frictional forces during sliding are approximately proportional to the applied normal force.

An alternative approach due to Persson [28] [see also [41, 42]] defines the function $\Phi(p)$ representing the probability that an arbitrary point on the interface should be in contact at a given pressure p, for a surface whose power spectral density [PSD] $P_S(k)$ is truncated at some upper cutoff k. An expression is then developed for the

Chapter 2 is reproduced from the publication:
Joe, Junki, M. Scaraggi, and J. R. Barber. "Effect of fine-scale roughness on the tractions between contacting bodies." *Tribology International* 111 (2017): 52-56.

incremental change in $\Phi(p)$ due to the inclusion of an additional increment Δk of the PSD, and the effect of the entire PSD is obtained by iteration or integration. This theory is also very successful at predicting important features of the contact problem (for example, as observed in molecular and finite element simulations of particular cases [37]).

Aficionados of either theory tend to be dismissive of the claims of the other, but despite their differing approaches, the two theories often lead to surprisingly similar predictions. For example, Bush [30] used predictions of asperity heights and curvatures from profile measurements to determine parameters for an asperity model and showed that at sufficiently low nominal pressures p_{nom}, the proportion of the nominal area A_{nom} in actual contact is approximated by

$$\frac{A}{A_{\text{nom}}} \approx \frac{p_{\text{nom}}}{E^*}\sqrt{\frac{\pi}{m_2}}\ , \tag{2.1}$$

where E^* is the composite elastic modulus defined by

$$\frac{1}{E^*} = \frac{(1-\nu_1)^2}{E_1} + \frac{(1-\nu_2)^2}{E_2}\ , \tag{2.2}$$

and m_2 is the mean square slope of the profile given by

$$m_2 = \int_{-\infty}^{\infty} k^2 P_P(k)dk = \pi \int_{0}^{\infty} k^3 P_S(k)dk\ , \tag{2.3}$$

where the profile PSD $P_P(k)$ is related to the surface PSD by

$$P_P(k) = 2\int_{k}^{\infty} \frac{sP_S(s)ds}{\sqrt{s^2-k^2}} \tag{2.4}$$

[43]. The corresponding prediction from Persson's theory is

$$\frac{A}{A_{\text{nom}}} = \int_0^\infty \Phi(p)dp \approx \frac{2p_{\text{nom}}}{E^*\sqrt{\pi m_2}} \,, \tag{2.5}$$

which has the same parametric dependence as Equation 2.1, but a numerical multiplier differing by a factor of $2/\pi$. However, qualitative differences between the two approaches are predicted when the nominal pressure is sufficient to ensure that a significant proportion of the nominal surface is in actual contact.

2.1.1 Fine-scale roughness

Real surfaces often exhibit fractal character at large k, with surface PSDs of the form

$$P_S(k) = Ck^{2D-8} \,, \tag{2.6}$$

where C is a constant and D is the fractal dimension of the surface and lies in the range $2 < D < 3$. However, if an expression of this form is substituted into Equation 2.3, the result is unbounded, so both theories predict a vanishing proportion of the nominal area in actual contact and a theoretically infinite mean contact pressure. In asperity model theories, this problem is reflected in the difficult of deciding at what scale the 'asperities' should be defined [44, 45]. Similar effects are seen in numerical studies with progressive mesh refinement [46]. Of course, fine-scale effects must ultimately be limited by plastic deformation or other failure modes of the material [47], and the continuum theory itself becomes inappropriate at length scales comparable with interatomic distances, but these arguments do not give a clear indication of the point at which $P_S(k)$ should be truncated.

2.1.2 Contact, separation and adhesive tractions

The difficulty with both approaches arises principally from the sharp distinction between contact and separation assumed in conventional contact mechanics. If this is relaxed through the use [say] of the Lennard-Jones traction law for contact interactions, it seems clear that the high frequency, low amplitude components of the PSD Equation 2.6 will have decreasing influence on the probability distribution function [PDF] for pressure $\Phi(p)$. By contrast, if these waves are forced into contact at zero gap, the incremental variance of contact pressure required increases without limit in proportion with the mean surface slope.

The Lennard-Jones law involves regions of tensile as well as compressive tractions and hence opens the vexed question of the influence of surface roughness on the maximum nominal tensile traction [the 'pull-off traction'] that can be supported by an interface between two otherwise plane surfaces. Fuller and Tabor [48] extended Greenwood and Williamson's model by using the 'JKR' solution [10] for each pair of interacting asperities, but the JKR theory also depends upon there being a sharp distinction between regions of contact and separation. This implies a singularity in tensile tractions at the edge of the contact region, and hence the occurrence of a finite region in which the assumed tractions exceed the theoretical strength of the materials. Tabor [14] has shown that this is an acceptable approximation for the contact of spheres only when the Tabor parameter

$$\mu = \left(\frac{R(\Delta\gamma)^2}{E^{*2}\epsilon^3} \right)^{1/3} \gg 1 \ , \tag{2.7}$$

where R is the radius of the sphere, $\Delta\gamma$ is the interface energy, and ϵ is a measure of the range of interatomic forces. Clearly this criterion will fail when asperities are defined at a sufficiently fine scale.

Persson and Scaraggi [2] investigated the effect of surface roughness using the so-

called 'DMT' approach, in which the adhesive tractions in the separation region are estimated based on the gap that would occur in the absence of such tractions (found in this case using Persson's theory). Greenwood [17] argues that the DMT approach is not a true asymptotic solution for $\mu \ll 1$ and offers an alternative 'semi-rigid' theory in which the gap is first estimated assuming the bodies to be rigid [7], but the tractions associated with this gap are then allowed to deform the body elastically. However, this approach fails for a Gaussian rough surface, since there is then a small but finite probability of an asperity or a region of the surface having an arbitrarily large height, so two statistically rough rigid bodies could theoretically never be made to approach each other.

In this chapter, we shall attempt to resolve these difficulties by developing a theory modelled on Persson's approach, but including the modulation between contact and separation associated with the Lennard-Jones law. In particular, we shall introduce the effect of each small increment in the surface PSD using a linearized solution for the combined effect of elastic deformation and Lennard-Jones gap-dependent tractions. With this approach, we shall show that the probability distribution tends to a limit at large k, so no truncation of the PSD is necessary. The same method also allows the influence of the infinite 'tail' of the PSD on the relation between mean traction and mean gap to be estimated, suggesting a procedure for extending the JKR approach to surfaces with quasi-fractal roughness.

2.2 Theoretical model

We assume that the tractions σ [tensile positive] between two atomically plane surfaces are defined by the integrated Lennard-Jones law

$$\sigma(g) = \frac{8\Delta\gamma}{3\epsilon}\left(\frac{\epsilon^3}{g^3} - \frac{\epsilon^9}{g^9}\right) \tag{2.8}$$

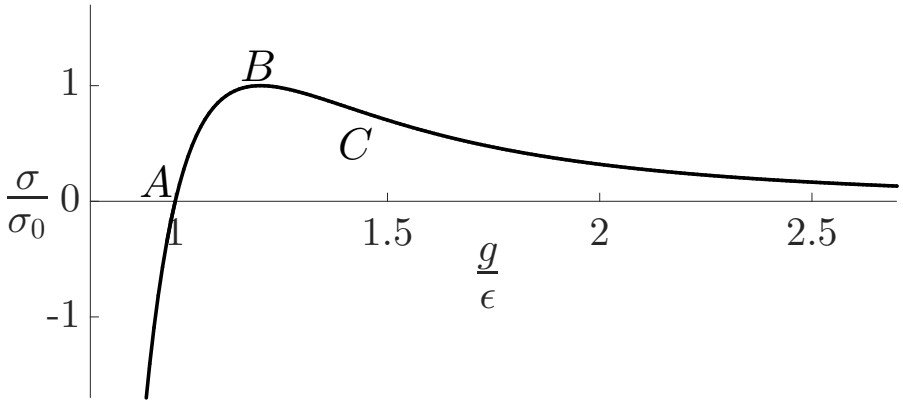

Figure 2.1: The Lennard-Jones force law.

[obtained through the application of the Derjaguin approach], where g is the local value of the gap (separation) between the surfaces, $\Delta\gamma$ is the interface energy and ϵ is the separation at which two unloaded bodies with plane surfaces would be in equilibrium. This relation is illustrated in Figure 2.1, where σ is normalized by the maximum tensile traction [the theoretical strength]

$$\sigma_0 = \frac{16\Delta\gamma}{9\sqrt{3}\epsilon} \,, \tag{2.9}$$

which occurs at B, where $g = 3^{1/6}\epsilon \approx 1.201\epsilon$. The relation between ϵ and crystal lattice parameters is discussed by Yu and Polycarpou [49].

2.2.1 Contact problem for a single sine wave

We first consider the simpler problem in which the gap g contains a single sinusoidal wave of amplitude g_1 and wavenumber k, so that

$$g(x) = g_{\text{ave}} + g_1 \cos(kx) \,, \tag{2.10}$$

where g_{ave} is the mean separation.

Equation 2.8 and Figure 2.1 define a non-linear relation, so the resulting con-

tact pressure $p(x)$ will not be sinusoidal. However, if $g_1/\epsilon \ll 1$, we can linearize Equation 1.1 about the mean value g_{ave}, obtaining

$$p(x) = -\sigma\left(g(x)\right) \approx \bar{p} + p_1 \cos(kx) \ , \tag{2.11}$$

where

$$\bar{p} = -\sigma\left(g_{\text{ave}}\right) \ ; \quad p_1 = -g_1 \left(\frac{\partial \sigma}{\partial g}\right)_{g=g_{\text{ave}}} \ . \tag{2.12}$$

The sinusoidal component will produce normal elastic displacements

$$u(x) = u_1 \cos(kx) \quad \text{where} \quad u_1 = \frac{2p_1}{E^* k} \tag{2.13}$$

(Johnson, 1985) and these increase the final gap $g(x)$, so we conclude that the original undeformed surface must have contained a sinusoidal perturbation of amplitude $h_1 = g_1 - u_1$. Using Equation 2.8 to evaluate the derivative in Equation 2.12, we obtain

$$g_1 = f(\tilde{g}, \tilde{k}) h_1 \quad \text{where} \quad f(\tilde{g}, \tilde{k}) = \left[1 + \frac{1}{\tilde{k}} \left(\frac{9}{\tilde{g}^{10}} - \frac{3}{\tilde{g}^4}\right)\right]^{-1} \tag{2.14}$$

and we have introduced the dimensionless parameters

$$\tilde{g} = \frac{g}{\epsilon} \ ; \quad \tilde{k} = \frac{3\epsilon^2 E^* k}{16 \Delta\gamma} \equiv \chi k \ ; \quad \tilde{P}_S(\tilde{k}) = \frac{P_S(k)}{\epsilon^2 \chi^2} \ . \tag{2.15}$$

Notice that the dimensionless wavenumber has obvious similarities to the Tabor parameter of Equation 2.7 and we could define an equivalent Tabor parameter using the radius of the peaks of the sine wave for R. It is also worth remarking that for the contact of similar materials, the slope of the Lennard-Jones relation Equation 2.8 at the equilibrium point A in Figure 2.1 is related to the elastic modulus E [50]. For this case, if $\nu = 0$, the dimensionless wavenumber $\tilde{k} \approx 3k\epsilon$.

2.2.2 A 'small' packet of uncorrelated sine waves

We next consider the case where the surfaces are nominally plane with constant separation $\tilde{g}_0$, and we add an isotropic packet of uncorrelated sine waves whose wavenumbers lie in a band $(\tilde{k}, \tilde{k} + \Delta\tilde{k})$. If the total energy in this band is sufficiently small, the PDF of the resulting gap $\tilde{g}$ will have the Gaussian form

$$\Phi(\tilde{g}, \tilde{g}_0, \tilde{k}, \Delta\tilde{k}) = \frac{1}{\sqrt{2\pi V}} \exp\left(-\frac{(\tilde{g} - \tilde{g}_0)^2}{2V}\right) \tag{2.16}$$

[51], with variance

$$V(\tilde{g}_0, \tilde{k}, \Delta\tilde{k}) = 2\pi \int_{\tilde{k}}^{\tilde{k}+\Delta\tilde{k}} s\tilde{P}_S(s) f(\tilde{g}_0, s)^2 ds \ . \tag{2.17}$$

This argument depends on V being sufficiently small for $f(\tilde{g}, \tilde{k})$ to be considered constant in the range where $\Phi(\tilde{g})$ is not negligible [e.g. in $\tilde{g}_0 - 5\sqrt{V} < \tilde{g} < \tilde{g}_0 + 5\sqrt{V}$]. Intuitively, the resulting error should tend to zero as $\Delta\tilde{k} \to 0$, and we shall show in Section Equation 2.3.1.1 that a corresponding numerical iterative solution for a given $\tilde{P}_S(\tilde{k})$ converges on a unique result in this limit.

2.2.3 Integration over an extended PSD

We interpret Equation 2.16 as defining the *conditional* probability $\Phi(\tilde{g}|\tilde{g}_0)$ of a point at separation $\tilde{g}_0$ being at $\tilde{g}$ after the addition of the wave packet $\Delta\tilde{k}$. This involves the assumption that the conditional probability depends only on the local value of $\tilde{g}_0$ and hence is the same as would be obtained if the entire surface were at $\tilde{g}_0$. However, this is not very different from the assumption in Persson's theory [28, 42] that the conditional probability $\Phi(p|p_0)$ for contact pressure is given by the full contact solution, since this implies that it is uninfluenced by the possible [and indeed likely] nearness of regions of separation.

If the PDF of $\tilde{g}$ for the case where the surface PSD is truncated at $\tilde{k}$ is denoted by $\Phi(\tilde{g}, \tilde{k})$, we can determine the corresponding expression after the addition of the wave packet $\Delta\tilde{k}$ as

$$\Phi(\tilde{g}, \tilde{k} + \Delta\tilde{k}) = \int_0^\infty \Phi(\tilde{g}_0, \tilde{k}) \Phi(\tilde{g}|\tilde{g}_0) d\tilde{g}_0 = \int_0^\infty \frac{\Phi(\tilde{g}_0, \tilde{k})}{\sqrt{2\pi V}} \exp\left(-\frac{(\tilde{g} - \tilde{g}_0)^2}{2V}\right) d\tilde{g}_0 \,. \quad (2.18)$$

This relation can then be applied iteratively to determine $\Phi(\tilde{g})$ due to an extended PSD.

Notice that the theory developed here differs from that of Persson [28] in that from the beginning we track the evolution of the probability distribution $\Phi(\tilde{g})$ of the gap $\tilde{g}$, rather than that of the contact pressure p. We make this choice because the Lennard-Jones traction $\sigma = -p$, illustrated in Figure 2.1, is a single-valued function of g, whereas for $0 < \sigma < \sigma_0$, g is a multi-valued function of p, so the probability $\Phi(p)$ entails some ambiguity as to which branch is in question. Almqvist *et al.* [52] developed expressions for $\Phi(g)$, but these were derived from $\Phi(p)$ using a strain energy argument, and assumed a sharp transition from contact to separation without traction.

2.2.4 Negative stiffness and instability

The function $f(\tilde{g}, \tilde{k})$ of Equation 2.14 is negative for

$$\tilde{k} < \frac{3}{\tilde{g}^4} - \frac{9}{\tilde{g}^{10}} \,, \quad (2.19)$$

implying that a single sine wave of infinitesimal amplitude in the original profile would result in a sinusoidal gap that is 180 deg out of phase. In effect, the system exhibits negative stiffness in this range and the resulting solution would clearly be unstable. Instead we should anticipate a jump to one of two stable states that are not within an infinitesimal neighbourhood of the original perturbation.

In fact, if two *plane* surfaces of (say) square planform of side $2\pi/k$ are brought to a mean separation $\tilde{g}$ in the range defined by Equation 2.19, it is energetically favourable for a sinusoidal perturbation to form spontaneously. However, the maximum value of the right-hand side of Equation 2.19 occurs at $\tilde{g} = \sqrt[6]{15/2}$ and is $\tilde{k}_0 = \sqrt[3]{324/3125} \approx 0.470$, so this instability is precluded if we restrict attention to roughness spectra in the 'fine-scale' range $\tilde{k} > \tilde{k}_0$.

To place this value in perspective, we note that the (dimensional) peak radius of the sinusoid $h\sin(k_0 x)$ of amplitude h is $R = 1/hk_0^2$. If this value is used in the definition of the Tabor number Equation 2.7, we obtain

$$\mu \approx 0.542\sqrt[3]{\frac{\epsilon}{h}}\,. \tag{2.20}$$

Thus, k_0 can also be interpreted as the wavenumber above which the JKR methodology would be inappropriate for a single sine wave of amplitude $h \sim \epsilon$.

2.3 Results

We first consider the case where the PSD has the quasi-fractal form of Equation 2.6 with lower and upper cutoff frequencies k_1, k_2 respectively. We start from the condition where the surface is plane so that the separation is everywhere constant and equal to g_{ave}, and hence $\Phi(\tilde{g}) = \delta(\tilde{g} - \tilde{g}_{\text{ave}})$, where $\delta(\cdot)$ is the Dirac delta function. We then add wave packets $\Delta\tilde{k}$ sequentially using equations Equation 2.18, Equation 2.17 until the entire PSD has been added.

2.3.1 Convergence tests

2.3.1.1 Choice of $\Delta\tilde{k}$

We argued in Section 2.2.2 that Equation 2.16 is strictly correct only when V is 'sufficiently small', which here places a restriction on the value of $\Delta\tilde{k}$. For a given

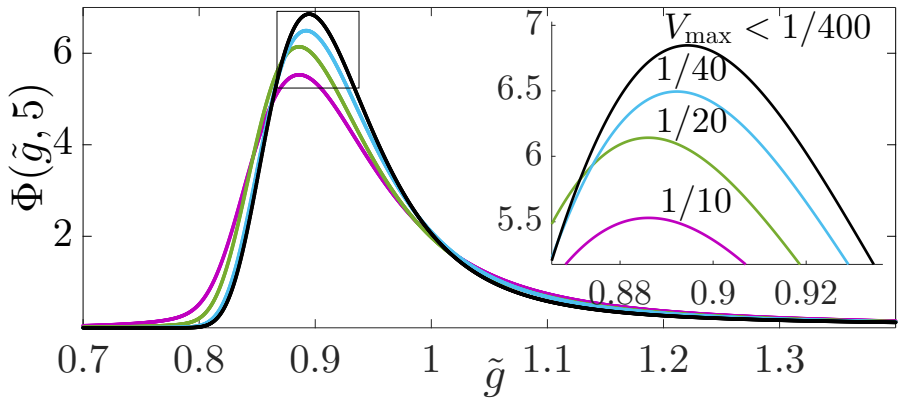

Figure 2.2: Effect of maximum wave packet variance $V_{\max}$ on the convergence of the process.

value of $\Delta\tilde{k}$, $V(\tilde{g}, \tilde{k}, \Delta\tilde{k})$ is a function of $\tilde{g}$ with the maximum value occurring at $\tilde{g}_0 = \sqrt[6]{15/2}$. We therefore anticipate that numerical convergence will be approximately characterized by the parameter $V_{\max} = V(\tilde{g}_0, \tilde{k}, \Delta\tilde{k})$

Figure 2.2 presents numerical calculations for the resulting PDF obtained with various values of this parameter, for the case where $\tilde{g}_{\text{ave}} = 0.98, \tilde{k}_1 = 1, \tilde{k}_2 = 5$ and the PSD is given by the dimensionless equivalent of Equation 2.6 with $D = 2.5$ and a multiplying constant $C = 1/\pi$. The results show that the PDF does indeed converge as $\Delta\tilde{k}$ is reduced, and the curves for values below $V_{\max} = 1/400$ are virtually indistinguishable, suggesting that this is an acceptable degree of discretization.

2.3.1.2 Convergence at large $\tilde{k}_2$

Figure 2.3 shows results obtained for the same PSD and mean gap $\tilde{g}_{\text{ave}}$, but different values of the upper cutoff frequency $\tilde{k}_2$. Notice that there is significant evolution of the PDF as $\tilde{k}_2$ is increased, but the curves become almost identical beyond $\tilde{k}_2 = 580$, showing that the process converges as surmised in the Introduction. It follows that with this strategy, it is not necessary to impose an arbitrary truncation on the PSD.

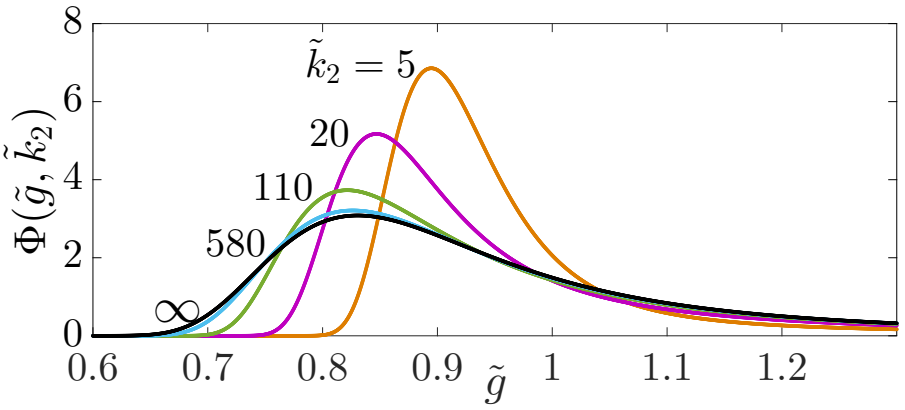

Figure 2.3: Effect of upper cutoff frequency $\tilde{k}_2$ on $\Phi(\tilde{g})$.

2.4 Relation between mean gap and nominal traction

Once the probability distribution function $\Phi(\tilde{g})$ has been determined, the nominal (mean) traction $\bar{\sigma}$ can be obtained as

$$\bar{\sigma} = \int_0^\infty \Phi(\tilde{g})\sigma(\tilde{g})d\tilde{g} \ , \tag{2.21}$$

where $\sigma(\tilde{g})$ is the Lennard-Jones traction Equation 2.8.

Figure 2.4 shows the resulting nominal traction, normalized by the maximum Lennard-Jones tensile traction σ_0, as a function of the mean gap $\tilde{g}_{\text{ave}}$, for the PSD Equation 2.6 with $\tilde{k}_1 = 1, C = 1/\pi, D = 2.5$ and $\tilde{k}_2 \to \infty$. Notice that the resulting figure is qualitatively similar to that of the original L-J law of Figure 2.1, but with two notable differences: (i) the maximum tensile value is significantly lower than unity, and (ii) the equilibrium point [where $\bar{\sigma} = 0$] is shifted to a value $\tilde{g}_{\text{ave}} > 1$. This shift is a consequence of the high stiffness of the surface to high frequency waves. At modest nominal compressive tractions, only the peaks of the distribution come within range of L-J tractions and hence the mean planes are more separated relative to similar loading of two plane surfaces. For a given (dimensional) PSD, this mean-plane shift increases with E^* and of course would be theoretically infinite in the rigid-body

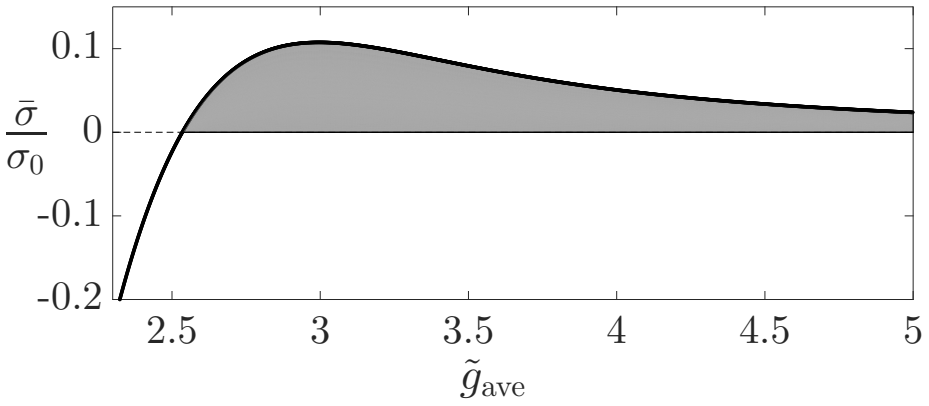

Figure 2.4: Relation between mean traction $\bar{\sigma}$ and mean gap $\tilde{g}_{\text{ave}}$ for $\tilde{k}_1 = 1, C = 1/\pi, D = 2.5$ and $\tilde{k}_2 \to \infty$.

(Bradley) limit [53], since the rough surface has no highest point. The modified force law of Figure 2.4 preserves the $\tilde{g}_{\text{ave}}^{-3}$ behaviour of the L-J law at large $\tilde{g}_{\text{ave}}$, but is not of power law form in the compressive range.

The shaded area in Figure 2.4 is proportional to the work that must be done per unit nominal area in order to separate the contacting rough surfaces from the equilibrium position. Thus it can be seen as a measure of interface energy $\Delta\gamma$, as modified [reduced] by the presence of fine-scale roughness $\tilde{k} > \tilde{k}_1$. Figure 2.5 shows the magnitude $\Delta\gamma_{\text{eff}}$ of this modified interface energy and also the maximum pull-off traction $\bar{\sigma}_{\max}$ as a function of the dimensionless variance of the fine-scale roughness $\tilde{m}_0 = m_0/\epsilon^2$, where

$$m_0 = 2\int_0^\infty P_P(k)dk = 2\pi\int_{k_1}^\infty kP_S(k)dk \ . \tag{2.22}$$

Notice that the more usual RMS roughness measure is equal to $\sqrt{m_0}$. Both $\Delta\gamma_{\text{eff}}$ and $\bar{\sigma}_{\max}$ are normalized by the plane surface values and hence tend to unity for $m_0 = 0$.

Persson and Scaraggi [2] define the related quantity $\gamma_{\text{eff}}(\bar{\sigma})$ as the work done per unit area in separating two surfaces currently loaded by a mean traction $\bar{\sigma}$. They estimated it using the 'DMT' approach, in which the gap [or in this case $\Phi(g)$] is

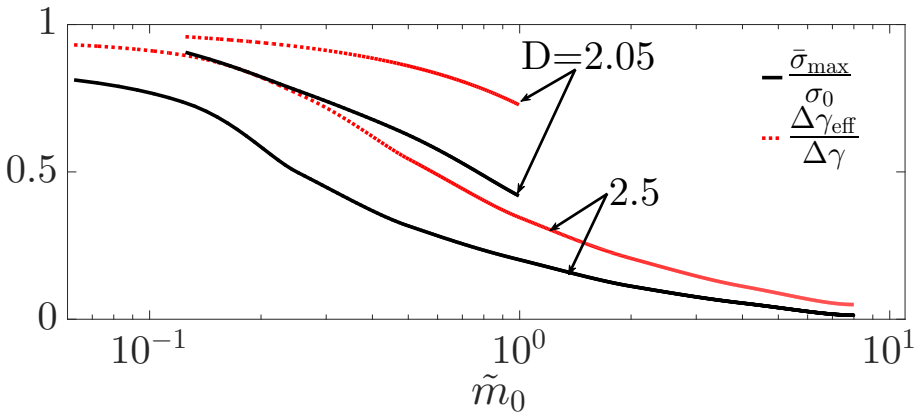

Figure 2.5: Effect of fine-scale roughness on the effective interface energy $\Delta\gamma_{\text{eff}}$ and pull-off traction $\bar{\sigma}_{\max}$. Here $D = 2.05, 2.5$, $\tilde{k}_1 = 0.5$ and the height variance m_0 is changed through the constant C in Equation 2.6.

estimated based on a classical 'hard-contact' elastic model without adhesive tractions. The van der Waals' tractions associated with this gap are then summed and added to the total compressive force in the contact region to obtain the total contact force. The quantity $\Delta\gamma_{\text{eff}}$ plotted in our Figure 2.5 is essentially $\gamma_{\text{eff}}(0)$. In other words, it is the work done in separating the bodies from the equilibrium position, where $\bar{\sigma} = 0$.

The results in Figure 2.5 show that adhesive tractions fall off more rapidly with increasing m_0 when the fractal dimension D is larger. This is consistent with results for conventional truncated PSDs, since an increase of D at constant m_0 would then imply an increase in the surface slope variance m_2, as reported [for example] by Pastewka and Robbins [37]. Notice however that for an untruncated fractal PSD m_2 is theoretically infinite, so a criterion based on surface slopes [rather than fractal dimension] is critically dependent on the upper cutoff k_2.

2.5 Comparison with a discrete numerical model

In order to assess the effect of the approximations inherent in the solution, we compared the results in particular cases with the numerical model described in the Appendix of [2]. A square domain is discretized using a uniform square mesh and the

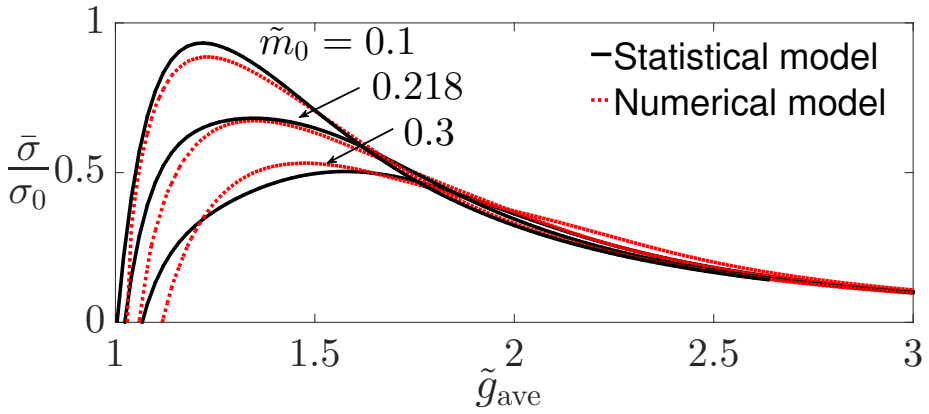

Figure 2.6: Comparison of the predicted mean traction $\bar{\sigma}$ as a function of mean gap $\tilde{g}_{\text{ave}}$ using the present statistical method and the numerical method of [2]. Results are presented for $\tilde{k}_1 = 1, \tilde{k}_2 = 8, D = 2.2$ and three values of the dimensionless height variance $\tilde{m}_0 = m_0/\epsilon^2$.

tractions at each grid point are defined by the Lennard-Jones law of Equation 2.8. The corresponding elastic deformations due to these tractions are determined by inversion of the elastic solution in Fourier space, which therefore implies periodic boundary conditions on the modelled domain. The combined [elastic + L-J] displacements at each point are required to satisfy the contact condition appropriate to a realization of the isotropic PSD Equation 2.6. The resulting set of non-linear equations is satisfied using a damped molecular dynamic algorithm. For more details, the reader is referred to [2].

Since the numerical solution is based on a particular realization of Equation 2.6, different results are obtained depending on the initial random number seed. In particular, the resulting force-displacement curve analogous to Figure 2.4 is quite sensitive to the actual maximum height in the realization. This variability would of course be reduced if computational considerations allowed a larger region of the surface to be modelled. In Figure 2.6, we compare the predictions of the present statistical algorithm with the average of four numerical realizations for the normalized mean traction $\bar{\sigma}/\sigma_0$, for three values of the height variance and $D = 2.2, \tilde{k}_1 = 1, \tilde{k}_2 = 8$.

2.6 A hybrid JKR theory

Many treatments of adhesive contact problems make use of the JKR formalism [48, 54, 55], since it is amenable to analytical solution, whereas a solution using the full Lennard-Jones traction law almost invariably requires numerical solution and even then the resulting problem can be quite challenging.

The present method opens up the possibility of decoupling the effect of fine-scale roughness [where the effective Tabor number is too small for the JKR approach to be reasonable], from coarse scale features. We first determine the reduced interfacial energy due to the fine-scale roughness $k > k_1$ using the methodology of Section 2. The rest of the profile, comprising roughness in the range $k < k_1$ and any macroscopic features of the contacting bodies can then be used to define a contact problem using the JKR formalism, but with $\Delta\gamma$ replaced by $\Delta\gamma_{\text{eff}}$.

2.7 Conclusions

We have described a procedure based on Persson's theory of rough surface contact for determining the effect of adding a small increment of the truncated PSD on the resulting probability distribution for the gap g, including contributions from elastic deformation and from the Lennard-Jones interfacial traction law. The L-J law is used throughout the compressive and tensile range and hence this theory does not include regions of 'hard' compressive contact where further variation of gap is impossible. As a result, the solution converges at large wavenumbers, in contrast to hard contact theories which generally require the PSD to be somewhat arbitrarily truncated.

Using this method, we are able to determine the effective reduction in interfacial energy and mean pull-off traction due to the fine scale [i.e. high wavenumber] components in the PSD. These results can then be used in problems formulated using the JKR formalism.

CHAPTER III

Effect of Roughness on the Adhesive Tractions Between Contacting Bodies

3.1 Introduction

If the surfaces of two contacting bodies were perfectly smooth and plane, the tractions between them would be determined by a potential law characterizing the physics of the intermolecular forces, and in particular would exhibit a range of separations in which these tractions would be attractive. However, the inevitable presence of surface roughness weakens the adhesive tractions. Indeed, Fuller and Tabor [48] showed that even minor roughness can seriously degrade the adhesion between contacting bodies.

Many researchers have developed models to predict the effect of surface roughness on contact. Since contact is expected to be concentrated near the highest points of the two surfaces, many of these theories depend on approximating the rough surface profile by a distribution of asperities, which are then assumed to act independently. Greenwood and Williamson [40] showed that the behaviour predicted by such a model is largely determined by the height and local curvature distribution of the asperities

Chapter 3 is reproduced from the publication:
Joe, Junki, M. D. Thouless, and J. R. Barber. "Effect of roughness on the adhesive tractions between contacting bodies." *Journal of the Mechanics and Physics of Solids* 118 (2018): 365-373.

and considerable effort has been expended in extracting this information from surface profile measurements [43]. However, high resolution measurements of surface profiles show that roughness exhibits multiscale features over several decades of length scale [56]. This implies that if an asperity is defined as a point higher than its nearest neighbours, the asperity parameters and some of the predictions of the resulting model are sensitive to the resolution of the surface measuring instrument.

An alternative approach, pioneered by Persson [28], is to characterize the rough surface contact problem by the probability distribution function [PDF] $\Phi(p, k)$ for the contact pressure p at a random point, when the power spectral density [PSD] $P(k)$ of the surface roughness is truncated at some wavenumber k. The modification of $\Phi(p)$ due to the introduction of a small increment $(k, k + \Delta k)$ of the PSD is then estimated. The PDF $\Phi(p)$ due to the entire PSD can then be determined by iteration or integration. This technique was introduced earlier by Ciavarella *et al.* to investigate the contact of a surface defined by the Weierstrass profile [41].

In a previous paper [57], we introduced a modification to Persson's theory in which we (i) tracked the PDF $\Phi(g)$ for the local separation [gap] g between the surfaces rather than the contact pressure, and (ii) determined the effect of an infinitesimal increment in the PSD using a linear perturbation of the traction law between plane surfaces [5] about the local value of g. The reason for developing this theory in terms of g was that the local traction $\sigma_0[= -p]$ is always a unique function of g, whereas if a tensile range $[\sigma_0 > 0]$ exists, g is not a unique function of σ_0. This is illustrated for the Lennard-Jones traction law in Figure 3.1, but it is clearly the case for any traction law, including those we shall use in the following analysis for the mean traction between rough surfaces.

The method described in [57] gives predictions of the relation between the mean traction $\bar{\sigma}$ and mean gap $\bar{g}$ that agree closely with direct numerical simulations for cases where the roughness PSD is restricted to high wavenumbers k. However, it can-

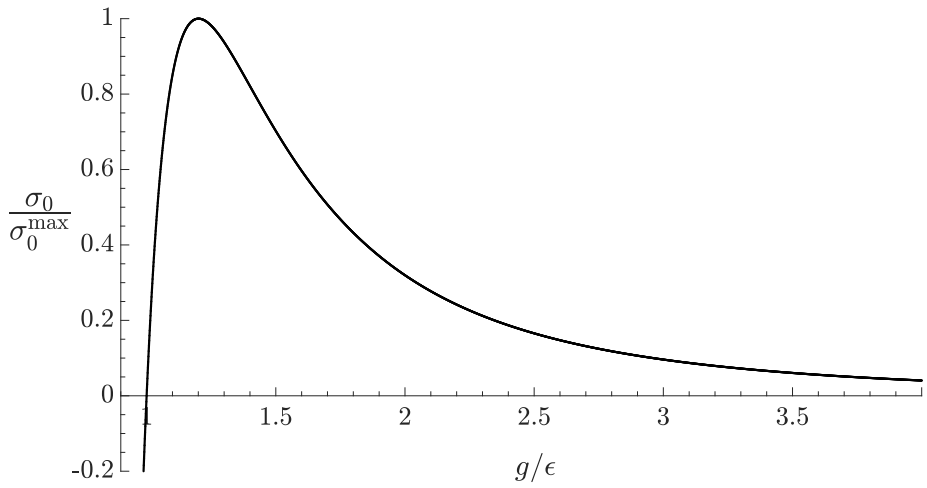

Figure 3.1: The Lennard-Jones interface traction law. The separation g is normalized by the equilibrium spacing ϵ between the surfaces.

not be extended to a broader spectrum because the incremental problem is unstable for wavenumbers that are low enough for the maximum negative slope of the traction law to exceed the positive stiffness of the contacting bodies subjected to a spatially sinusoidal traction. This is a real physical effect. [58] and [59] have shown experimentally that for thin elastic films, nominally uniform contact can bifurcate into regular patterns. An energetic analysis of this phenomenon [60, 61] predicts instabilities for layers of any thickness, including the half space, if the wavelength is sufficiently large [i.e. k sufficiently small]. An arbitrarily small perturbation of the given wavenumber [i.e. any non-zero content in the PSD in that range] is then sufficient to trigger the instability.

In this context we should note that practical contact problems necessarily involve bodies of finite dimensions, and the description of the surface in terms of a PSD [and particularly a power-law PSD] is then meaningful only for wavelengths much smaller than the linear dimensions of the macroscopic contact area. Practical surfaces are likely to exhibit stochastic and/or deterministic deviations from the plane outside this range, and these can also be expected to influence the contact morphology and hence the adhesive force law.

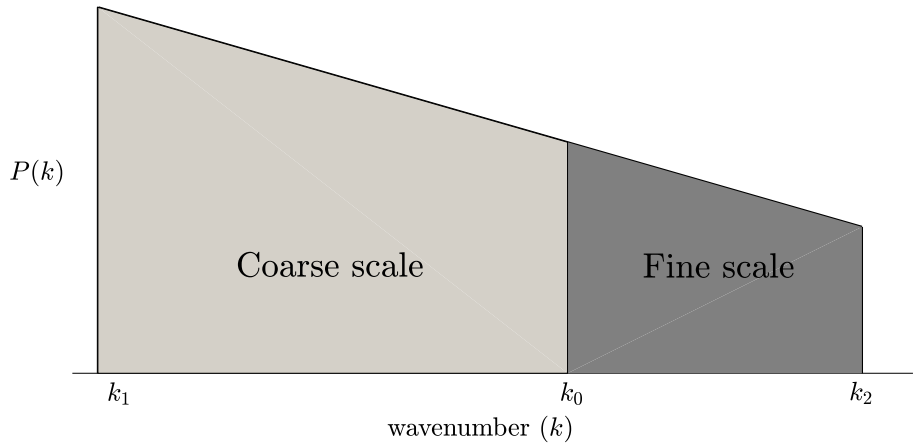

Figure 3.2: Partition of the power spectral density [PSD] into 'fine scale' and 'coarse scale' components.

In this chapter, we shall overcome this difficulty by applying the technique from [57] sequentially. To illustrate the concept, Figure 3.2 shows a representative PSD in the range $k_1 < k < k_2$ which has been arbitrarily separated into coarse-scale $[k_1 < k < k_0]$ and fine-scale $[k_0 < k < k_2]$ components. Suppose that k_0 is sufficiently large to permit the method of reference [57] to be used to determine the relation $\bar{\sigma}(\bar{g})$ for a plane surface containing *only* the fine scale roughness. We can then consider the entire PSD of Figure 3.2 as defining a surface whose PSD contains only the coarse scale roughness, but for which the interface traction law is $\bar{\sigma}(\bar{g})$ rather than $\sigma(g)$. In other words, at this stage, the coarse scale is modelled explicitly, but the effect of the fine scale is reflected in a modified traction law. Since $\bar{\sigma}(\bar{g})$ will generally have a lower maximum negative slope than $\sigma(g)$ [the fine-scale roughness attenuates the attractive tractions], this allows us to proceed to lower wavenumbers without encountering an instability in the incremental problem.

3.2 Theory

If the force between two molecules is assumed to follow the Lennard-Jones 6-12 law, the traction $\sigma_0(g)$ between two bodies bounded by plane surfaces and separated by a distance g is given by

$$\sigma_0(g) = \frac{8\Delta\gamma_0}{3\epsilon}\left(\frac{\epsilon^3}{g^3} - \frac{\epsilon^9}{g^9}\right) , \tag{3.1}$$

[5], where $\Delta\gamma_0$ is the interface energy per unit area and ϵ is the equilibrium spacing. The maximum tensile traction then occurs at $g = 3^{1/6}\epsilon \approx 1.201\epsilon$ and is

$$\sigma_0^{\max} = \frac{16\Delta\gamma_0}{9\sqrt{3}\epsilon} . \tag{3.2}$$

We shall use these results in the following derivations, but we note that the same method can be applied to any other traction law for which the function $\sigma_0(g)$ is known or assumed.

3.2.1 Probability function for gap

Suppose that a rough surface is placed near to a plane surface such that the mean gap is g, and that, in this configuration, the probability of a given point having a local gap s is $\Phi(s|g)$. The mean traction $\sigma(g)$ between the surfaces can then be found by convolution with the traction law as

$$\sigma(g) = \int_0^\infty \Phi(s|g)\sigma_0(s)ds . \tag{3.3}$$

We shall refer to $\sigma(g)$ as the *effective traction law* for a surface of the given roughness. It corresponds to the traction law that would be measured experimentally for nominally plane but actually slightly rough surfaces.

We next extend the definition of the conditional PDF such that $\Phi(s|g; k_1, k_2)$

denotes the conditional probability $\Phi(s|g)$ for the case where the roughness is defined by that part of a given PSD $P(k)$ in the range $k_1 < k < k_2$. If $P(k)$ is partitioned into two ranges as in Figure 3.2, it then follows that

$$\Phi(s|g;k_1,k_2) = \int_0^\infty \Phi(s|t;k_0,k_2)\Phi(t|g;k_1,k_0)dt \ , \tag{3.4}$$

since points that are separated by t for the PSD (k_1,k_0) will be distributed by the conditional probability $\Phi(s|t;k_0,k_2)$ when the roughness spectrum (k_0,k_2) is added.

If we now apply the operator Equation 3.3 to both sides of Equation 3.4, we obtain

$$\begin{aligned} \sigma(g;k_1,k_2) &= \int_0^\infty \int_0^\infty \Phi(s|t;k_0,k_2)\Phi(t|g;k_1,k_0)\sigma_0(s)dtds \\ &= \int_0^\infty \Phi(t|g;k_1,k_0)\sigma(t;k_0,k_2)dt \end{aligned} \tag{3.5}$$

after changing the order of integration, where

$$\sigma(t;k_0,k_2) = \int_0^\infty \Phi(s|t;k_0,k_2)\sigma_0(s)ds \tag{3.6}$$

is the effective traction law for a surface containing only the roughness in (k_0,k_2).

Clearly this argument can be applied sequentially to a PSD partitioned into any number N of tranches. At each stage, the effective traction law determined up to that point is used in place of $\sigma_0(g)$ to determine the new traction law when the next tranche is included.

3.2.2 Conditional probability

An essential stage in the procedure is the determination of the conditional probability distribution $\Phi(s|g)$ given the PSD $P(k)$ when $k \in (k_{i-1},k_i)$ and the most recent effective traction law $\sigma_i(g) = \sigma(g;k_i,k_N)$. If the added roughness is sufficiently small,

this problem can be solved as in [57], but using a local linear perturbation of the non-linear function $\sigma_i(g)$, in combination with the elastic solution for a prescribed sinusoidal traction.

The derivations are given in [57] and are omitted here in the interests of brevity. We obtain

$$\Phi(t|g; k_{i-1}, k_i) = \frac{1}{\sqrt{2\pi V}} \exp\left(-\frac{(t-g)^2}{2V}\right) , \tag{3.7}$$

where the variance

$$V = 2\pi \int_{k_{i-1}}^{k_i} kP(k) \left[1 + \frac{2}{E^* k} \frac{\partial \sigma_i}{\partial g}\right]^{-2} dk , \tag{3.8}$$

$$\frac{1}{E^*} = \frac{(1-\nu_1^2)}{E_1} + \frac{(1-\nu_2^2)}{E_2} , \tag{3.9}$$

and $E_j, \nu_j,\ j = 1, 2$ are the Young's modulus and Poisson's ratio respectively for body j. These results reduce to equations (14–17) of [57] if $\sigma_i(g)$ is replaced by the Lennard-Jones law $\sigma_0(g)$ of Equation 3.1.

3.3 Numerical solution and convergence

The procedure described above [and in particular Equation 3.7 and Equation 3.8)] depends on a linearization of $\sigma_i(t)$ about $t = g$, which should be a good approximation provided that

$$V \frac{\partial^2 \sigma_i}{\partial g^2} \ll \left[\frac{\partial \sigma_i}{\partial g} + \frac{E^* k}{2}\right] . \tag{3.10}$$

This in turn requires that the intervals (k_{i-1}, k_i) be sufficiently small, and that appropriate values can be chosen based on a conventional convergence study. However, the condition Equation 3.10 suggests that larger intervals can be used at smaller values of k to increase computational efficiency. Numerical experiments with several different PSDs showed that converged results can be obtained by choosing k_{i-1} such

that

$$\mathcal{E}(g) \equiv \frac{2m_0(\Delta k)}{E^* k_i} \left| \frac{\partial^2 \sigma_i}{\partial g^2} \right| \left[1 + \frac{2}{E^* k_i} \frac{\partial \sigma_i}{\partial g} \right]^{-3} < 2 \times 10^{-5} \tag{3.11}$$

for all g, where

$$m_0(\Delta k) = 2\pi \int_{k_{i-1}}^{k_i} k P(k) dk \tag{3.12}$$

is the height variance associated with the tranche $\Delta k = (k_{i-1}, k_i)$ of the PSD. For fractal surfaces with fractal dimension D, this leads to an approximate power-law dependence $k_i \sim i^\lambda$ with $\lambda \approx 7 - 2D$.

3.3.1 Comparison with direct numerical computations

The strength of the present method is that it can be used for broadband spectra where the ratio of upper to lower wavenumber k_N/k_1 is relatively large. Direct numerical solutions [e.g. boundary-element or finite-element studies] are limited to values of this ratio of the order of 100. Furthermore, they can only give results for particular random realizations of the underlying statistics, requiring multiple calculations to yield appropriate averages. However, as a check on the present procedure, we compared our results with numerical solutions using the 'Green's function molecular dynamics' [GFMD] code developed by Persson and Scaraggi [2] for a PSD of power-law form with a fractal dimension $D = 2.2$, $\tilde{k}_1 = 0.8, \tilde{k}_2 = 8.0$ and height variace $m_0 = 0.66\epsilon^2$, where the dimensionless wavenumber is defined by

$$\tilde{k} = \chi k \quad \text{with} \quad \chi = \frac{3\epsilon^2 E^*}{16 \Delta \gamma_0} \, . \tag{3.13}$$

Figure 3.3 shows the predicted relation between the normalized mean interface traction $\sigma/\sigma_0^{\max}$ and gap g/ϵ [solid black line] and numerical simulations using several realizations of the same PSD [thin red lines]. The present prediction lies well within the variance of these realizations, except in a range very close to the equilibrium gap,

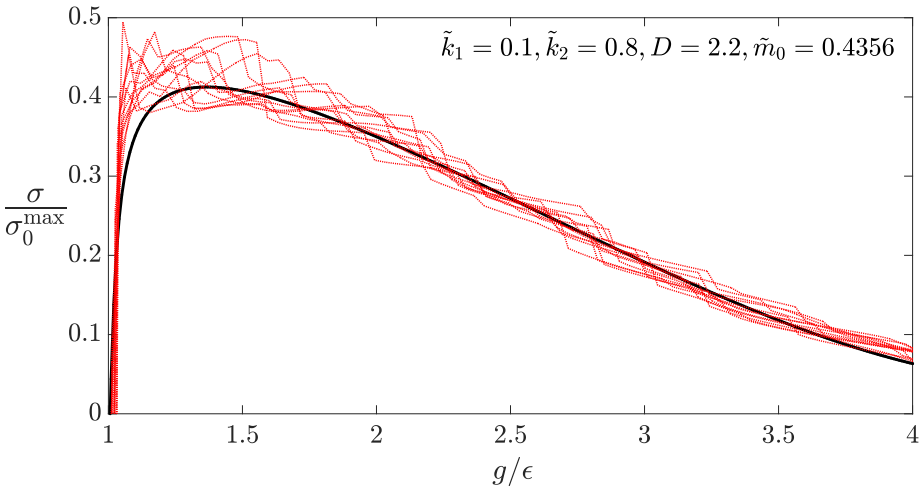

Figure 3.3: Traction law $\sigma(g)$ for contact between a nominally plane rough surface and a flat. The roughness spectrum is a power-law with fractal dimension $D = 2.2$, dimensionless wavenumbers $0.8 < \tilde{k} < 8.0$ and height variance $m_0 = 0.4356\epsilon^2$. The solid line represents the predictions of the present theory and the thin red lines represent numerical solutions using the 'GFMD' code from [2].

where the theoretical line is lower than the mean of the simulations.

For practical applications, interest is focussed mainly on the effective interface strength $\sigma^{\max}$ [the maximum value of the traction in Figure 3.3] and the effective interface energy $\Delta\gamma_{\text{eff}}$ [the area underneath the curve in Figure 3.3]. This latter term is the work per unit area needed to separate the rough surfaces from the equilibrium separation. The analytical predictions for these quantities using the present theory are $\sigma^{\max} = 0.41\sigma_0^{\max}$ and $\Delta\gamma_{\text{eff}} = 0.88\Delta\gamma_0$, whereas a curve $\sigma(g)$ averaged over those from 12 numerical realizations gives $\sigma^{\max} = 0.43\sigma_0^{\max}$ and $\Delta\gamma_{\text{eff}} = 0.89\Delta\gamma_0$ respectively.

As a further check, Figure 3.4 compares our predictions for the pull-off traction $\sigma^{\max}$ for the somewhat broader PSD defined by Figure 18 of [2] with numerical [GFMD] calculations and theoretical predictions both taken from Figures 15 and 17 of the same paper, for four different values of the interface energy $\Delta\gamma$ for plane surfaces. The agreement between the present theory and the GFMD calculations is clearly very satisfactory.

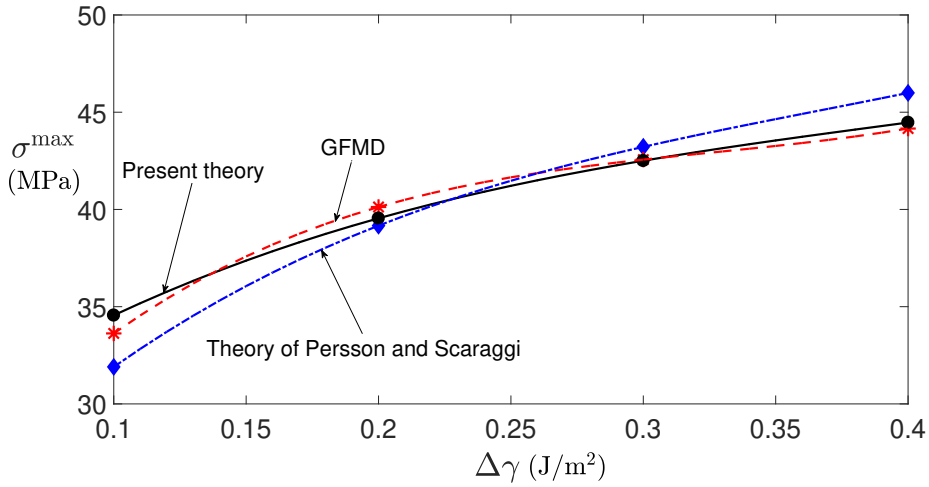

Figure 3.4: The solid line shows the predicted pull-off traction $\sigma^{\max}$ for the PSD defined by Figure 18 of [2], which has fractal form with $D = 2.2$ in the range $k_r < k < 8k_r$ and is constant in $k_r/4 < k < k_r$, where the roll-off wavenumber $k_r = 10^6$ m^{-1}. The RMS roughness height is $h_{\rm RMS} = 0.52$ nm. Theoretical predictions [dotted line] and numerical [GFMD] calculations [dashed line] from [2] are shown for comparison. [This figure is plotted with dimensional axes to facilitate comparison with [2].]

3.4 Results

The comparisons in Section Equation 3.3.1 show that the proposed solution gives good predictions of the effect of surface roughness on adhesive traction parameters, so we now apply the method to broader roughness spectra, for which direct numerical calculations would be very computationally intensive. In the interests of generality, we present the results in terms of the dimensionless wavenumber $\tilde{k}$ of Equation 3.13.

We restrict attention to power-law PSDs, which can be characterized by the lower and upper dimensionless wavenumbers $\tilde{k}_1$ and $\tilde{k}_2$, the fractal dimension D and the dimensionless height variance

$$\widetilde{m}_0 = \frac{m_0}{\epsilon^2} = \left(\frac{h_{\rm RMS}}{\epsilon}\right)^2 . \tag{3.14}$$

Figure 3.5 shows the effect of height variance on $\sigma^{\max}$ and $\Delta\gamma_{\rm eff}$, for a fractal PSD with $\tilde{k}_1 = 0.04, \tilde{k}_2 = 8$ and $D = 2.2$. In this range, $\widetilde{m}_0$ has a dramatic effect on both

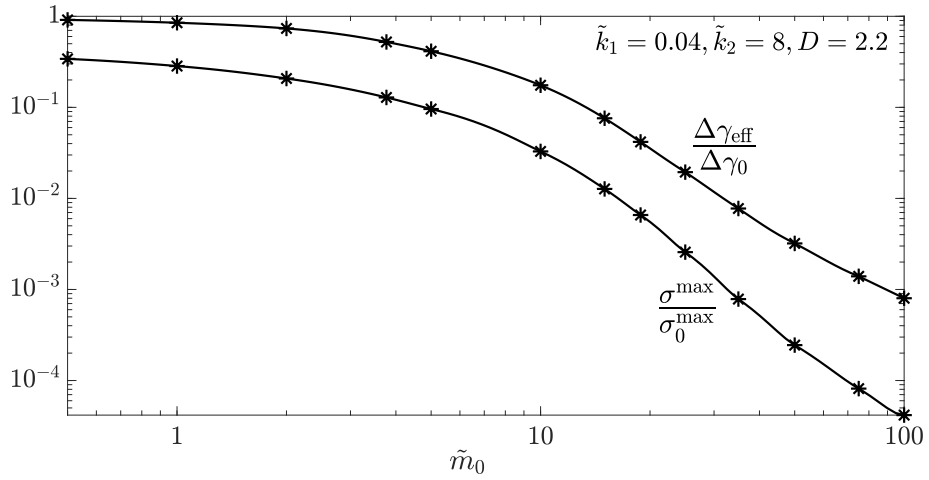

Figure 3.5: The effect of dimensionless height variance $\widetilde{m}_0$ on $\sigma^{\max}$ and $\Delta\gamma_{\text{eff}}$ for fractal roughness with $D = 2.2$ and $\tilde{k}_1 = 0.04, \tilde{k}_2 = 8$.

these measures of adhesion. Changing $\widetilde{m}_0$ by a factor of 200 [from 0.5 to 100 and hence h_{RMS} from 0.7ϵ to 10ϵ] reduces $\Delta\gamma_{\text{eff}}$ by a factor of 1,000 and $\sigma^{\max}$ by a factor of 25,000.

The dashed line in Figure 3.5 represents the analytical prediction for $\sigma^{\max}$ defined by [62] based on a 'Bearing Area' approximation to the adhesive tractions. This method underestimates $\sigma^{\max}$ [perhaps because of the empirical factor in the bearing area calculation], but tracks the shape of the curve well except at larger values of $\tilde{m}_0$.

We showed in [57] that the gap distribution $\Phi(g)$ and hence the effective traction law $\sigma(g)$ for a fractal surface converge as the upper cutoff $\tilde{k}_2 \to \infty$, since eventually the amplitudes of any added waves are small compared with the length scale of the intrinsic force between the surfaces. Results from the present analysis confirm that changing $\tilde{k}_2$ has relatively little effect on $\sigma^{\max}$ and $\Delta\gamma_{\text{eff}}$ once it approaches a practical limit of the atomic scale. By contrast, the lower cutoff $\tilde{k}_1$ has a significant effect, as shown in Figure 3.6, which plots these quantities as functions of $\tilde{k}_1$ for fixed values of $\widetilde{m}_0, \tilde{k}_2$ and D.

This result has a simple physical explanation. The amplitude of the traction distribution needed to flatten a single sine wave elastically is proportional to the

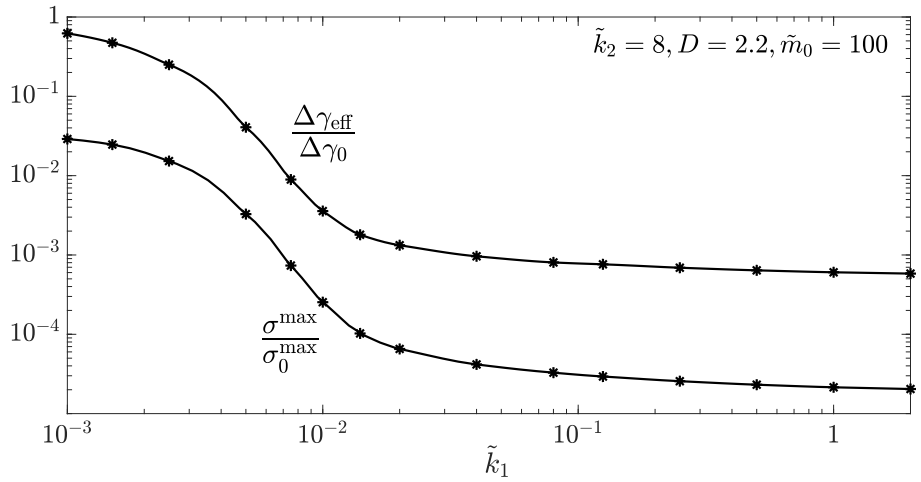

Figure 3.6: The effect of lower cutoff $\tilde{k}_1$ on $\sigma^{\max}$ and $\Delta\gamma_{\text{eff}}$ for fractal roughness with $\tilde{k}_2 = 8, \widetilde{m}_0 = 100$ and $D = 2.2$.

surface slope, so the short wavelength roughness is very difficult to deform. The behaviour in this range is dominated by the interfacial traction law and the height distribution, and is therefore well characterized by m_0. This is the range described by Persson and Scaraggi [2] as the 'DMT-limit'. However, at lower wavenumbers, elastic deformation becomes increasingly dominant, and the effect of coarse scale roughness tends to that predicted using a hard contact theory which is characterized by the mean square slope m_2.

3.4.1 Effect of fractal dimension

All the results presented above are for a surface PSD with fractal dimension $D = 2.2$. Reducing D for given values of the other parameters has the effect of moving contributions from the variance $\widetilde{m}_0$ towards lower wavenumbers, where we have already seen the effect of roughness on both $\sigma^{\max}$ and $\Delta\gamma_{\text{eff}}$ is somewhat reduced. This tendency is confirmed by Figure 3.7, for $\tilde{k}_1 = 0.05, \tilde{k}_1 = 8, \widetilde{m}_0 = 0.4356$. However, the effect is relatively modest, implying that the results for $D = 2.2$ should be reasonably representative for other practical fractal dimensions.

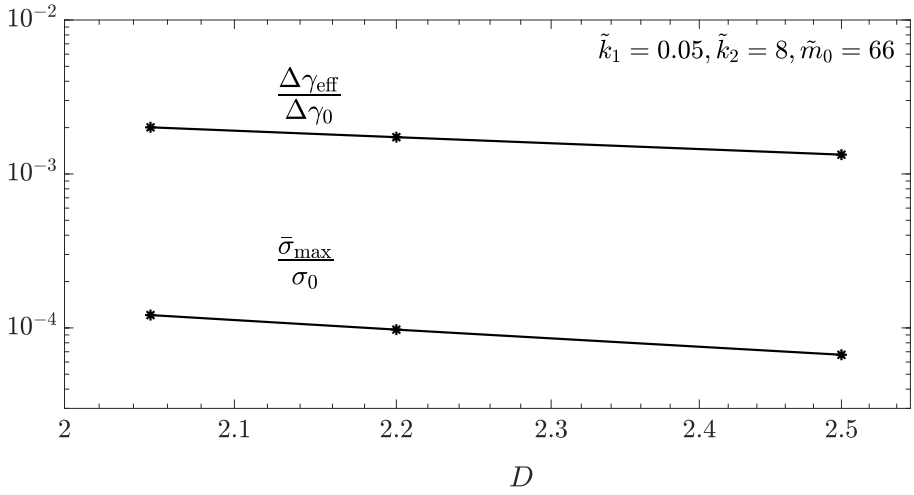

Figure 3.7: The effect of fractal dimension D on $\sigma^{\max}$ and $\Delta\gamma_{\text{eff}}$ for fractal roughness with $\tilde{k}_1 = 0.05, \tilde{k}_2 = 8$ and $\widetilde{m}_0 = 66$.

3.4.2 Contour plot

Each point in Figures 3.5 and 3.6 involves the calculation of the effective traction law $\sigma_i(g)$ for the PSD truncated at at a progressively lower wavenumber cutoff k_i and therefore provides implicit information about the pull-off traction $\sigma^{\max}$ and the effective interface energy $\Delta\gamma_{\text{eff}}$ at a series of points along a line in (m_0, k_1)-space. These data were used to construct the contour plots of Figure 3.8 [for $\sigma^{\max}$] and Figure 3.9 [for$\Delta\gamma_{\text{eff}}$] for power-law PSDs with $\tilde{k}_2 = 8$ and $D = 2.2$.

The bottom left region of each of these figures [below the dashed line] defines parameter values in which the reduction of maximum negative slope in the effective traction law $\bar{\sigma}(\bar{g})$ due to surface roughness is insufficient to prevent instability. In this range, if the linear dimensions of the surface are sufficiently large to support a sine wave of the given value of $\tilde{k}_1$, we can anticipate periodic structures of the type documented by Chaudhury and Shenoy [58, 59, 60, 61], even if the roughness PSD contains no waves of this wavelength.

One consequence of these instabilities is that there then exist two stable equilibrium states for a given value of mean separation, so that the loading and unloading

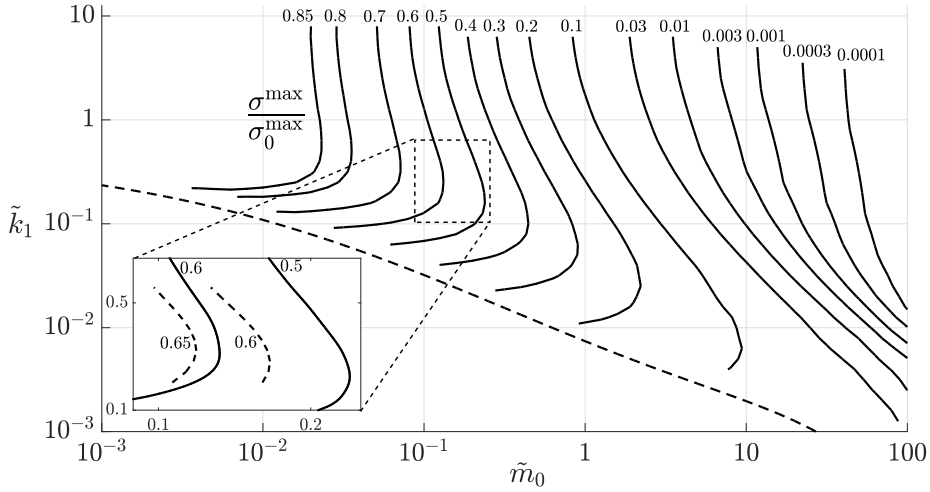

Figure 3.8: Contour plot of normalized pull-off traction $\sigma^{\max}/\sigma_0^{\max}$ as a function of $\tilde{k}_1, \widetilde{m}_0$ for fractal roughness with $\tilde{k}_2 = 8$ and $D = 2.2$. The inset compares contours in the dashed rectangle from the present theory [solid lines] with those from the GFMD code [dashed lines] using a single realization for each point.

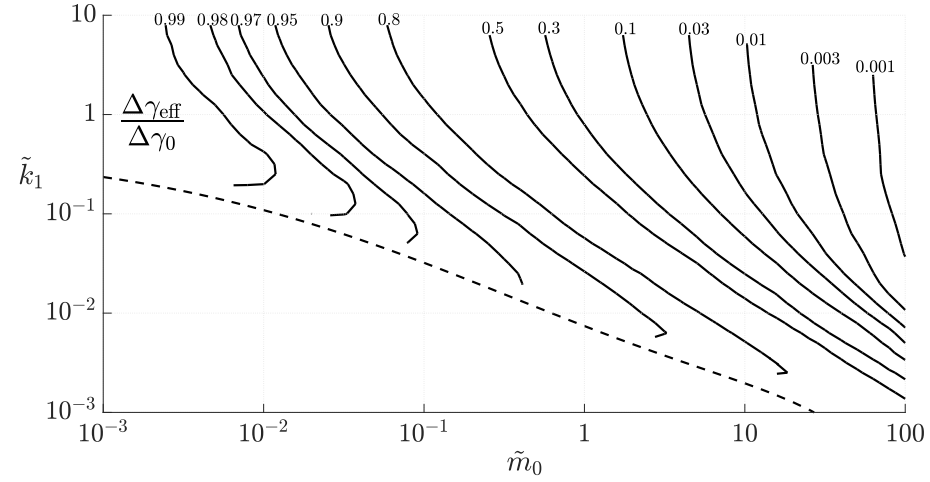

Figure 3.9: Contour plot of normalized effective interface energy $\Delta\gamma_{\text{eff}}/\Delta\gamma_0$ as a function of $\tilde{k}_1, \widetilde{m}_0$ for fractal roughness with $\tilde{k}_2 = 8$ and $D = 2.2$.

curves will generally be different. This implies hysteretic energy loss during a loading/unloading cycle, and since different regions encounter the instability at different points in the loading cycle, the unloading cycle and the hysteretic loss will depend on the maximum compressive traction during loading. Results of this kind have been documented in asperity models ([63]) and in numerical models ([64]). One method of quantifying these effects would be to use a partition of the PSD as shown schematically in Figure 3.2, such that inclusion of the fine scale alone defines a point in the stable range in Figs. 8, and 9 and hence leads to a single-valued traction law. This law could then be used in a numerical solution of the coarse-scale problem. This is a subject of ongoing research.

The contours in these figures start to curve backwards as the unstable region is approached, particularly for the pull-off traction $\sigma^{\max}$ in Figure 3.8. This implies a greater reduction of adhesion in this region as k_1 is reduced. Physically this arises because long wavelength sinusoids experience relatively large amplitudes of elastic deformation, which increase the variance of the local gap g in regions where the traction law has a negative slope. In effect, the PDF $\Phi(g)$ is already starting to develop the bimodal form associated with the unstable patterns described in [58, 59, 60, 61].

To ensure that these results were not the result of a fictitious numerical instability, we ran numerical [GFMD] examples in the range defined by the dotted rectangle in Figure 3.8. In this range, numerical calculations are computer-intensive but not prohibitively so. Since each run of the GFMD code defines only one realization of the underlying statistics, a precise check on the theory is not possible, but the predicted pull-off traction for all the cases analyzed were within $\pm 10\%$ of the predicted values. More importantly, the GFMD results confirm that the pull-off traction falls with decreasing k_1 near the stability boundary, implying that the contours have the shape shown in Figure 3.8.

3.5 Conclusions

This chapter presents an efficient procedure for predicting the effect of broad sprectrum surface roughness on the effective adhesive traction law — i.e. the relation between nominal adhesive traction and mean gap. Results agree well with the averages of direct numerical simulations for the relatively narrower spectra over which such simulations are computationally practicable.

Contour plots are presented for the nominal pull-off traction and effective interface energy for broader power-law spectra as a function of lower cutoff wavenumber and height variance. The calculations show that instabilities occur for relatively smooth surfaces whose linear dimensions are sufficiently large to support long wavelength perturbations. This is a physical effect that has been documented both experimentally and theoretically. Near the unstable range, a greater reduction in adhesive effects is predicted and this behaviour has been confirmed for relatively narrow spectra using numerical simulations.

At large wavenumbers [short wavelengths], the effect of roughness on adhesion is well-characterized by the height variance m_0, but at lower wavenumbers elastic effects become more important and incremental contributions to m_0 have less effect, except near the unstable range.

CHAPTER IV

Effect of Adhesion on the Thin Elastic Layer

4.1 Thin elastic layers

Many engineering and scientific applications involve thin deformable layers supported by a relatively rigid foundation. Examples include rubber layers bonded to steel components and cartilage layers attached to bones. If an elastic layer of thickness h is bonded to a rigid foundation and then subjected to a uniform tensile traction σ, the only non-zero strain will be that in the thickness direction and the surface will move outwards through a distance

$$u = \frac{\sigma}{k} \quad \text{where} \quad k = \frac{E(1-\nu)}{(1+\nu)(1-2\nu)h} \, . \tag{4.1}$$

Johnson [65] argued that this remains a good approximation under more general spatially-varying tractions as long as the layer is 'sufficiently thin' meaning that h is small compared with the linear dimensions of the loaded area. The layer then acts like a Winkler foundation of 'modulus' k, with proportionality between local

Chapter 4 is adapted from part of the published paper:
Ciavarella, M., Joe, J., Papangelo, A., Barber, J. R. "The role of adhesion in contact mechanics." *Journal of the Royal Society Interface* 16.151 (2019): 20180738.

displacement and local traction. In particular, in non-conformal contact problems [such as indentation of an elastic layer by a sphere], the contact pressure then goes to zero at the edge of the contact area.

Johnson's argument was extended to problems involving adhesive tractions by Yang [66] and Argatov *et al.* [67], using an energy argument analogous to that in the JKR theory [10]. They showed that the effect of interface energy was to change the boundary condition at the edge of the contact area from $\sigma = 0$ to $\sigma = \sqrt{2k\Delta\gamma}$, which is independent of the contact geometry [as is the stress intensity factor Equation 4.2 in the JKR theory].

$$K_{\mathrm{I}} = \sqrt{2E^*\Delta\gamma} \quad \text{where} \quad \frac{1}{E^*} = \frac{1-\nu_1^2}{E_1} + \frac{1-\nu_2^2}{E_2} \tag{4.2}$$

and E_i, ν_i are Young's modulus and Poisson's ratio respectively for the two bodies, with $i = 1, 2$.

If $\nu \to 0.5$, the modulus $k \to \infty$, since the layer becomes incompressible. Deformation is still possible under non-uniform tractions, but involves the displacement of material in the plane of the layer [65]. Approximate solutions for the case with adhesive tractions are given by Yang [68], Argatov *et al.* [67] and Papangelo [69].

4.1.1 Instabilities

The traction law $\sigma(g)$ of Equation 1.1 and Figure 1.1 can be regarded as a non-linear spring [with ranges of negative stiffness] in series with the linear spring associated with the modulus k of Equation 4.1. For example, if Δ denotes the gap that would exist between a layer and a plane surface in the absence of elastic deformation, the actual gap will be g where

$$\Delta = g + \frac{\sigma(g)}{k} \quad \text{and hence} \quad \frac{\partial\Delta}{\partial g} = 1 + \frac{1}{k}\frac{\partial\sigma}{\partial g}\,. \tag{4.3}$$

The gap g and hence the traction $\sigma(g)$ will be multivalued functions of rigid-body approach Δ if there exist ranges where $\partial\Delta/\partial g < 0$. Notice [for example from Figure 1.1] that any traction law involving adhesive tractions must exhibit a range of values of g in which the slope $\partial\sigma/\partial g < 0$, and from Equation 4.3, instability is most likely to occur at the point where the magnitude of this negative slope is maximum. For the traction law of Equation 1.1, this maximum slope occurs at $g = (15/2)^{1/6}\varepsilon$ and is of magnitude $1.253\Delta\gamma/\varepsilon^2$.

A typical case involving instability is illustrated in Figure 4.1, where $\nu = 0.25$ and the dimensionless parameter

$$\beta = \frac{E\varepsilon^2}{h\Delta\gamma} \tag{4.4}$$

is equal to 0.5. If the bodies are initially widely separated, the tractions will be defined by the lower branch of the curve, but if Δ is reduced below Δ_A, there must then be a jump to the point B. A jump in the opposite direction from C to D is anticipated during subsequent separation, so that during an approach-separation cycle, there will be a hysteretic energy loss defined by the area $ABCD$.

4.1.2 Sinusoidal instabilities

The uniform state defined by Equation 4.3 can be unstable to non-uniform perturbations even where jumps are not predicted. It is convenient to define a dimensionless coordinate $\xi = x/h$ in the plane of the layer. For a linear elastic layer, a sinusoidal traction distribution $\sigma(\xi) = S\cos(\zeta\xi)$ will produce a surface displacement

$$u(\xi) = \frac{S}{k(\zeta)}\cos(\zeta\xi)\ , \tag{4.5}$$

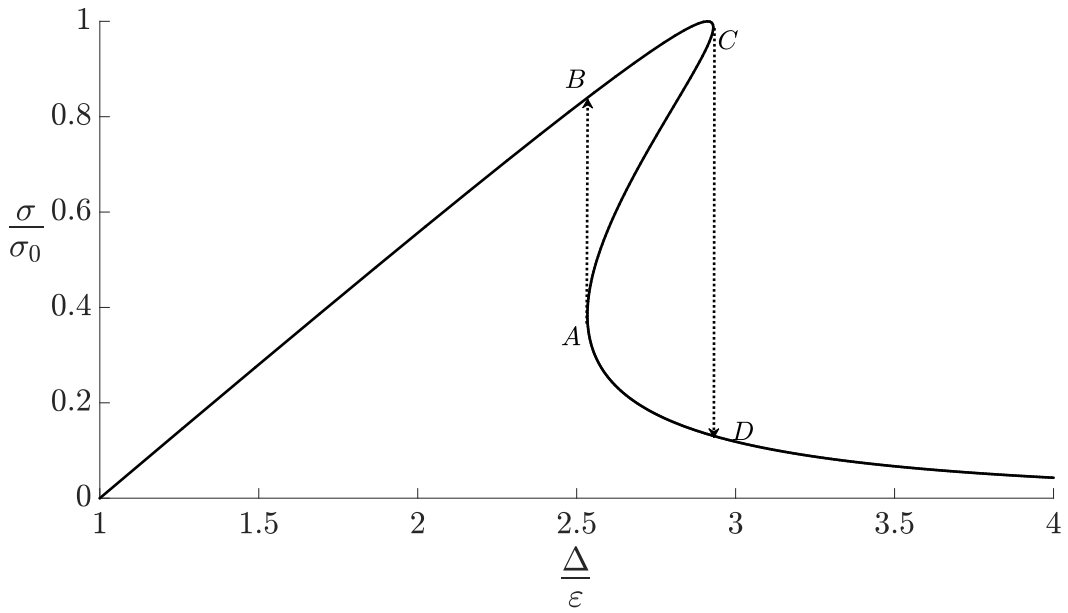

Figure 4.1: Adhesive traction σ as a function of rigid-body approach Δ [i.e. the gap that would exist in the absence of elastic deformation] for a layer with $\nu = 0.25$ and $\beta = 0.5$. Jumps occur during approach from A to B and during separation from C to D as indicated by the dotted lines.

where $k(\zeta)$ is a wavenumber-dependent stiffness. For a uniform elastic layer bonded to a rigid foundation, we have

$$k(\zeta) = \frac{E\zeta\left[(3-4\nu)\cosh(2\zeta) + 2\zeta^2 + 5 - 12\nu + 8\nu^2\right]}{2h(1-\nu^2)\left[(3-4\nu)\sinh(2\zeta) - 2\zeta\right]} \tag{4.6}$$

[70], which reduces to Equation 4.1 in the limit $\zeta \to 0$. However, similar arguments can also be applied to more complex elastic systems such as multilayers or functionally graded layers, the only change being in the function $k(\zeta)$.

If the layer is placed such that the uniform solution of § 4.1.1 involves a gap g_1, energetic arguments can be used to show that infinitesimal sinusoidal perturbations on this solution of wavenumber ζ will then be unstable if

$$\left(\frac{\partial\sigma}{\partial g}\right)_{g=g_1} < -k(\zeta)\,, \tag{4.7}$$

[71, 72], so instability is most likely to occur at values of g_1 near the maximum negative slope of the traction law. With the Lennard-Jones law, this implies that instabilities are to be anticipated during the approach of an elastic layer to a plane surface unless

$$k(\zeta) > \frac{1.253\Delta\gamma}{\varepsilon^2} \quad \text{or equivalently} \quad \frac{E}{hk(\zeta)} < \frac{\beta}{1.253} \tag{4.8}$$

for all ζ, from Equation 4.4, and Equation 4.7.

Non-linearity of the traction law Equation 4.1 places limits on the growth of such a perturbation, but if the condition Equation 4.7 is satisfied for some range of values of g_1, ζ, we might then anticipate the development of a spatially-periodic deformation pattern during approach of the layer to a plane surface.

Patterns of this kind have been predicted theoretically [71, 72] and observed experimentally [73, 74] mainly for incompressible layers for which the 'uniform' instability of § 4.1.1 is suppressed. Gonuguntla *et al.* [73] have shown how this self-patterning behaviour can be used in the manufacture of patterned layers using lithography.

4.1.3 Periodic deformation patterns

Figure 4.3 shows contours of the gap $g(x, y)$ for four stages of approach Δ for a layer with $\beta = 0.25, \nu = 0.5$. These results were obtained using the Green's Function Molecular Dynamics [GFMD] algorithm of Persson and Scaraggi [75]. Since the material is incompressible, uniform instabilities of the type discussed in Section 3.1 cannot occur. The contours are defined as multiples of ε and the scale bar in Figure 4.3 (a) represents the layer thickness h.

During approach [Δ decreasing] the morphology is first defined by pillars of 'contact' [values of g close to ε] surrounded by regions of much larger gap (a). Further reduction in Δ leads to the labyrinth pattern (b) and then an inverted labyrinth (c)

where regions of contact are connected. The last stage (d) comprises a pattern of approximately circular separation regions surrounded by contact. The red line in Figure 4.3 (d) represents wavelength corresponding to the most unstable sinusoidal perturbation [see § 4.1.5 and Figure 4.5 below].

Theoretically, instability starts at the value of Δ at which an infinitesimal sinusoidal perturbation first becomes unstable. However, once a pattern is established, it persists beyond the range of linear instability and hence the traction curves for loading and unloading are different, as shown in Figure 4.3. During progress from contact to separation, patterns develop before the theoretical point, presumably due to the use of finite increments in the iterative algorithm.

4.1.4 Determination of patterns using series methods

An alternative approach for approximating these patterns is to represent the elastic deformation as a finite Fourier series and use the Rayleigh-Ritz method for determining the coefficients. For example, in two dimensions we write

$$u(\xi) = \sum_{n=0}^{N} u_n \cos(n\zeta_0 \xi) \ , \tag{4.9}$$

where ζ_0 is a fundamental wavenumber that might be related to the finite dimension of the contact surface. The elastic strain energy per unit area is then

$$U = \frac{1}{2} k(0) u_0^2 + \frac{1}{4} \sum_{n=1}^{N} k(n\zeta_0) u_n^2 \ . \tag{4.10}$$

and the interface energy per unit area is defined by

$$\Gamma = \frac{\zeta_0}{2\pi} \int_0^{2\pi/\zeta_0} d\xi \int_{\Delta - u(\xi)}^{\infty} \sigma(g) dg \ . \tag{4.11}$$

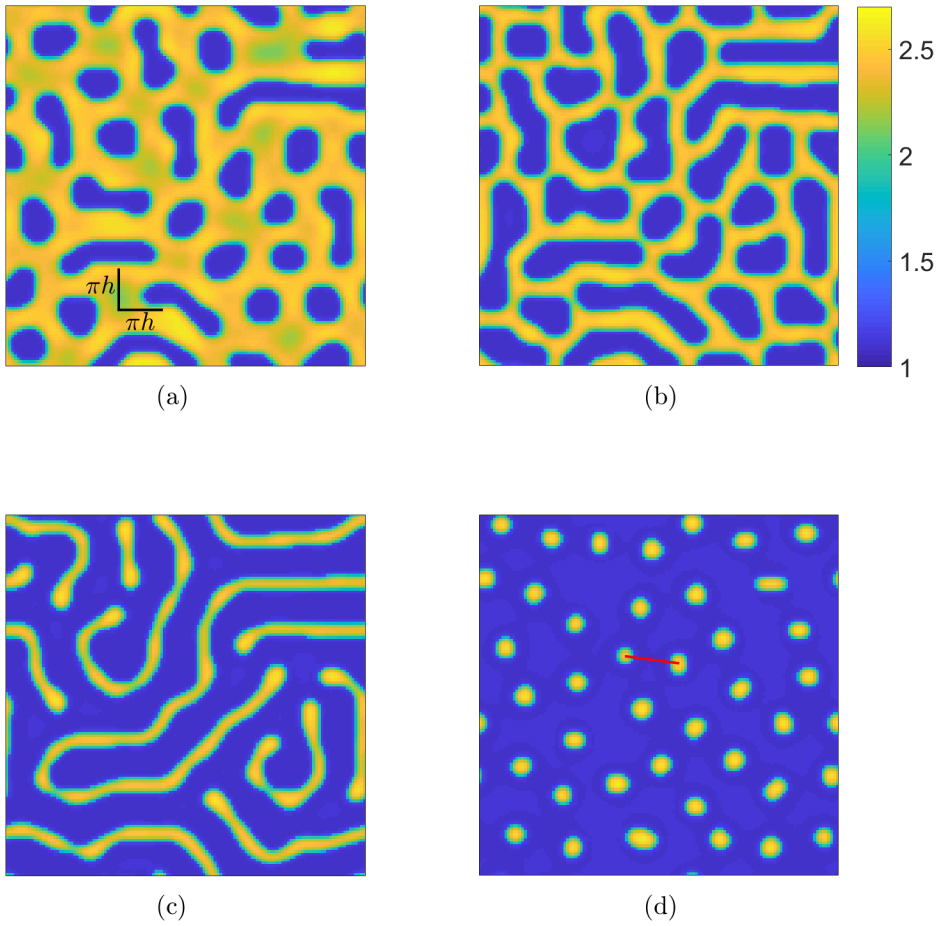

Figure 4.2: Contours of dimensionless local gap $g(x, y)/\varepsilon$ during approach of a uniform incompressible layer to a plane surface. $\Delta = 2\varepsilon$ (a), 1.7ε (b), 1.4ε (c), 1.2ε (d). The contour scale applies to all four figures.

The coefficients u_n are then determined using an appropriate optimization algorithm so as to minimize the total energy $\Pi = U - \Gamma$ for a given value of approach Δ [72]. The same technique was extended to three-dimensional patterns by Gonuguntla *et al.* [73] using a double Fourier series.

4.1.5 Effect of material parameters

Figure 4.5 shows the dimensionless layer compliance [reciprocal of stiffness] $E/hk(\zeta)$ as a function of wavenumber ζ for the bonded layer defined by Equation 4.7 for various

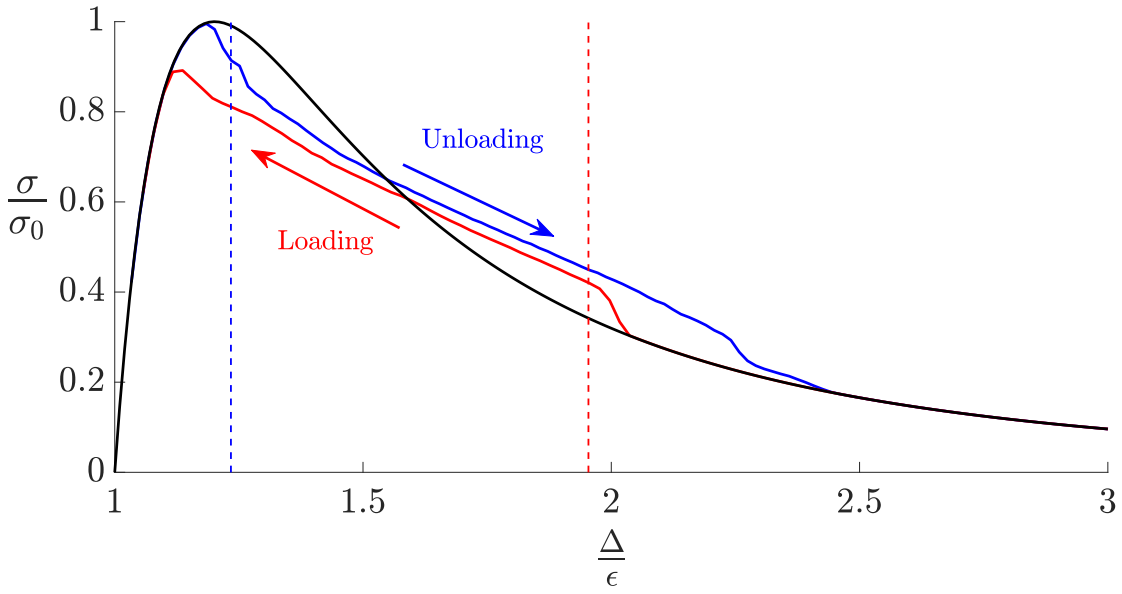

Figure 4.3: Relation between mean traction and rigid-body separation Δ for $\beta = 0.25, \nu = 0.5$. The black line represents the uniform traction solution of Equation 1.1. It is unstable between the vertical dashed lines.

values of Poisson's ratio ν.

We notice from Figure 4.5 that the curves for $\nu > 0.25$ exhibit a maximum at some value $\zeta = \zeta_0 > 0$, whereas for $\nu \leq 0.25$, the maximum occurs at $\zeta = 0$. In both cases, instability will commence when the gap $g = g_1$ in the uniform solution reaches the value at which $\partial\sigma/\partial g$ first satisfies Equation 4.7. For $\nu \leq 0.25$ the first unstable condition corresponds to a uniform perturbation [$\zeta = 0$] and hence occurs at the point A during loading and C during unloading in Figure 4.1. The unstable response comprises a sudden change [jump] in uniform traction as indicated.

For $\nu > 0.25$, the maximum compliance occurs at a non-zero wavenumber ζ_0 and we anticipate the development of a pattern with this periodicity, at least near the value of g at which Equation 4.7 is first satisfied. This behaviour is shown schematically in Figure 4.5 for the Lennard-Jones traction law.

The dashed line in this figure defines the value of β below which a uniform pertur-

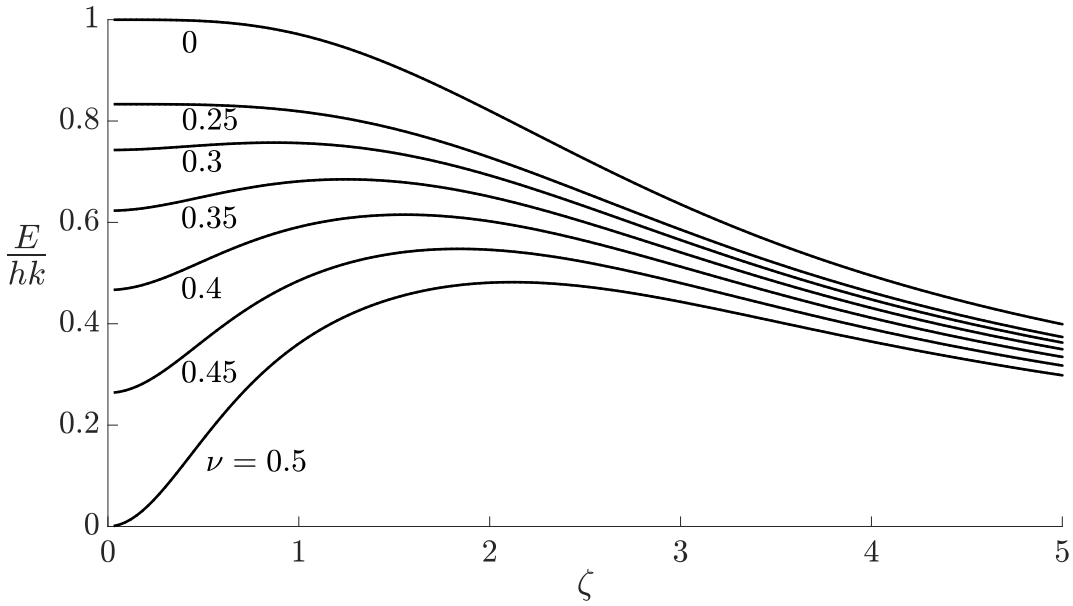

Figure 4.4: Dimensionless layer compliance as a function of wavenumber for an elastic layer bonded to a rigid foundation. We recall from condition Equation 4.8 that instability occurs above the value $\beta/1.253$, and hence for $\nu = 0.5$, low and high wavenumbers are both stable.

bation [$\zeta = 0$] is also unstable. In this region, the non-uniform instability is triggered before the uniform one and generally dominates the subsequent behaviour. However, this requires that a representative in-plane dimension L of the layer be large enough to accommodate at least one wavelength of an unstable sinusoidal perturbation. In most practical cases $h \ll L$ and which ensures that this condition is satisfied except for values of ν quite close to 0.5.

Similar calculations can be performed for more complex layers. In particular, we note that for a bi-material layer, the dimensionless compliance may exhibit two distinct maxima [76]. In such cases, the absolute maximum of the curve defines the first instability during either approach or separation and generally dominates the subsequent pattern development.

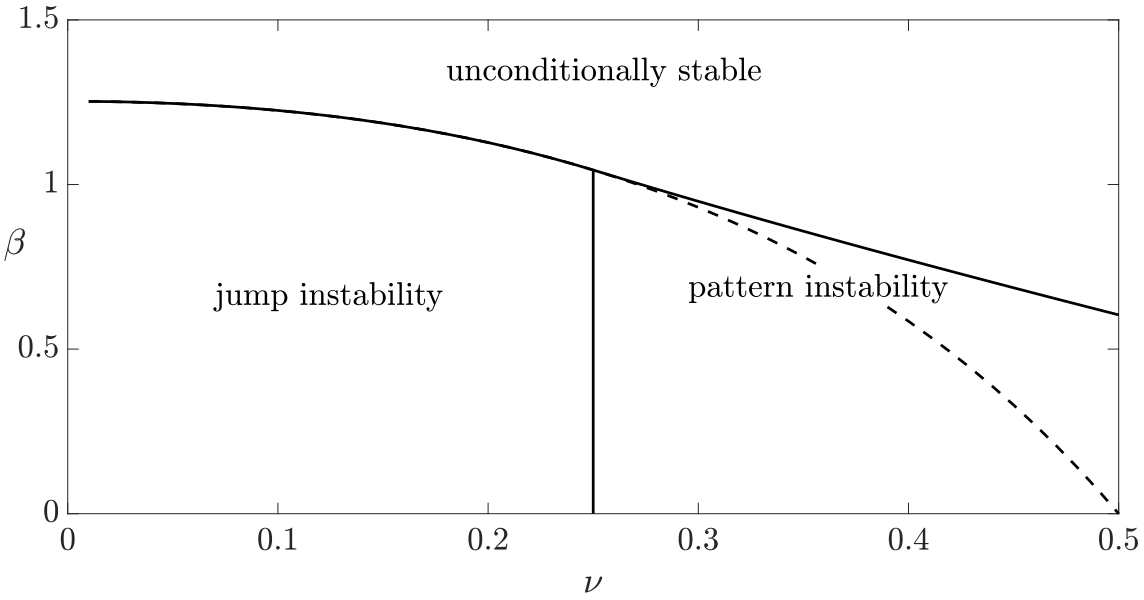

Figure 4.5: Dependence of stability behaviour on ν and β.

4.2 Conclusions

We have seen that the development of self-generated patterns can result from the interaction of adhesive [i.e. tensile] tractions between contacting bodies for $\nu > 0.25$. The pattern shapes can be pillars, labyrinth, or column, depending on the approach. Once instability occurs during loading or unloading, the morphology changes slowly from the first instability point, resulting in different loading and unloading curves.

CHAPTER V

Effect of Surface Roughness on Adhesive Instabilities for the Elastic Layer

5.1 Introduction

If two bodies with plane surfaces are placed close together, they may experience attractive [e.g. van der Waals'] forces, or forces involving both attractive and repulsive ranges [4, 5]. Since the attractive forces must eventually decay with increasing separation, they have the character of a 'negative spring', which can trigger an elastic instability. If the bodies are incompressible [Poisson's ratio $\nu = 0.5$], or if a body comprising a thin elastic layer bonded to a rigid plane surface is attracted to another rigid plane surface, the instability may result in a non-uniform [typically periodic] pattern of alternating regions of contact and separation. Patterns of this kind have been observed experimentally [73, 74], and predicted theoretically, based on energetic arguments [71, 72]. In particular, the characteristic length scale of the pattern correlates with the unstable wavelength in a linear perturbation of the uniform state. The patterning instability also modifies the mean traction-separation characteristic

Chapter 5 is reproduced from the publication:
Joe, Junki, James Richard Barber, and Michael D. Thouless. "Effect of surface roughness on adhesive instabilities for the elastic layer." *Frontiers in Mechanical Engineering* 6 (2020): 31.

for the layered system, generally leading to different behaviour during approach and separation and consequent hysteresis losses [77].

The instability permits self-assembly processes such as elastic contact lithography [ECL], where the pattern in a polymer film is fixed by UV curing or by lowering the temperature [78, 79, 80]. In ECL, the periodicity and size of the pattern are critical parameters and various methods have been proposed to control them, including the use of a curved substrate [81], an imprinted stamp [82, 83, 84, 85, 86], or a pre-strained substrate [87]. Also, electric fields can be used to extend the range of attraction relative to van der Waals' forces and to provide greater control of the process, whilst retaining a similar morphology [88, 89, 90].

Real surfaces are of course never perfectly smooth, and surface roughness generally reduces both the maximum pull-off traction and the maximum negative slope of the effective traction-separation law [3]. This should reduce the tendency for patterning in the contact of layered bodies. However, sufficiently small amplitude roughness might also serve as an initial perturbation to trigger an instability. In this chapter, we shall therefore use a numerical solution to examine the effect of roughness on both the generation of patterns and the mean traction-separation relation. In particular, we shall examine the extent to which the effect of roughness can be captured by using a modified adhesive traction law developed for the contact of rough elastic half spaces.

5.2 Deformation of a thin layer

We consider an elastic layer of thickness h bonded to a rigid plane, and define Cartesian coordinates (x, y) in the plane of the layer surface and corresponding dimensionless coordinates $\xi = x/h, \eta = y/h$. If a second rigid plane is placed a distance $\bar{g}$ away from the undeformed surface of the layer as shown in Figure 5.1, the local gap

between the surfaces will then be

$$g(\xi, \eta) = \bar{g} - u(\xi, \eta) \ , \tag{5.1}$$

where $u(\xi, \eta)$ is the local outward normal elastic displacement of the layer surface.

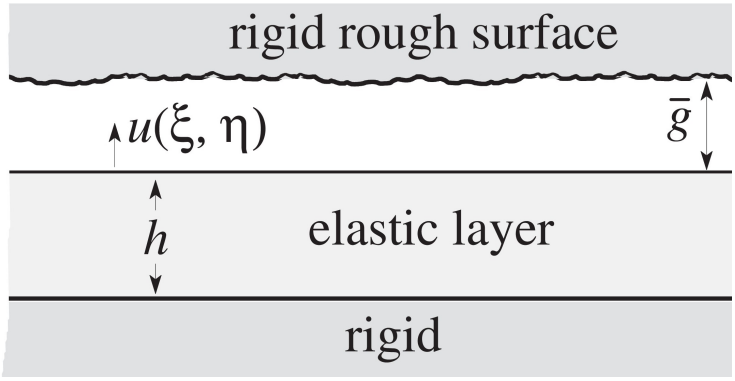

Figure 5.1: A rigid body with a plane surface that may contain some surface roughness is placed near to an elastic layer bonded to a rigid foundation. The mean gap is $\bar{g}$ and $u(\xi, \eta)$ is the local elastic displacement of the layer surface.

5.2.1 Interface energy

We assume that the adhesive tractions between the surfaces can be described by a traction law $\sigma(g)$, where g is the local value of the gap. We can then also define the mean interface energy per unit area as

$$\Gamma = \big\langle \gamma(g(\xi, \eta)) \big\rangle \quad \text{where} \quad \gamma(g) = -\int_{g}^{\infty} \sigma(s) ds \ , \tag{5.2}$$

and a stable final configuration will be one that minimizes the total potential energy $\Pi = U + \Gamma$, where U is the mean elastic strain energy per unit area.

5.2.2 Elastic strain energy

The normal traction $\sigma(\xi, \eta)$ at the free surface of the layer needed to produce a sinusoidal normal elastic displacement $u(\xi, \eta) = u_\zeta \cos(\zeta\xi)$ is

$$\sigma(\xi, \eta) = \frac{Ef(\zeta)u_\zeta}{h} \cos(\zeta\xi) \,, \tag{5.3}$$

where

$$f(\zeta) = \frac{\zeta\left[(3-4\nu)\cosh(2\zeta) + 2\zeta^2 + 5 - 12\nu + 8\nu^2\right]}{2(1-\nu^2)\left[(3-4\nu)\sinh(2\zeta) - 2\zeta\right]} \,, \tag{5.4}$$

[70], and we recall that $\xi = x/h$, so ζ is a dimensionless wavenumber.

In this chapter, we shall restrict attention to incompressible layers [$\nu = 0.5$], for which the corresponding dimensionless compliance $1/f(\zeta)$ is shown as a function of dimensionless wavenumber ζ in Figure 5.1. The curve exhibits a maximum of approximately 0.482 at a wavenumber $\zeta \approx 2.1$, and zero compliance for uniform loading [$f(\zeta) \to \infty$ as $\zeta \to 0$]. One consequence of this is that with general loading $\sigma(\xi, \eta)$, the mean value of u is zero and hence $\bar{g}$ is determined by the rigid-body approach which is a controlled parameter.

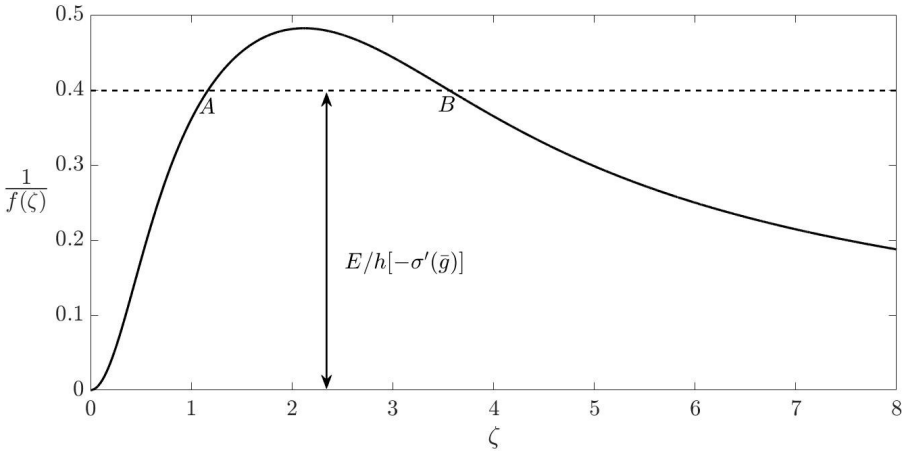

Figure 5.2: Dimensionless layer compliance as a function of wavenumber for an incompressible elastic layer bonded to a rigid foundation. For a given value of $E/h[-\sigma'(\bar{g})]$ satisfying condition Equation 5.6, wavenumbers in the range $\zeta_A < \zeta < \zeta_B$ are unstable.

The mean elastic strain energy per unit area associated with the deformation Equation 5.3 is

$$U(\zeta) = \frac{1}{2} \langle \sigma(\xi, \eta) u_\zeta(\xi, \eta) \rangle = \frac{E f(\zeta) u_\zeta^2}{4h} \ . \tag{5.5}$$

The elastic strain energy for more general displacement distributions can be obtained by writing $u(\xi, \eta)$ as a double Fourier series or Fourier transform and convoluting the resulting transform with Equation 5.5.

5.2.3 Stability criterion

If both surfaces are plane [i.e. smooth], the state $u(\xi, \eta) = 0, g(\xi, \eta) = \bar{g}, \sigma(\xi, \eta) = \sigma(\bar{g})$ is clearly an equilibrium state, but it will be unstable to small sinusoidal perturbations of dimensionless wavenumber ζ if there exists any ζ such that

$$-\left(\frac{\partial \sigma}{\partial g}\right)_{g=\bar{g}} > \frac{E f(\zeta)}{h} \ . \tag{5.6}$$

The critical wavenumber is defined by the maximum of the curve in Figure 5.1, from which we deduce that the uniform solution will be unstable if and only if $-\sigma'(\bar{g}) > E/0.482h$.

5.2.4 Solution method

More general displacement distributions for a square domain $0 < x < L$, $0 < y < L$ can be written in the form

$$u(x, y) = \Re \sum_{m=-N}^{N} \sum_{n=-N}^{N} A_{mn} \exp\left[\frac{2\pi \imath (mx + ny)}{L}\right] \ , \tag{5.7}$$

and Equation 5.5 can then be used to obtain the mean strain energy per unit area U as

$$U = \sum_{m=-N}^{N} \sum_{n=-N}^{N} \frac{E \left|A_{mn}\right|^2 f(\zeta_{mn})}{4h} \tag{5.8}$$

where

$$\zeta_{mn} = \frac{2\pi h\sqrt{m^2+n^2}}{L} \ . \tag{5.9}$$

Adding the corresponding interface energy from Equation 5.2, we obtain the total potential energy Π, which must be a minimum at a stable equilibrium state. We used the gradient descent method to identify the values of the Fourier coefficients A_{mn} for a local energy minimum. Notice that the upper limit N must be chosen so as to provide an adequate number of integration points in the evaluation of Γ.

5.3 Results for smooth surfaces

If the two surfaces are smooth, the uniform state is always an equilibrium solution at which energy gradients are zero, and since the material is incompressible [$\nu = 0.5$], this corresponds to $u(\xi, \eta) = 0$. Even when the criterion Equation 5.6 is satisfied, the numerical solution may remain at the uniform state unless some small perturbation is introduced.

We used the traction law

$$\sigma(g) = \frac{8\Delta\gamma}{3\varepsilon}\left[\left(\frac{\varepsilon}{g}\right)^3 - \left(\frac{\varepsilon}{g}\right)^9\right] \tag{5.10}$$

[5] derived from Lennard-Jones molecular force law [4], where ε is an interatomic length scale and $\Delta\gamma = \gamma(\varepsilon)$ is the interface energy per unit volume at the equilibrium spacing $g = \varepsilon$. The maximum tensile traction occurs at $g = 3^{1/6}\varepsilon$ and is of magnitude $\sigma_0 \approx 1.06\Delta\gamma\varepsilon$.

If the maximum negative slope $[-\sigma'(g)]_{\max}$ satisfies the condition

$$\frac{h}{E}\left[-\sigma'(g)\right]_{\max} > \frac{1}{0.482} \ , \tag{5.11}$$

there will exist a bounded range $g_1 < \bar{g} < g_2$ in which the uniform solution is unstable.

Also, for a value of $\bar{g}$ strictly within this range, there will exist a range of unstable wavenumbers $\zeta_A < \zeta < \zeta_B$, including but not limited to $\zeta \approx 2.1$. This range can be identified by drawing a horizontal line at the height $E/h[-\sigma'(\bar{g})]$ in Figure 5.2 as shown, and finding its intersection with the curve.

We start the solution procedure with a value of $\bar{g}$ outside the unstable range and then change $\bar{g}$ by small increments, using the solution at the previous step as an initial guess for the gradient descent solution. This is expected to mimic the behaviour of the physical system under controlled displacement conditions. Numerical noise might also be expected to emulate the effect of noise [e.g. vibration] in an experimental system.

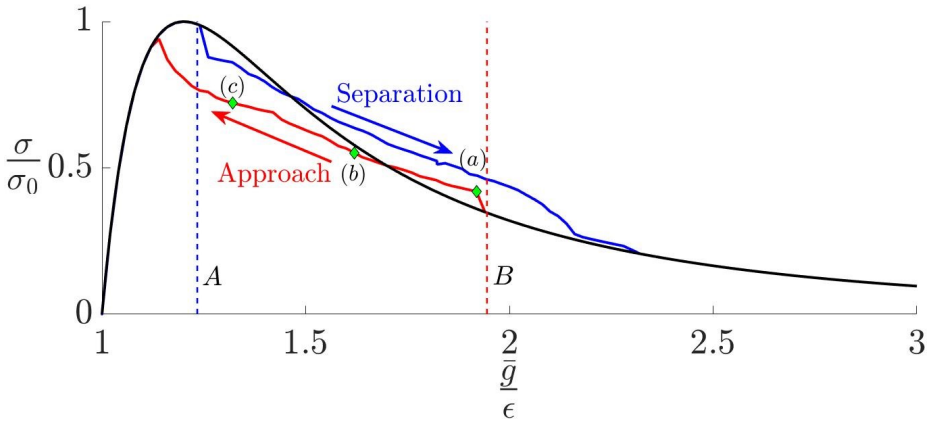

Figure 5.3: Mean traction $\bar{\sigma}$ as a function of mean gap $\bar{g}$ for a smooth layer for $\beta = 0.5$ and domain size $L = 8\pi h$, showing instabilities during approach and separation. The Lennard-Jones law Equation 5.10 is shown in black. The dashed lines A, B define the region in which the uniform traction solution is unstable.

Figure 5.3 compares a typical relation between the mean traction $\bar{\sigma} = \langle \sigma(x, y) \rangle$ and the mean gap [approach] $\bar{g}$ with the local traction law Equation 5.10 for the case where the dimensionless parameter

$$\beta = \frac{E\varepsilon^2}{h\Delta\gamma} \tag{5.12}$$

is equal to 0.25. The domain size was chosen so as to define a fundamental wavenumber [e.g. ζ_{01}] equal to 0.25, so that $L = 8\pi h$. Results are shown for both separation $d\bar{g}/dt > 0$ and approach $d\bar{g}/dt < 0$. In each case, the uniform state is preserved up to the appropriate stability boundary [denoted by A and B respectively], but the non-uniform solution then persists significantly beyond the point at which the uniform solution reverts to stability. We deduce that even in the stable range there exist local energy minima corresponding to non-uniform states, and that these states are separated from the lower energy uniform state by energy barriers.

Notice that both the approach and separation curves in Figure 5.3 are approximately straight lines with slope close to the critical slope defined by Equation 5.6.

The non-uniform deformation states are characterized by the development of regular patterns. Figure 5.4(a,b,c) shows contours of local gap $g(x, y)$ corresponding to the points on the approach curve labelled (a), (b) and (c) in Figure 5.3. A 'labyrinth' [i.e. a connected system of passageways (high g) separated by walls of 'contact' (low g)] develops at the onset of instability (a) and then morphs into an inverse labyrinth at (b) and into an array of isolated regions of separation ['holes'] at (c).

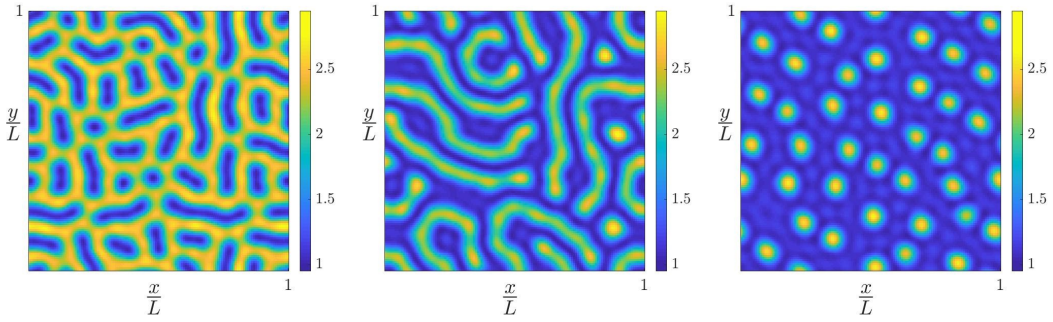

Figure 5.4: Contour plot of the gap $g(x, y)$ during approach at points (a,b,c) in figure 5.3.

Figure 5.5(a,b,c) shows the same results in Fourier transform space. In all cases we see high values clustered near the most unstable wavenumber $\zeta = 2.1$ and the

distribution is axisymmetric within the limits of statistical variance, indicating that the pattern is statistically isotropic.

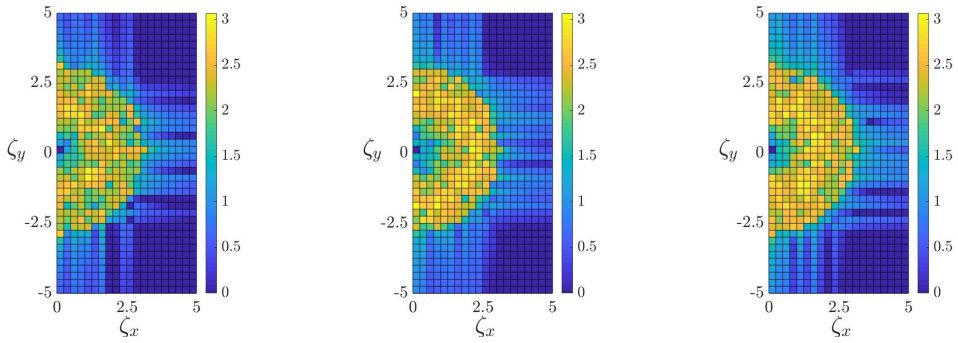

(a) (b) (c)

Figure 5.5: Fourier transform of $g(x, y)$ from Figure 5.4.

5.4 Effect of surface roughness

We assume that the surface is rough with a power spectral density [PSD] of the form

$$P(\zeta) = B\zeta^{-2-2H} \; ; \quad \zeta_1 < \zeta < \zeta_2 \; , \tag{5.13}$$

where B is a constant, H is the Hurst exponent, here taken as $H = 0.2$, and ζ_1, ζ_2 define the range of dimensionless wavenumbers in the spectrum, outside which the spectral content is zero. For the finite domain $L \times L$, a realization of this PSD can be written as

$$u_0(x, y) = \Re \sum_m \sum_n B_{mn} \exp\left[\frac{2\pi\imath(mx + ny)}{L}\right] \; , \tag{5.14}$$

where $u_0(x, y)$ describes the deviation of the surface from the mean plane in the undeformed state, and

$$\frac{\zeta_1 L}{2\pi h} < \sqrt{m^2 + n^2} < \frac{\zeta_2 L}{2\pi h} \; . \tag{5.15}$$

The magnitudes of the coefficients $|B_{mn}|$ were chosen so as to ensure that the resulting surface PSD was of the form Equation 5.13 and the corresponding arguments [phases]

were chosen randomly.

With this definition, the gap can be written

$$g(x,y) = \bar{g} + u_0(x,y) + u(x,y) \ , \tag{5.16}$$

where $u(x,y)$ is given by Equation 5.7. Notice that we arbitrarily assign the value $B_{00} = 0$, so that the roughness makes no contribution to the mean gap. The interface energy is then determined from Equation 5.2 and the constants A_{mn} are chosen so as to minimize Π as in the smooth surface case.

5.4.1 A two-scale approximation

We anticipate that the wavelengths in the roughness spectrum will generally be significantly smaller than the layer thickness, and this suggests the possibility of a scale-separation approach. Compared with the roughness scale, the thickness of the layer is large, so local effects can be approximated by those in a corresponding half space. The effect of the roughness, as compared with a corresponding smooth surface, can therefore be described in terms of a modified traction law.

An inductive method for estimating this law is described in [3]. If the modified traction law $\sigma_M(g, \zeta_0)$ is known for a surface with spectral content only in $\zeta_0 < \zeta < \zeta_2$, where $\zeta_0 > \zeta_1$, the corresponding law for $\sigma_M(g, \zeta_0 - \delta\zeta)$ can be obtained by convoluting $\sigma_M(g, \zeta_0)$ with the additional roughness tranche $\zeta_0 - \delta\zeta < \zeta < \zeta_0$. Successive applications of this technique allow us to determine the modified law for the entire spectrum. In [3], this procedure was implemented using discrete tranches of the spectrum, but the same approach can be used to develop a partial differential equation for $\sigma_M(g, \zeta)$, following the methodology of Persson [91]. The modified traction law for the complete roughness spectrum is then defined by $\sigma_M(g) = \sigma_M(g, \zeta_1)$.

On the scale of the layer thickness, the effect of the surface roughness can then

be approximated by using $\sigma_M(g)$ in place of Equation 5.10, and treating the layer surface as smooth.

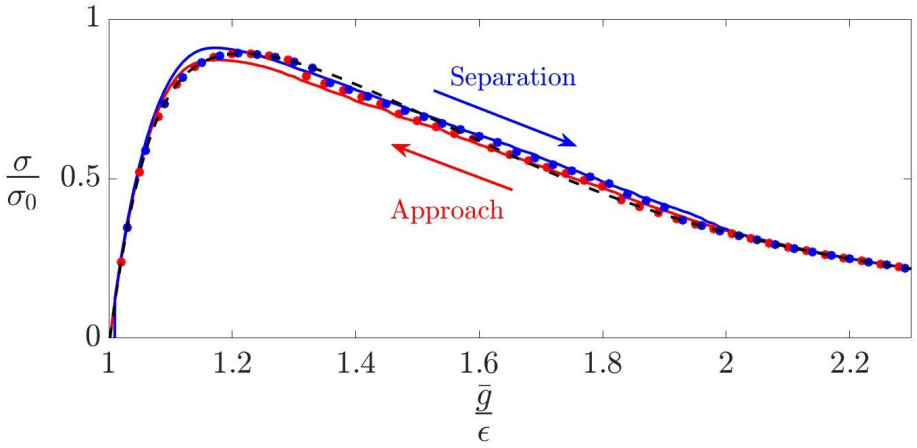

Figure 5.6: Mean traction $\bar{\sigma}$ as a function of mean gap $\bar{g}$ for a layer with fine-scale roughness defined by Equation 5.14 with $\zeta_1 = 6.0, \zeta_2 = 8.0$ and $m_0 = 10^{-2.5}\varepsilon^2$. The solid lines correspond to a direct numerical solution for the rough surface using the Lennard-Jones traction law, whilst the circles were obtained by approximating the effect of roughness through a modified traction law $\sigma_M(g)$ [3] [shown here as a dashed line].

5.4.1.1 Results

Figure 5.6 shows the relation between mean traction and mean gap for an incompressible elastic half space with roughness of the form Equation 5.13 with $\zeta_1 = 6.0, \zeta_2 = 8.0$ and height variance

$$m_0 = 2\pi \int_{\zeta_1}^{\zeta_2} \zeta P(\zeta) d\zeta = 10^{-2.5}\varepsilon^2 \tag{5.17}$$

[92]. In this figure, we compare two methods of solution: (i) a direct numerical solution of the problem [solid line] by minimizing the total energy for a gap defined by Equation 5.16 using the Lennard-Jones traction law and (ii) a solution in which the layer is smooth [$u_0(x, y) = 0$], but the traction law is modified to describe the effect of roughness [circles]. The agreement is clearly extremely good. The advantage

of using the modified traction law is that the deformation of the layer can then be adequately described on a much coarser grid, or equivalently, by a more severely truncated Fourier series, and this is particularly useful if the spectral range $[\zeta_1, \zeta_2]$ is broad.

5.4.2 Identifying instability effects

The argument of the previous section suggests that pattern instabilities should occur if and only if the maximum slope of the modified traction law $\sigma_M(\bar{g})]$ satisfies the condition Equation 5.11 — i.e.

$$\frac{h}{E}\left[-\sigma'_M(g)\right]_{\max} > \frac{1}{0.482}\ , \tag{5.18}$$

If the roughness amplitude is relatively small, this hypothesis can be tested by examining the corresponding contour plots for $g(x, y)$. For example, Figure 5.7(a) shows the contour plot for the actual rough surface during separation at a mean gap $\bar{g} = 1.4$ indicated by the point A in Figure 5.6, and Figure 5.7(b) shows the corresponding pattern predicted for a smooth surface with the modified traction law. There is some blurring of the observed patterns, but the overall morphology is clearly similar.

However, if the roughness amplitude is larger, patterns become more blurred, a typical example being shown in Figure 5.8(a). In this case, detection of instability from gap contours is more difficult, but the corresponding Fourier plot of Figure 5.8(b) clearly shows substantial spectral content in the unstable range near $\zeta = 2.1$. This suggests that we might quantify the extent of pattern formation in the numerical solution for the rough surface using the dimensionless parameter m_0^u/ε^2, where m_0^u is the variance of that part of the gap PSD that lies in the unstable range in the 'smooth' solution, identified in Figure 5.2. We assume here that the roughness PSD has no content in this wavenumber range, since otherwise it would be difficult to

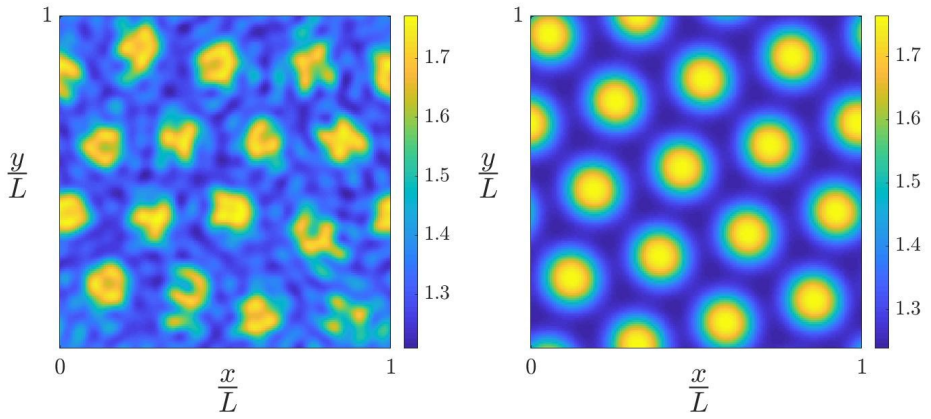

Figure 5.7: Contour plots of gap $g(x, y)$ at a point in the unstable range for $\beta = 0.5$ and roughness defined by $\zeta_1 = 6, \zeta_2 = 8$ and $m_0 = 10^{-2.5}\varepsilon^2$.

distinguish the separate effects of instability and roughness.

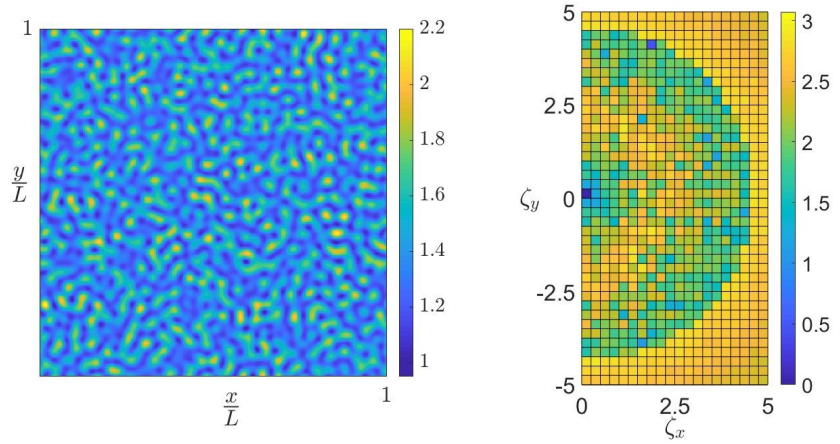

Figure 5.8: (a) Contour plots of gap $g(x, y)$ in the unstable range for $\beta = 0.5$ and roughness defined by $\zeta_1 = 4.5, \zeta_2 = 8$ and $m_0 = 10^{-2}\varepsilon^2$. (b) Fourier domain plot for the gap distribution $g(x, y)$ from (a).

In Figure 5.9 we plot $[m_0^u/\varepsilon^2]_{\max}$, obtained from the numerical solution, as a function of the maximum negative slope of the modified traction law $[-\sigma_M'(\bar{g})]_{\max}$, normalized by the corresponding expression for the Lennard-Jones law. Each set of points corresponds to a different value of the lower wavenumber of the roughness $\zeta_1 = 4.5 : 0.5 : 6.5$ and a range of roughness variances $-2.7 < \log_{10}(m_0/\varepsilon^2) <$

-1.6. Results were obtained under both approach and separation conditions, but no significant difference was observed. The vertical dashed line in Figure 5.9 corresponds to the criterion Equation 5.18, below which the two-scale approximation would predict $m_0^u = 0$, though the direct numerical results exhibit a level of noise as one might expect. However, the results exhibit a remarkable level of consistency, showing that $[-\sigma'_M(\bar{g})]_{\max}$ is a very good indicator of the effect of roughness on the instability, and more generally that the two-scale approach to the layer problem defines a good approximation to important features of the system behaviour.

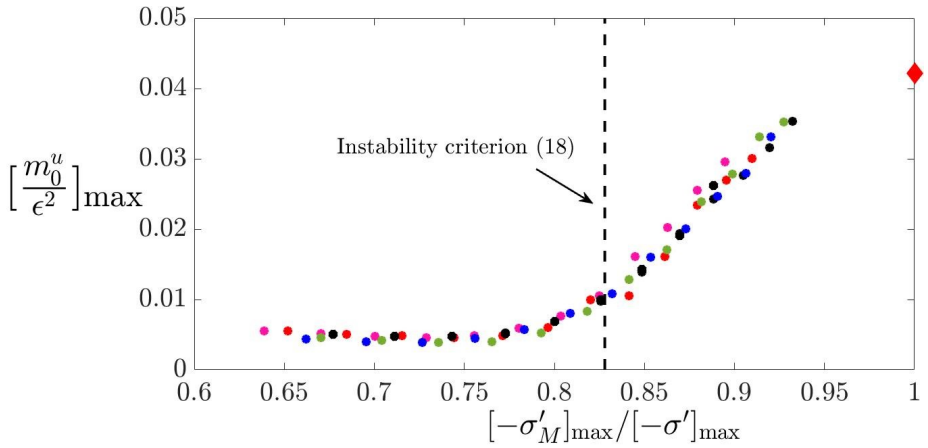

Figure 5.9: Normalized spectral content $[m_0^u/\varepsilon^2]_{\max}$ for the gap $g(x, y)$ in the unstable wavenumber range as a function of the maximum negative slope of the modified traction law $[-\sigma'_M(\bar{g})]_{\max}$. Consistency between several roughness spectra shows that $[-\sigma'_M(\bar{g})]_{\max}$ is a good indicator of the effect of roughness on instability. The point at the top right defines $[m_0^u/\varepsilon^2]_{\max}$ for a smooth layer.

5.5 Conclusions

If a smooth elastic layer is placed close to a plane surface, elastic instabilities due to adhesive tractions lead to the development of patterns and to a modification of the traction-separation law. However, a relatively small amplitude of roughness on the surfaces has a significant effect on this process. Here we have described a model

for analyzing the contact of both rough and smooth surfaces using a double Fourier series.

We also developed a two-scale approximation to the rough contact behaviour, by (i) estimating the effect of roughness on the mean traction between two half spaces, using a previously published method [3], and then (ii) using this modified traction law in the analysis of a smooth elastic layer. Results show that this gives a very good approximation to the traction-separation law obtained by direct numerical simulation. In particular, the development of patterns is predicted if the maximum slope of the modified traction law satisfies the inequality Equation 5.18 and the corresponding results correlate extremely well with a criterion based on the spectral content in the unstable range from the numerical solution.

CHAPTER VI

Relation Between Interfacial Separation and Load on Elastic Rough Surfaces : Partial Differential Equations Approach

6.1 Introduction

Chapter 3 and chapter 5 solved the multiscale problems idealized by PSD with a classical homogenization approach to adhesive contacts. The fine-scale traction laws are investigated, and the fine-scale effects are homogenized to give continuum properties. The homogenized properties are used at the following coarser scale. JTB(chapter 3) developed this discrete process involving interactions. In contrast to the Weierstrass function used in CDBJ with the homogenization process, the rough surface idealized by PSD has a non-zero probability of any given height. The conditional PDF described in Chapter 3 is a Gaussian distribution, but the discrete method's integral domain should be finite. During the iteration, the summation of probability may decrease by leakage at the tail of Gaussian. This leakage problem could be solved with a large enough gap domain and a small enough additional increment Δk or ΔV, resulting in more expensive computational costs. If the discrete method in Chapter 3 could be converted to a diffusional partial differential equation [PDE], the summation would remain unity without increasing the computational complexity.

Persson(2001) derived a simple diffusional differential equation for PDF for pressure in adhesiveless contact using the homogenization approach. The theory does not give the force-displacement relation and PDF for the gap, beneficial for incremental stiffness [and hence electrical contact resistance] and interfacial fluid flow estimates. Therefore, he extended the theory to find tractions with the PDE's simplicity but introduced a semi-empirically determined parameter, a function of the contact area.

This chapter derives two diffusional PDEs for tractions and PDF for a gap, based on the discrete method in Chapter 3. We shall show that the correction factor is unnecessary with the present method. While the discrete method was applied only for adhesive contact in the previous chapters, the PDEs developed in this chapter are extended to adhesiveless contact due to the PDE's simplicity. This development allows us to compare PDE results with rigorous simulations such as GFMD and MD. As the bandwidth of PSD in GFMD or MD increases, the rough surface in numerical simulation idealizes an entire surface more accurately. The bandwidth must be constrained, because it increases computational cost with $O(n\sqrt{n}\log n)$. In this sense, 'Contact Challenge' shows the best result from rigorous simulations with three decades bandwidth to compare with theoretical models. The PDE method will be compared with the GFMD result from 'Contact Challenge' and theoretical result from Persson's model. To verify that the agreement of the results with 'Contact Challenge' is not a coincidence, we shall compare the MD result with 648 bandwidth from Yang and Persson(2008) and the present PDE method. For the adhesive contact case, the GFMD results with 64 bandwidth from Persson and Scaraggi(2014) are compared with the PDE method.

6.2 Theory

In Chapter 3, the mean traction between the rough surfaces for only the range (k_a, k_b) of roughness can be written by convolution as

$$\sigma(g; k_a, k_b) = \int_0^\infty \Phi(s|g; k_a, k_b)\sigma(s)ds, \tag{6.1}$$

where g now denotes the mean gap. We assumed that if the wavenumber increment $(k_b - k_a)$ is sufficiently small, $\Phi(s|g; k_a, k_b)$ will be approximately Gaussian, — *i.e.*

$$\Phi(s|g; k_a, k_b) \approx \mathcal{N}(s|g, V) \equiv \frac{1}{\sqrt{2\pi V}} \exp\left(-\frac{(s-g)^2}{2V}\right), \tag{6.2}$$

where the variance

$$V(k_a, k_b; \sigma(g)) = 2\pi \int_{k_b}^{k_a} qP(q)\left[1 + \frac{2}{E^* q}\frac{\partial \sigma}{\partial g}\right]^{-2} dq. \tag{6.3}$$

More generally, if $\sigma(g; k_b, k_2)$ is known, the effect of adding the increment (k_a, k_b) to the PSD can be obtained as

$$\sigma(g; k_a, k_2) = \int_0^\infty \mathcal{N}(s|g, V)\sigma(s; k_b, k_2)ds, \tag{6.4}$$

where $V = V(k_a, k_b; \sigma(g; k_b, k_2)$. In Chapter 3, we used this relation iteratively with [small] discrete intervals $\Delta k = k_b - k_a$ to develop a numerical solution for the modified traction law $\sigma(g; k_1, k_2)$, where $k_1 < k_a$.

The same conditional probability is used to update the gap probability $\Phi(g)$ in the direction of increasing wavenumber, using the convolution

$$\Phi(g|g_0; k_1, k_b) = \int_0^\infty \Phi(s|g; k_1, k_a)\Phi(g|s; k_a, k_b)ds. \tag{6.5}$$

6.2.1 Derivation of partial differential equations

Writing $k_b = k$ in Equation 6.4, differentiating with respect to k_a, and taking the limit as $k_a \to k$, we obtain

$$-\frac{\partial \sigma}{\partial k}(g;k,k_2) = \lim_{k_a \to k} \int_0^\infty \sigma(s;k,k_2) \frac{\partial \mathcal{N}(s|g,V)}{\partial k_a} ds. \tag{6.6}$$

Now,

$$\frac{\partial \mathcal{N}}{\partial k_a} = \frac{\partial \mathcal{N}}{\partial V}\frac{\partial V}{\partial k_a} = \frac{1}{2}\frac{\partial^2 \mathcal{N}}{\partial s^2}\frac{\partial V}{\partial k_a} \tag{6.7}$$

and for sufficiently small $\Delta k \equiv k - k_a$,

$$-\frac{\partial V}{\partial k_a} = U(g;k,k_2) \equiv 2\pi k P(k) \left[1 + \frac{2}{E^* k}\frac{\partial \sigma(g;k,k_2)}{\partial g}\right]^{-2}, \tag{6.8}$$

from Equation 6.3. In the limit, the right-hand side of Equation 6.6 therefore becomes

$$-\frac{1}{2}U(g;k,k_2)\int_0^\infty \sigma(s;k,k_2)\frac{\partial^2 \mathcal{N}}{\partial s^2} ds. \tag{6.9}$$

Integrating by parts twice and noting that in the limit $\Delta k \to 0$, the Gaussian function $\mathcal{N}$ and its derivative will be zero at $s = 0, \infty$, we obtain the partial differential equation

$$\frac{\partial \sigma}{\partial k}(g;k,k_2) = \frac{1}{2}U(g;k,k_2)\frac{\partial^2 \sigma}{\partial g^2}(g;k,k_2). \tag{6.10}$$

An essentially similar procedure applied to Equation 6.5 yields the partial differential equation

$$\frac{\partial \Phi(g|g_0;k_1,k)}{\partial k} = \frac{1}{2}\frac{\partial^2}{\partial g^2}\left[U(g;k,k_2)\Phi(g|g_0;k_1,k)\right], \tag{6.11}$$

for the conditional probability $\Phi(g|g_0;k_1,k)$.

There are some significant differences between these two partial differential equa-

tions, notably

1. Equation 6.11 requires values of the function $U(g; k, k_2)$ which includes the traction law $\sigma(g; k, k_2)$. Thus, the gap distribution can be found only after Equation 6.10 has been solved for the traction law.

2. The function $\sigma(g; k, k_2)$ has an independent physical meaning for all values of k. It represents the traction law appropriate to a rough surface containing only that part of the PSD in (k, k_2). This is not the case for $\Phi(g|g_0; k_1, k)$, since Equation 6.11 makes implicit reference to the rest of the PSD (k, k_2) through the function $U(g; k, k_2)$. In effect, Equation 6.11 is just a step on the way to the solution for the gap distribution $\Phi(g|g_0; k_1, k)$ for the entire PSD.

6.3 Boundary and initial conditions

Equation 6.10 and Equation 6.11 have the form of modified diffusion equations with the wavenumber k as a time-like variable. It is therefore natural to describe the conditions at $k = k_1$ or $k = k_2$ as *initial conditions*, and those at $g = 0$ or $g \to \infty$ as *boundary conditions*.

6.3.1 Initial conditions

Equation 6.10: The function $\sigma(g; k_2, k_2)$ defines the traction between two completely plane surfaces separated by a distance g. For problems involving adhesive forces, this will typically be something like the Lennard-Jones/Maugis traction law.

However, we also plan to use the present formalism to examine the effect of surface roughness in problems without adhesion, for which the most natural choice would be the 'hard contact law' $\sigma g = 0, \sigma \leq 0, g \geq 0$. Clearly this cannot be used to initiate a numerical solution of Equation 6.10, but we shall show that a regularized

approximation of the form

$$\frac{p(g)}{E^*} = (Ck_2 g)^{-N} \tag{6.12}$$

can be so used, and that the results converge as the regularization parameter C is increased, tending to the hard contact limit.

Equation 6.11: The corresponding initial condition for Equation 6.11 is the delta function

$$\Phi(g|g_0; k_1, k_1) = \delta(g - g_0), \tag{6.13}$$

since if no part of the PSD is included, the surface will remain plane and the gap will be uniform. For numerical solution, this also has to be regularized as a Gaussian distribution, but the results will be shown to converge as the variance of this distribution is reduced. This initial condition also implies that the numerical solution of Equation 6.11 must progress from coarse to fine roughness [k_1 to $k2$], in contrast to Equation 6.10 which is solved from k_2 to k_1.

6.3.2 Boundary conditions

The conditional probability $\Phi(g|g_0; k_1, k)$ tends strongly to zero at both $g = 0$ and $g \to \infty$, since small gaps are prevented by the corresponding large contact pressures, and large ones by their large distance from the initial condition. Thus, if the necessarily finite calculation domain $g_1 < g < g_2$ is chosen to be sufficiently large, the results should be insensitive to the precise boundary conditions used. For numerical purposes we used a discrete version of the condition

$$\frac{\partial^2}{\partial g^2}\Phi(g|g_0; k_1, k) = 0 \; ; \quad g = g_1, g_2. \tag{6.14}$$

Numerical convergence was tested by allowing g_1, g_2 to get nearer to the limits $(0, \infty)$ and also by checking to make sure that

$$\int_{g_1}^{g_2} \Phi(g|g_0; k_1, k) dg = 1 \; ; \quad \forall k \in [k_1, k_2] \tag{6.15}$$

—in other words, that no probability has 'leaked' out of the domain. The traction law $\sigma(g; k, k_2)$ can be written as a convolution integral, Equation 6.1, so if the range (g_1, g_2) is sufficiently large for $\Phi(s|g; k, k_2)$ to be negligible near the boundaries $g_1, g_2, \sigma(g; k, k_2)$ should also be insensitive to the exact boundary condition used. This was indeed found to be true at the large g limit $g \to g_2$, where $\sigma(g) \to 0$. At this boundary, we used the condition

$$\frac{\partial^2}{\partial g^2} \sigma(g; k, k_2) = 0 \; ; \quad g = g_2. \tag{6.16}$$

However, the combination of a negligibly small gap probability and an extremely large traction near $g = g_1$ tends to cause numerical instabilities. In this range, we found, essentially by trial and error, that the boundary condition

$$\frac{\partial^2}{\partial g^2} \log \left(\frac{\sigma(g)}{E^*} \right) = 0 \; ; \quad g = g_1 \tag{6.17}$$

leads to a numerically converged result, the validity of which is justified by the fact that the corresponding gap probability remains negligibly small near the boundary.

6.4 Results

The PDE method derived in Section 6.3 is compared with the discrete method in Chapter 3. Then, the method is compared with the numerical methods such as GFMD and MD and Persson's theoretical method. For the comparisons, data are extracted

from 'Contact Challenge,' Persson and Yang(2008), and Persson and Scaraggi(2014). When two PDEs are numerically solved, a regular mesh grid is used for gap and additional roughness ΔV. The convergences are checked with the finer mesh grid and the wider gap range for all results in this section.

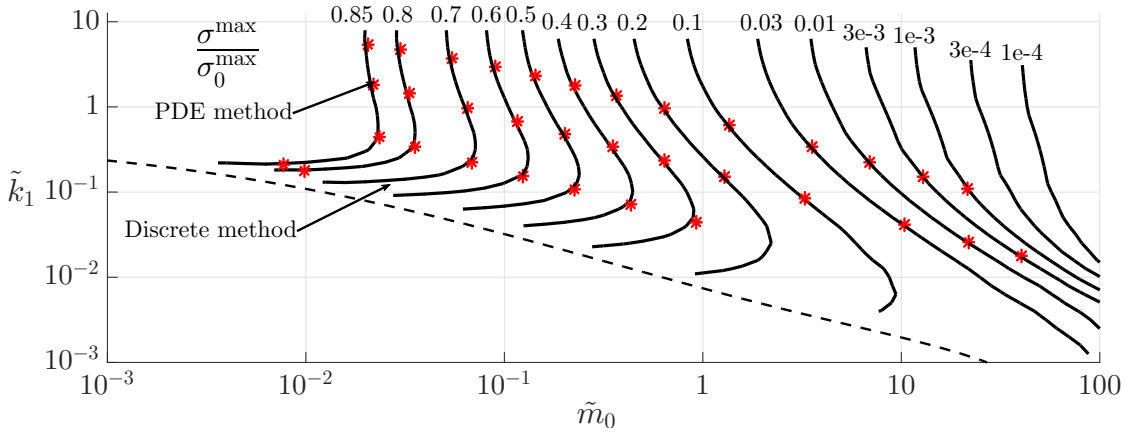

Figure 6.1: PDE method (Equation 6.10) on the same contour plot Figure 3.8.

Figure 6.1 shows pull-off from the PDE method on the contour result from the discrete method (See Figure 3.8). This comparison verifies that PDE methods result in the same solution as the discrete methods for various rough surfaces.

The 'Contact Challenge' presented GFMD results for one rough surface idealized by PSD, where $k_1 = 20\pi mm^{-1}$, $k_r/k_1 = 5$, $k_2/k_1 = 10^3$, $H = 0.8$, and $h_{\text{rms}} = 0.762\mu m$. As explained in Section 1.5, theoretical models participated in the sport, and Persson's results agreed well with the GFMD result in the paper, while asperity models showed deviation. The paper used a very weak adhesive law for computational convenience. Therefore, we treat the problem as the adhesiveless contact. Figure 6.2 shows resulting traction from different regularized adhesiveless contact laws for 'Contact Challenge' PSD. The contact law is $p(g)/E^* = (Ck_2g)^{-N}$, where C and N are regularization parameters. When C in the contact law is between 10 up to 10^3 with $N = 20$, the resulting tractions show one unique solution. The nu-

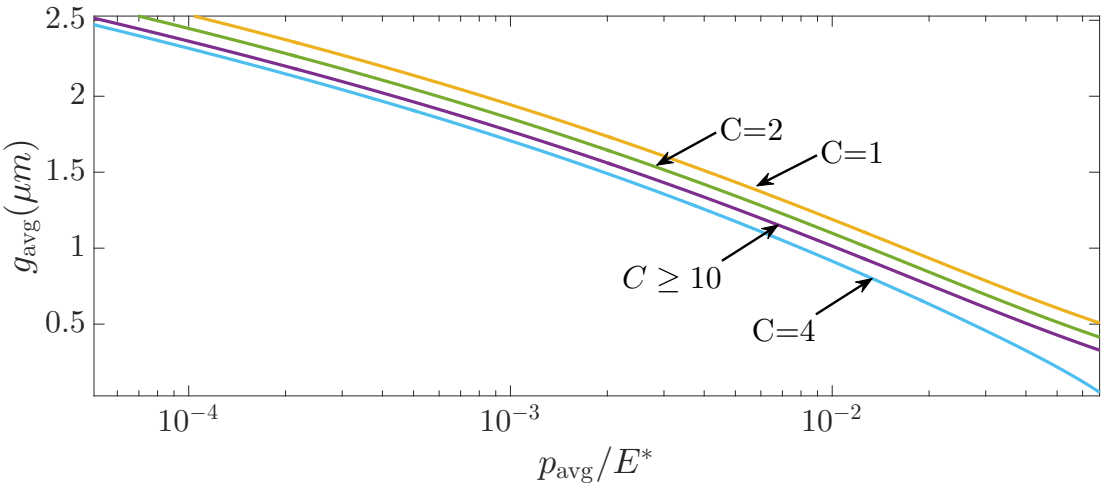

Figure 6.2: Mean gap and mean pressure normalized by composite modulus. The regularized approximation, $\frac{p(g)}{E^*} = (Ck_2g)^{-N}$, is used for the rough surface described in 'Contact Challenge'. As C increases up to 10^3 with $N = 20$, the results show one unique solution.

merical mesh grid for this problem was defined by $\Delta g = 0.01mm$, $\Delta V = 3\text{e}{-5}mm^2$, $g_1 = 0.1mm$, and $g_2 = 10mm$.

Figure 6.3 shows traction from 'Contact Challenge,' Persson's model, and the PDE method. The PDE result is the same as the unique solution in Figure 6.2. 'Contact Challenge' and Persson's model are extracted from Figure 12 in the Challenge paper. Two theoretical models show greater pressure at a larger gap because the height of rough surfaces' configuration is inevitably limited in GFMD. However, in theoretical models, the rough surface idealized by PSD has a non-zero probability of any given height.

Figure 6.4 shows PDF for gap at mean gap 1 µm from 'Contact Challenge,' Persson's model, and the PDE method. Both theoretical models deviate for small gaps ($g < 0.06\,\mu\text{m}$), showing higher probability density than the 'Contact Challenge' due to the limited height of the configuration of the rough surface. The summation of the resulting PDF from the PDE method is 0.989. The leakage inevitably occurred mainly at g_1.

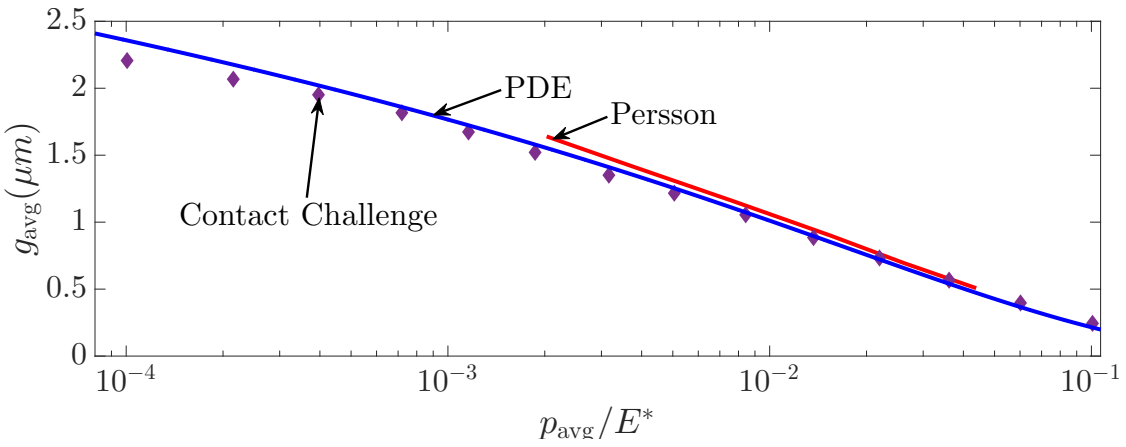

Figure 6.3: Mean gap and mean pressure normalized by composite modulus. 'Contact Challenge' and Persson's data are extracted from Fig.12 in the contact challenge paper.

In Yang and Persson(2008), Persson developed the Equation 1.11, comparing with MD simulation for a PSD, where $k_1 = 6.04\text{E}7m^{-1}$, $k_r/k_1 = 3$, $k_2/k_1 = 648$, $H = 0.8$, and $h_{\text{rms}} = 1nm$. Figure 6.5 shows tractions from MD, Persson's model, and the PDE method. A mesh grid for the PDE method is defined by $\Delta g = 0.0062nm$, $\Delta V = 3\text{e}{-6}nm^2$, $g_1 = 0.01nm$, and $g_2 = 10nm$. Like in Figure 6.3, Figure 6.5 shows roughly logarithmic trends and both theoretical models result in greater pressure than MD at $g > 2nm$, although Persson's model shows earlier deviation.

Figure 6.6 shows the probability density function for the gap at two different mean pressure, $p/E^* = 0.002$ and 0.013. The results of the PDE method are compared with only MD because Persson's data were not available. The summations of the probability from the PDE method are 0.995 and 0.968.

In the Persson and Scaraggi(2014), Persson extended his model into adhesion law for both JKR and DMT limit, comparing with GFMD results with using Lennard-Jones law as the adhesive law. PSD of the rough surface is $k_1 = 2.5\text{E}5m^{-1}$, $k_r/k_1 = 4$, $k_2/k_1 = 64$, $H = 0.8$, and $h_{\text{rms}} = 0.52nm$. Figure 6.8 shows tractions normalized by

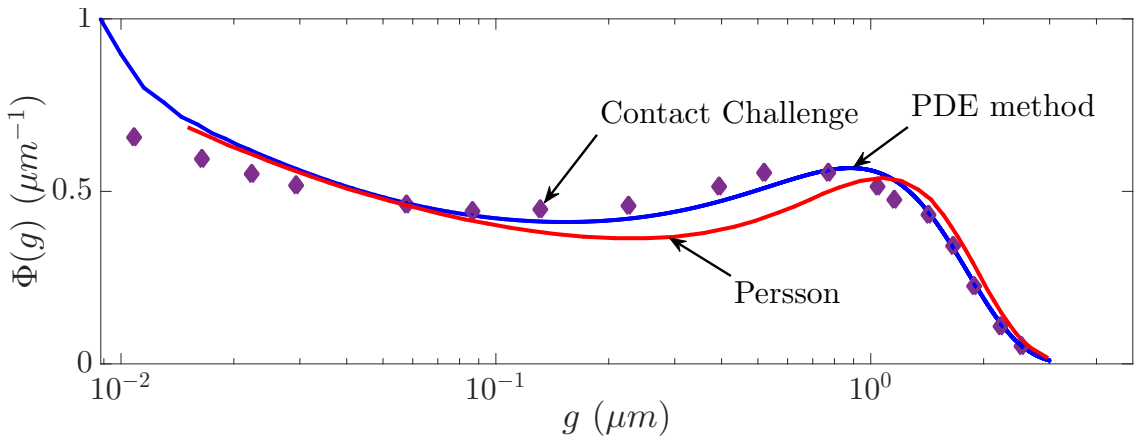

Figure 6.4: Probability density function for gap at mean gap 1 µm. 'Contact Challenge' and Persson's data are extracted from Fig.8 in contact challenge paper.

a maximum tensile stress of the law, and both theoretical models agree well with GFMD. Two different Lennard-Jones laws are used as the adhesive law on the same rough surface. According coefficients for the dimensionless wavenumber suggested in Equation 3.13 are $\chi = 2.5\text{e}{-6}m$ and $6.25\text{e}{-7}m$. A mesh grid for the PDE method is defined by $\Delta g = 0.01\epsilon$, $\Delta V = 1\text{e}{-4}\chi^2$, $g_1 = 0.3\epsilon$, and $g_2 = 10\epsilon$.

6.5 Conclusion

We derived two diffusional PDEs for traction and PDF for a gap, based on the discrete method developed in Chapter 3. We verified that the PDE results are the same as the discrete method in the pull-off contour plot. With the PDE's simplicity, we extend the method to the adhesiveless contact case. For the adhesiveless contact, due to its singularity at the near-zero gap, we introduced the regularized adhesiveless law to solve the PDE numerically. As the regularized laws become close to the Signori's condition, the resulting tractions converge to one unique solution. Although the unique solutions agree well with 'Contact Challenge' and MD, its boundary condition would benefit from additional study. Because the height of the configuration in numerical

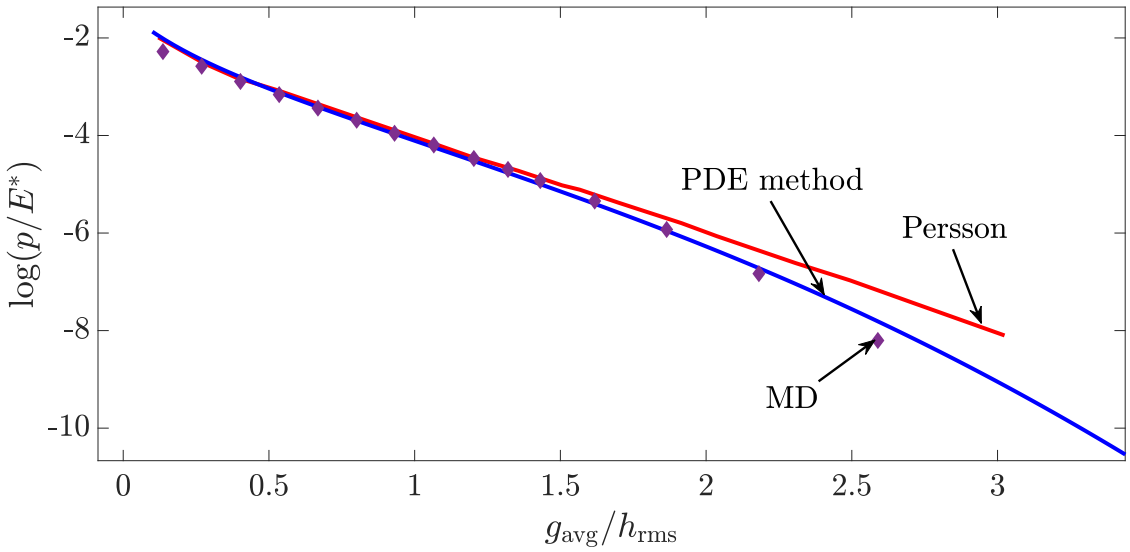

Figure 6.5: Traction for Yand and Persson(2008). MD and Persson's data are extracted from Fig.11 in the paper. Both theoretical models resulted in higher pressure than MD at $g > 2nm$.

simulations such as GFMD and MD is limited, both Persson's and the present PDE method showed qualitatively correct deviation for the traction and the probability for a gap. Notably, the PDE method agreed well without using any correction factors.

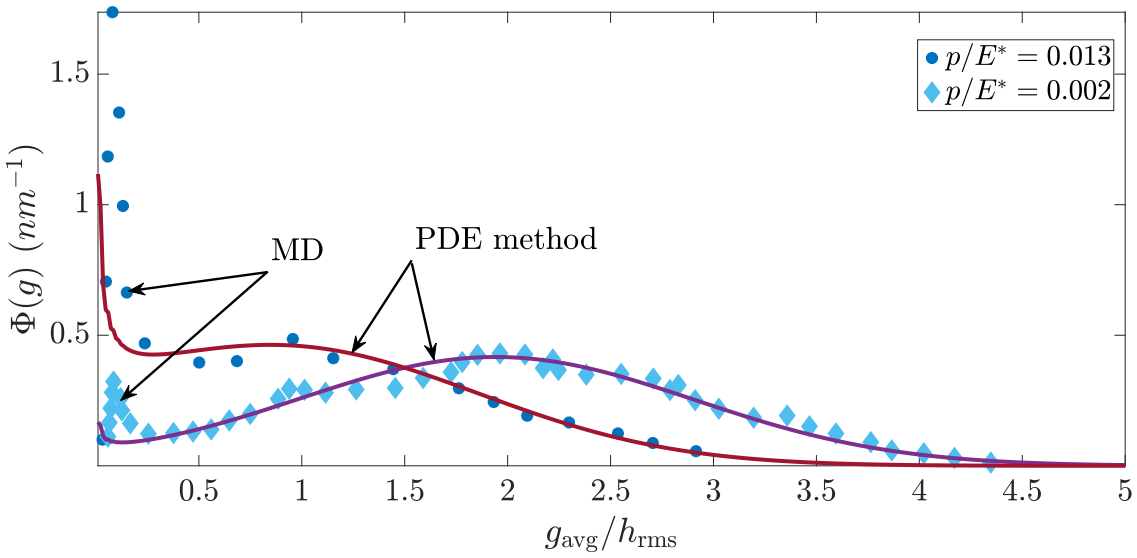

Figure 6.6: Probability density function for gap at mean pressure $p/E^* = 0.002$ and 0.013. MD results are extracted from Fig.5 in the paper.

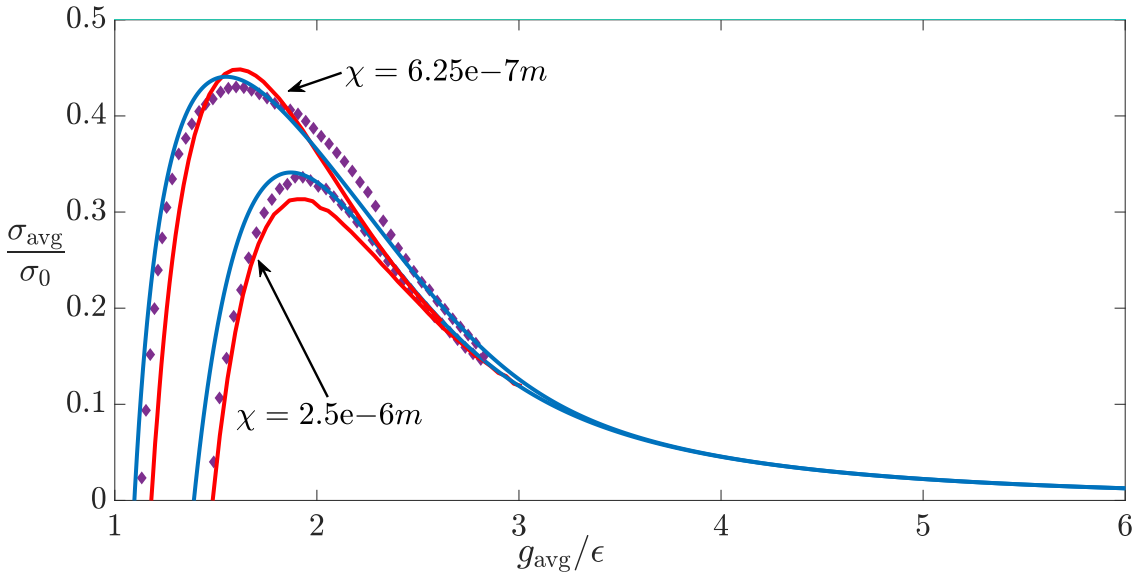

Figure 6.7: GFMD(purple dot) and Persson's data(red line) are extracted from Fig.17 in Persson and Scaraggi(2014). Mean gap and mean traction are normalized by Lennard-Jones equilibrium spacing and its maximum tensile traction, which is 0.103GPa and 0.412GPa for $\Delta\gamma = 0.1$J/m and $\Delta\gamma = 0.4$J/m each. PDE method(blue line) used same parameters.

CHAPTER VII

Conclusions and Future Directions

7.1 Conclusions

Every surface has roughness; the roughness changes physical properties of contact such as electrical and thermal conductivity, friction coefficient, wear, lubrication, and interfacial flow between surfaces. Understanding the effect of the roughness requires multidisciplinary knowledge such as elasticity, plasticity, fluid dynamics and chemical and thermal interaction. Also, physical and chemical effects on the roughness vary depending on the scale of time and space. Due to the complexity of the roughness, the fundamental mechanism has not been studied enough.

As computational power has been increased, numerical methods analyzing the effect of roughness have been developed. The finite element method [FEM] prescribe constitutive laws of the material and molecular dynamics [MD] uses intermolecular potential energy each within the discretization of volume. Green's function molecular dynamics [GFMD] describes only surfaces as MD and uses a boundary element method [BEM], where simple theoretical solutions of point load on the surface are used.

The numerical methods result in the exact solution with a refined meshgrid to precisely depict an actual rough surface. Still, the methods require highly expensive computational costs. On the other hand, theoretical models suggest simple solu-

tions and a fundamental understanding of the effect of roughness. Therefore, despite the development of numerical methods, theoretical models to analyze the effect of roughness should also be developed.

As a pivotal theory, Greenwood and Williamson [GW] theory idealized rough surfaces as spherical asperities, assuming that 1) the asperities are independent, 2) curvature of the asperities are the same, and 3) the distribution of summit is Gaussian or exponential. While it was revealed that rough surfaces are multiscaled by self-affine fractal, of which range shows a power-law type of power spectral density [PSD], the multiscale property of the roughness is not explained in GW's asperity model. Also, the interaction between asperities becomes a problem at fine-scale roughness.

Persson's theoretical model is another seminal work, explaining the multiscale property. Persson's theory resulted in a simple diffusional partial differential equation [PDE] for probability density function [PDF] for a mean pressure, derived by an iterative method on adhesiveless contact. The method idealizes the rough surface as a sum of different scales of roughness. The PDF for pressure is obtained by iteratively adding infinitesimal roughness to known PDF, which is a Dirac-delta function for an initial condition. Assuming that the contact remains as full contact, the known PDF is diffused by Gaussian, of which variance is m_2 of the added roughness. Persson extended his theory for other properties such as load-displacement relation, adhesion, interfacial liquid flow, and rubber friction coefficient. However, it is required to introduce a semi-empirical correct factor, a function of the contact area.

This dissertation focused on developing a model for load-displacement relation and PDF for mean gaps by linear-elastic deformation on isotropic Gaussian rough surfaces. Persson's model has inspired the present method. However, instead of using full-contact assumption, we assumed that added infinitesimal roughness is deformed by a homogenized traction law from rest fine scale of PSD, resulting in diffusional PDEs for load-displacement relation and PDF for mean gaps. The present PDE

method could also be applied to both adhesive and adhesiveless contact.

The present PDE method was compared with numerical methods and theoretical models from other papers. Among the papers, 'Contact Challenge' used the largest bandwidth, depicting the actual rough surface more precisely. In 'Contact Challenge,' theoretical and numerical methods and experiments were compared for weak adhesion contact on one rough surface. Most of the results agreed well, but asperity models showed significant deviation from numerical results. Noticeably, the present PDE method showed an excellent agreement with numerical results, but it showed a deviation at large mean gaps. While the height of surface configuration is constrained in the numerical method, rough surfaces idealized by PSD have a non-zero probability for any given height. This difference caused the present PDE method and Persson's theory to show larger mean pressure at $g > 3h_{\mathrm{rms}}$.

Although the comparison agreed well, there are three limitations in the present theory. First, we could not use a boundary condition that traction goes to infinity at zero gaps because the singularity of traction near zero gap causes PDE instability. Instead, its boundary condition near zero gaps was obtained by trial and error. Second, the actual rough surfaces are neither isotropic nor Gaussian, and has finite height, while we used isotropic Gaussian surface in the theoretical model. Third, the present model was derived from linear elasticity, but the actual rough surfaces are plastically deformed, because contact occurs at tips of rough surfaces. We leave this limitation as future works.

BIBLIOGRAPHY

[1] D Maugis. Adhesion of spheres: the JKR-DMT transition using a Dugdale model. *Journal of Colloid and Interface Science*, 150(1):243–269, 1992.

[2] BNJ Persson and M Scaraggi. Theory of adhesion: role of surface roughness. *The Journal of Chemical Physics*, 141(12):124701, 2014.

[3] J Joe, MD Thouless, and JR Barber. Effect of roughness on the adhesive tractions between contacting bodies. *Journal of the Mechanics and Physics of Solids*, 118:365–373, 2018.

[4] JE Jones. On the determination of molecular fields.—ii. from the equation of state of a gas. *Proceedings of the Royal Society of London. Series A, Containing Papers of a Mathematical and Physical Character*, 106(738):463–477, 1924.

[5] D Maugis. *Contact, Adhesion and Rupture of Elastic Solids*, volume 130. Springer Science & Business Media, 2013.

[6] B Derjaguin. Untersuchungen über die reibung und adhäsion, iv. *Kolloid-Zeitschrift*, 69(2):155–164, 1934.

[7] RS Bradley. LXXIX. The cohesive force between solid surfaces and the surface energy of solids. *The London, Edinburgh, and Dublin Philosophical Magazine and Journal of Science*, 13(86):853–862, 1932.

[8] H Rumpf. *Particle Technology*, volume 1. Springer Science & Business Media, 2012.

[9] YI Rabinovich, JJ Adler, A Ata, RK Singh, and BM Moudgil. Adhesion between nanoscale rough surfaces: I. Role of asperity geometry. *Journal of Colloid and Interface Science*, 232(1):10–16, 2000.

[10] KL Johnson, K Kendall, and AD Roberts. Surface energy and the contact of elastic solids. *Proceedings of the Royal Society of London. A. Mathematical and Physical Sciences*, 324(1558):301–313, 1971.

[11] KL Johnson. The adhesion of two elastic bodies with slightly wavy surfaces. *International Journal of Solids and Structures*, 32(3-4):423–430, 1995.

[12] VL Popov, R Pohrt, and Q Li. Strength of adhesive contacts: influence of contact geometry and material gradients. *Friction*, 5(3):308–325, 2017.

[13] VM Muller, VS Yushchenko, and BV Derjaguin. On the influence of molecular forces on the deformation of an elastic sphere and its sticking to a rigid plane. *Journal of Colloid and Interface Science*, 77(1):91–101, 1980.

[14] D Tabor. Surface forces and surface interactions. In *Plenary and Invited Lectures*, pages 3–14. Elsevier, 1977.

[15] BV Derjaguin, VM Muller, and YP Toporov. Effect of contact deformations on the adhesion of particles. *Journal of Colloid and Interface Science*, 53(2):314–326, 1975.

[16] MD Pashley. Further consideration of the DMT model for elastic contact. *Colloids and Surfaces*, 12:69–77, 1984.

[17] JA Greenwood. On the DMT theory. *Tribology Letters*, 26(3):203–211, 2007.

[18] JA Greenwood. Adhesion of elastic spheres. *Proceedings of the Royal Society of London. Series A: Mathematical, Physical and Engineering Sciences*, 453(1961):1277–1297, 1997.

[19] JA Greenwood and KL Johnson. An alternative to the maugis model of adhesion between elastic spheres. *Journal of Physics D: Applied Physics*, 31(22):3279, 1998.

[20] KL Johnson and JA Greenwood. An adhesion map for the contact of elastic spheres. *Journal of Colloid and Interface Science*, 192(2):326–333, 1997.

[21] M Ciavarella, JA Greenwood, and JR Barber. Effect of tabor parameter on hysteresis losses during adhesive contact. *Journal of the Mechanics and Physics of Solids*, 98:236–244, 2017.

[22] UD Schwarz. A generalized analytical model for the elastic deformation of an adhesive contact between a sphere and a flat surface. *Journal of Colloid and Interface Science*, 261(1):99–106, 2003.

[23] FP Bowden and D Tabor. *The Friction and Lubrication of Solids*, volume 1. Oxford university press, 2001.

[24] D Tabor. *The Hardness of Metals*. Oxford university press, 2000.

[25] BB Mandelbrot, DE Passoja, and AJ Paullay. Fractal character of fracture surfaces of metals. *Nature*, 308(5961):721–722, 1984.

[26] KNG Fuller and D Tabor. The effect of surface roughness on the adhesion of elastic solids. *Proceedings of the Royal Society of London. A. Mathematical and Physical Sciences*, 345(1642):327–342, 1975.

[27] JA Greenwood and JBP Williamson. Contact of nominally flat surfaces. *Proceedings of the Royal Society of London. Series A. Mathematical and Physical Sciences*, 295(1442):300–319, 1966.

[28] BNJ Persson and E Tosatti. The effect of surface roughness on the adhesion of elastic solids. *The Journal of Chemical Physics*, 115(12):5597–5610, 2001.

[29] M Ciavarella and A Papangelo. Discussion of "measuring and understanding contact area at the nanoscale: A review"(jacobs, tdb, and ashlie martini, a., 2017, asme appl. mech. rev., 69 (6), p. 060802). *Applied Mechanics Reviews*, 69(6), 2017.

[30] AW Bush, RD Gibson, and TR Thomas. The elastic contact of a rough surface. *Wear*, 35(1):87–111, 1975.

[31] C Putignano, L Afferrante, G Carbone, and G Demelio. A new efficient numerical method for contact mechanics of rough surfaces. *International Journal of Solids and Structures*, 49(2):338–343, 2012.

[32] G Carbone and F Bottiglione. Asperity contact theories: do they predict linearity between contact area and load? *Journal of the Mechanics and Physics of Solids*, 56(8):2555–2572, 2008.

[33] BNJ Persson. Relation between interfacial separation and load: a general theory of contact mechanics. *Physical Review Letters*, 99(12):125502, 2007.

[34] A Papangelo, N Hoffmann, and M Ciavarella. Load-separation curves for the contact of self-affine rough surfaces. *Scientific Reports*, 7(1):1–7, 2017.

[35] JR Barber. Bounds on the electrical resistance between contacting elastic rough bodies. *Proceedings of the Royal Society of London. Series A: Mathematical, Physical and Engineering Sciences*, 459(2029):53–66, 2003.

[36] SP Venugopalan, MH Müser, and L Nicola. Green's function molecular dynamics meets discrete dislocation plasticity. *Modelling and Simulation in Materials Science and Engineering*, 25(6):065018, 2017.

[37] L Pastewka and MO Robbins. Contact between rough surfaces and a criterion for macroscopic adhesion. *Proceedings of the National Academy of Sciences*, 111(9):3298–3303, 2014.

[38] MH Müser, WB Dapp, R Bugnicourt, P Sainsot, N Lesaffre, TA Lubrecht, BNJ Persson, K Harris, A Bennett, K Schulze, et al. Meeting the contact-mechanics challenge. *Tribology Letters*, 65(4):1–18, 2017.

[39] Martin H Müser, Wolf B Dapp, Romain Bugnicourt, Philippe Sainsot, Nicolas Lesaffre, Ton A Lubrecht, Bo NJ Persson, Kathryn Harris, Alexander Bennett, Kyle Schulze, et al. Meeting the contact-mechanics challenge. *Tribology Letters*, 65(4):118, 2017.

[40] JA Greenwood and JBP Williamson. Proceedings of the royal society of london series a: Mathematical. *Physical and Engineering Sciences*, 295:300–319, 1966.

[41] M Ciavarella, G Demelio, JR Barber, and YH Jang. Linear elastic contact of the Weierstrass profile. *Proceedings of the Royal Society of London. Series A: Mathematical, Physical and Engineering Sciences*, 456(1994):387–405, 2000.

[42] W Manners and JA Greenwood. Some observations on Persson's diffusion theory of elastic contact. *Wear*, 261(5-6):600–610, 2006.

[43] PR Nayak. Random process model of rough surfaces. *Journal of Lubrication Technology*, 93(3):398–407, 1971.

[44] H Aramaki, HS Cheng, and Y Chung. The contact between rough surfaces with longitudinal texture-part I: average contact pressure and real contact area. 1993.

[45] JA Greenwood and JJ Wu. Surface roughness and contact: an apology. *Meccanica*, 36(6):617–630, 2001.

[46] M Borri-Brunetto, A Carpinteri, and B Chiaia. Lacunarity of the contact domain between elastic bodies with rough boundaries. In *Probamat-21st Century: Probabilities and Materials*, pages 45–64. Springer, 1998.

[47] Y Gao and AF Bower. Elastic-plastic contact of a rough surface with Weierstrass profile. *Proceedings of the Royal Society A: Mathematical, Physical and Engineering Sciences*, 462(2065):319–348, 2006.

[48] KNG Fuller and D Tabor. The effect of surface roughness on the adhesion of elastic solids. *Proceedings of the Royal Society of London. A. Mathematical and Physical Sciences*, 345(1642):327–342, 1975.

[49] N Yu and AA Polycarpou. Adhesive contact based on the Lennard-Jones potential: a correction to the value of the equilibrium distance as used in the potential. *Journal of Colloid and Interface Science*, 278(2):428–435, 2004.

[50] JJ Gilman. Direct measurements of the surface energies of crystals. *Journal of applied physics*, 31(12):2208–2218, 1960.

[51] P Beckmann. Statistical distribution of the amplitude and phase of a multiply scattered field. *Journal of Research of the National Bureau of Standards, 66D*, 3:231–240, 1962.

[52] A Almqvist, C Campana, N Prodanov, and BNJ Persson. Interfacial separation between elastic solids with randomly rough surfaces: comparison between theory and numerical techniques. *Journal of the Mechanics and Physics of Solids*, 59(11):2355–2369, 2011.

[53] M Ciavarella and L Afferrante. Adhesion of rigid rough contacts with bounded distribution of heights. *Tribology International*, 100:18–23, 2016.

[54] KL Johnson. The adhesion of two elastic bodies with slightly wavy surfaces. *International Journal of Solids and Structures*, 32(3-4):423–430, 1995.

[55] PR Guduru. Detachment of a rigid solid from an elastic wavy surface: theory. *Journal of the Mechanics and Physics of Solids*, 55(3):445–472, 2007.

[56] BB Mandelbrot, DE Passoja, and AJ Paullay. Fractal character of fracture surfaces of metals. *Nature*, 308(5961):721–722, 1984.

[57] J Joe, M Scaraggi, and JR Barber. Effect of fine-scale roughness on the tractions between contacting bodies. *Tribology International*, 111:52–56, 2017.

[58] A Ghatak, MK Chaudhury, V Shenoy, and A Sharma. Meniscus instability in a thin elastic film. *Physical Review Letters*, 85(20):4329, 2000.

[59] A Ghatak and MK Chaudhury. Adhesion-induced instability patterns in thin confined elastic film. *Langmuir*, 19(7):2621–2631, 2003.

[60] J Sarkar, V Shenoy, and A Sharma. Patterns, forces, and metastable pathways in debonding of elastic films. *Physical review letters*, 93(1):018302, 2004.

[61] J Sarkar, A Sharma, and V Shenoy. Adhesion and debonding of soft elastic films: crack patterns, metastable pathways, and forces. *Langmuir*, 21(4):1457–1469, 2005.

[62] M Ciavarella. A very simple estimate of adhesion of hard solids with rough surfaces based on a bearing area model. *Meccanica*, 53(1-2):241–250, 2018.

[63] JA Greenwood. Reflections on and extensions of the fuller and tabor theory of rough surface adhesion. *Tribology Letters*, 65(4):159, 2017.

[64] G Carbone, E Pierro, and G Recchia. Loading-unloading hysteresis loop of randomly rough adhesive contacts. *Physical Review E*, 92(6):062404, 2015.

[65] KL Johnson. *Contact Mechanics*. Cambridge university press, 1987.

[66] F Yang. Asymptotic solution to axisymmetric indentation of a compressible elastic thin film. *Thin Solid Films*, 515(4):2274–2283, 2006.

[67] II Argatov, GS Mishuris, and VL Popov. Asymptotic modelling of the jkr adhesion contact for a thin elastic layer. *The Quarterly Journal of Mechanics and Applied Mathematics*, 69(2):161–179, 2016.

[68] F Yang. Adhesive contact between a rigid axisymmetric indenter and an incompressible elastic thin film. *Journal of Physics D: Applied Physics*, 35(20):2614, 2002.

[69] A Papangelo. Adhesion between a power-law indenter and a thin layer coated on a rigid substrate. *Facta Universitatis*, 16(1):19–28, 2018.

[70] M Hannah. Contact stress and deformation in a thin elastic layer. *The Quarterly Journal of Mechanics and Applied Mathematics*, 4(1):94–105, 1951.

[71] V Shenoy and A Sharma. Pattern formation in a thin solid film with interactions. *Physical Review Letters*, 86(1):119, 2001.

[72] J Sarkar, V Shenoy, and A Sharma. Patterns, forces, and metastable pathways in debonding of elastic films. *Physical Review Letters*, 93(1):018302, 2004.

[73] M Gonuguntla, A Sharma, R Mukherjee, and SA Subramanian. Control of self-organized contact instability and patterning in soft elastic films. *Langmuir*, 22(16):7066–7071, 2006.

[74] W Mönch and S Herminghaus. Elastic instability of rubber films between solid bodies. *EPL (Europhysics Letters)*, 53(4):525, 2001.

[75] BNJ Persson and M Scaraggi. Theory of adhesion: role of surface roughness. *The Journal of Chemical Physics*, 141(12):124701, 2014.

[76] R Mukherjee, R Pangule, A Sharma, and G Tomar. Contact instability of elastic bilayers: miniaturization of instability patterns. *Advanced Functional Materials*, 17(14):2356–2364, 2007.

[77] M Ciavarella, J Joe, A Papangelo, and JR Barber. The role of adhesion in contact mechanics. *Journal of the Royal Society Interface*, 16(151):20180738, 2019.

[78] A Ghosh, D Bandyopadhyay, and A Sharma. Influence of the mutable kinetic parameters on the adhesion and debonding of thin viscoelastic films. *Journal of Colloid and Interface Science*, 477:109–122, 2016.

[79] A Ghosh, D Bandyopadhyay, J Sarkar, and A Sharma. Hierarchical micro-and nanofabrication by pattern-directed contact instabilities of thin viscoelastic films. *Physical Review Fluids*, 2(12):124004, 2017.

[80] J Sarkar and A Sharma. A unified theory of instabilities in viscoelastic thin films: from wetting to confined films, from viscous to elastic films, and from short to long waves. *Langmuir*, 26(11):8464–8473, 2010.

[81] A Ghosh, D Bandyopadhyay, and A Sharma. Micro-patterning of coatings on a fiber surface exploiting the contact instabilities of thin viscoelastic films. *Physics of Fluids*, 30(11):114101, 2018.

[82] N Bhandaru, A Sharma, and R Mukherjee. Programmable nanopatterns by controlled debonding of soft elastic films. *ACS Applied Materials & Interfaces*, 9(23):19409–19416, 2017.

[83] A Sharma, M Gonuguntla, R Mukherjee, SA Subramanian, and RC Pangule. Self-organized meso-patterning of soft solids by controlled adhesion: elastic contact lithography. *Journal of Nanoscience and Nanotechnology*, 7(6):1744–1752, 2007.

[84] R Mukherjee, RC Pangule, A Sharma, and I Banerjee. Contact instability of thin elastic films on patterned substrates. *The Journal of Chemical Physics*, 127(6):064703, 2007.

[85] M Gonuguntla, A Sharma, and SA Subramanian. Elastic contact induced self-organized patterning of hydrogel films. *Macromolecules*, 39(9):3365–3368, 2006.

[86] J Sarkar, A Sharma, and V Shenoy. Adhesion and debonding of soft elastic films on rough and patterned surfaces. *The Journal of Adhesion*, 81(3-4):271–295, 2005.

[87] B Davis-Purcell, P Soulard, T Salez, E Raphaël, and K Dalnoki-Veress. Adhesion-induced fingering instability in thin elastic films under strain. *The European Physical Journal E*, 41(3):1–7, 2018.

[88] S Sahoo, N Bhandaru, and R Mukherjee. Reversible morphological switching and deformation hysteresis in electric field mediated instability of thin elastic films. *Soft Matter*, 15(18):3828–3834, 2019.

[89] N Arun, A Sharma, VB Shenoy, and KS Narayan. Electric-field-controlled surface instabilities in soft elastic films. *Advanced Materials*, 18(5):660–663, 2006.

[90] J Sarkar, A Sharma, and VB Shenoy. Electric-field induced instabilities and morphological phase transitions in soft elastic films. *Physical Review E*, 77(3):031604, 2008.

[91] BNJ Persson. Theory of rubber friction and contact mechanics. *The Journal of Chemical Physics*, 115(8):3840–3861, 2001.

[92] JR Barber. *Contact Mechanics*, volume 250. Springer, 2018.